

# Proposal for $K_L \rightarrow \pi^0 \nu \bar{\nu}$ Experiment at J-Parc

April 28, 2006  
Revised: May 2, 2006

Joseph Comfort and Jeremy Figgins  
*Arizona State University, Physics Department*  
*Tempe, Arizona 85287 USA*

Mircea Bogdan, Jiasen Ma, Fukun Tang, Harold Sanders, and  
Yau W. Wah  
*Enrico Fermi Institute, The University of Chicago*  
*5640 South Ellis Avenue, Chicago, Illinois 60637, USA*

Alexandr S. Kurilin, Evgeni S. Kuzmin, Sergey V. Podolsky, and  
Anton A. Shuteev  
*Joint Institute for Nuclear Research (JINR)*  
*Dzhelepov Laboratory of Nuclear Problems*  
*Joliot-Curie St., 6, Dubna Moscow Region 141980, Russia*

Mikhail Yu. Doroshenko, Takao Inagaki, Nobuhiro Ishihara,  
Takeshi K. Komatsubara, Gei-Youb Lim, Hideki Okuno,  
Takahiro Sato, Michiko Sekimoto, Hiroaki Watanabe, and  
Yoshio Yoshimura  
*High Energy Accelerator Research Organization (KEK)*  
*Oho 1-1, Tsukuba-shi, Ibaraki 305-0801, Japan*

Hideki Morii, Yasuhiro Nakajima, Hajime Nanjo, Tadashi Nomura,  
Noboru Sasao, and Toshi Sumida  
*Kyoto University, Department of Physics*  
*Kitashirakawa-Oiwake, Sakyo, Kyoto 606-8502, Japan*

Toru Matsumura and Takao Shinkawa  
*National Defense Academy, Department of Applied Physics*  
*1-10-20 Hashirimizu, Yokosuka 239-8686, Japan*

Kai-Feng Chen, Yee Bob Hsiung, Yu-Chen Tung, and Meng-Lin Wu  
*National Taiwan University, Department of Physics*  
*1, Roosevelt Rd., Sec.4, Taipei, Taiwan 10617 ROC*

Eito Iwai, Atsushi Kakehashi, Ken Sakashita, Mitsuhiro Yamaga, and  
Taku Yamanaka  
*Osaka University, Department of Physics*  
*1-1 Machikaneyama, Toyonaka, Osaka 560-0043, Japan*

Jung Keun Ahn, Hyo Sang Lee, and Kwang Yoon Baik  
*Pusan National University, Department of Physics*  
*Pusan 609-735, Korea*

Shiro Suzuki, Shigeharu Kobayashi, Risa Ogata, Tetsushi Shimogawa,  
and Masayuki Yoshimi  
*Saga University, Department of Physics*  
*1 Honjo-machi, Saga 840-8502, Japan*

Macharashvili Gogi and Tsamalaidze Zviadi  
*Tbilisi State University, Department of Physics*  
*I. Chavchavadze Avenue, 3, 0128, Tbilisi, Georgia*

Toshio Numao  
*TRIUMF*  
*4004 Wesbrook Mall, Vancouver, British Columbia, Canada, V6T 2A3*

Takahiro Iwata<sup>1</sup>, Yasuhisa Tajima<sup>2</sup>, and Hiroshi Yoshida<sup>2</sup>  
*Yamagata University,*  
*<sup>1</sup>Department of Physics, and <sup>2</sup>Networking and Computing Service*  
*Center*  
*1-4-12 Kojirakawa-machi, Yamagata 990-8560, Japan*

Spokesperson: Taku Yamanaka  
Email: taku@hep.sci.osaka-u.ac.jp, Phone: +81-6-6850-5356

# Contents

<b>1</b>	<b>Executive Summary</b>	<b>5</b>
<b>2</b>	<b>Physics Motivation</b>	<b>6</b>
2.1	Standard Model . . . . .	6
2.2	Beyond the Standard Model . . . . .	9
2.3	$K_L^0 \rightarrow \pi^0 \nu \bar{\nu}$ and Flavor Physics in the next decade . . . . .	10
2.4	Other physics decay modes . . . . .	16
2.4.1	$K_L^0 \rightarrow \pi^0 \pi^0 \nu \bar{\nu}$ . . . . .	16
2.4.2	Light sgoldstinos in $K_L^0 \rightarrow \pi^0 \pi^0 X^0$ . . . . .	17
2.4.3	$K_L^0 \rightarrow \pi^0 \gamma \gamma$ . . . . .	17
<b>3</b>	<b>Strategy</b>	<b>19</b>
3.1	Basic strategy of the experiment . . . . .	19
3.2	E391a . . . . .	20
3.3	Step 1 . . . . .	20
3.4	Step 2 . . . . .	21
<b>4</b>	<b>Step 1</b>	<b>23</b>
4.1	Goal of Step 1 . . . . .	23
4.2	Beamline . . . . .	23
4.3	Detector . . . . .	27
4.3.1	Calorimeter . . . . .	28
4.3.2	Barrel Photon Veto . . . . .	34
4.3.3	Charged Veto . . . . .	38
4.3.4	Collar Counters . . . . .	42
4.3.5	Beam Hole Veto . . . . .	43
4.3.6	Vacuum . . . . .	46
4.4	Frontend electronics, Trigger, and DAQ . . . . .	47
4.4.1	Electronics . . . . .	47
4.4.2	Trigger and DAQ . . . . .	49
4.5	Rates . . . . .	50
4.6	Sensitivity . . . . .	51
4.6.1	Detector acceptance . . . . .	51
4.6.2	Acceptance Loss . . . . .	53
4.6.3	Single event sensitivity . . . . .	55
4.7	Backgrounds . . . . .	55
4.7.1	$K_L \rightarrow \pi^0 \pi^0$ background . . . . .	56
4.7.2	$K_L \rightarrow \gamma \gamma$ background . . . . .	60

4.7.3	$K_L \rightarrow \pi^0\pi^0\pi^0$ background . . . . .	60
4.7.4	$K_L \rightarrow \pi^+\pi^-\pi^0$ Background . . . . .	62
4.7.5	$K_L \rightarrow \pi^-e^+\nu$ Background . . . . .	63
4.7.6	Neutron Background . . . . .	65
4.7.7	Accidental halo neutron background . . . . .	67
<b>5</b>	<b>Step 2</b>	<b>69</b>
5.1	New beamline . . . . .	69
5.2	Detector . . . . .	71
5.3	Sensitivity and Background . . . . .	72
5.4	Detector R&D . . . . .	74
5.4.1	Endcap Calorimeter . . . . .	74
5.4.2	Charged Veto . . . . .	75
5.4.3	Pipeline readout . . . . .	78
<b>6</b>	<b>Schedule and Cost</b>	<b>79</b>
6.1	Schedule . . . . .	79
6.2	Cost . . . . .	79
<b>7</b>	<b>Conclusion</b>	<b>81</b>
<b>A</b>	<b>Appendices</b>	<b>82</b>
A.1	Beam Simulation . . . . .	82
A.2	Photon Veto Inefficiency . . . . .	87
A.3	Charged Particle Veto Inefficiency . . . . .	90
A.4	Expected Performance of Beam Hole Photon Veto . . . . .	93

# 1 Executive Summary

The very rare decay  $K_L^0 \rightarrow \pi^0 \nu \bar{\nu}$  is a sensitive probe for direct CP violation in the quark sector. The decay is a Flavor Changing Neutral Current process that is induced through electroweak loop diagrams. The branching ratio for  $K_L^0 \rightarrow \pi^0 \nu \bar{\nu}$  is predicted to be  $(2.8 \pm 0.4) \times 10^{-11}$  in the Standard Model, and the theoretical uncertainty is estimated to be only a few percent. The decay is also sensitive to new physics scenarios beyond the Standard Model such as Supersymmetric theories. A comparison of the CP-violation parameters from  $K_L^0 \rightarrow \pi^0 \nu \bar{\nu}$  with the values obtained from experiments at the B factories is therefore a precise tool for discovering and understanding the flavor structure in new physics.

We propose to measure the branching ratio of the  $K_L \rightarrow \pi^0 \nu \bar{\nu}$  decay with an uncertainty less than 10%. We will take a *step-by-step* approach to achieve our goal.

We have already run a pilot experiment, E391a, at the KEK 12-GeV Proton Synchrotron. We propose to reuse the beamline and detector, and apply necessary modifications based on our experience with E391a. In particular, we plan to replace the CsI crystals in the Calorimeter with the smaller-size crystals used in the Fermilab KTeV experiment. We will start running at Time 0 of the J-PARC slow extraction beam, by using the common T1 target on the A-line and a neutral beam line with a  $16^\circ$  extraction angle; this stage will be the **Step 1** of our experiment. Our goal of **Step 1** is to make the first observation of the decay. We expect to observe 3.5 Standard Model events (with a 50% acceptance loss due to tight extra-photon rejection) with  $1.8 \times 10^{21}$  protons on target in total. The expected S/N ratio is 1.4. The beamline and detector in **Step 1** can be realized with reasonable costs.

In the **Step 2** stage, we plan to upgrade the beam line and the detector, and accumulate more than 100 Standard Model events with an S/N ratio of 4.8.

This proposal is focused on the **Step 1** experiment, but will also show our plan for **Step 2**.

## 2 Physics Motivation

CP violation is currently recognized as one of the forefront issues in elementary particle physics. Together with obtaining a better understanding of quark mixing as well as neutrino mixing phenomena, it is one of the central goals of particle physics and has been pursued vigorously in many experiments. The very rare decay  $K_L^0 \rightarrow \pi^0 \nu \bar{\nu}$  [2] provides one of the best probes for understanding the origin of CP violation in the quark sector [3, 4]. The decay is a Flavor Changing Neutral Current (FCNC) process from strange quark to down quark, and its observation will provide new positive evidence for direct CP violation. It has been established that studies of FCNC processes are extremely useful for understanding the underlying physics phenomena.

The decay  $K_L^0 \rightarrow \pi^0 \nu \bar{\nu}$  is a unique and clean process. The decay has been considered as an ideal “golden mode” in quark flavor physics for a critical test of the Standard Model (SM), as well as a search for new physics beyond the SM [5, 6]. The ultimate goal of this proposal is to achieve a sensitivity of better than  $3 \times 10^{-13}$  for the branching ratio, corresponding to an observation of more than 100 events for the Standard Model prediction. This result would determine the height of the CKM unitarity triangle, represented by the imaginary part  $\eta$  of the CKM matrix, to better than 5% accuracy.

### 2.1 Standard Model

Understanding the phenomenology of quark mixing and CP violation requires examining the CKM ansatz of the Standard Model through precise determination of its basic parameters, several of which are still poorly known. To assure a clear interpretation of the experimental results, the ideal observable must not only be sensitive to fundamental parameters, but it must also be calculable with little theoretical ambiguity.

The rare decay  $K_L^0 \rightarrow \pi^0 \nu \bar{\nu}$  provides such an opportunity and is unique among potential SM observables. It is dominated by direct CP violation and is entirely governed by short-distance physics involving the top quark. Long-distance contributions have been shown to be negligible. Theoretical uncertainties are extremely small in SM calculations.

The  $K_L^0 \rightarrow \pi^0 \nu \bar{\nu}$  decay is a FCNC process that is induced through loop effects. A direct term, which proceeds through a  $\Delta S = 1$  transition as expressed by the electroweak penguin and box diagrams shown in Fig. 1, dominates an “indirect” mixing term that proceeds through a  $\Delta S = 2$  transition where  $K_L^0$  changes into  $K_S^0$  via  $K^0 - \bar{K}^0$  mixing [7]. The  $K_L^0 \rightarrow \pi^0 \nu \bar{\nu}$

decay therefore offers information of the  $\Delta S = 1$  process. The hadronic matrix element can be factorized as the well-known branching ratio of the  $K \rightarrow \pi e \nu$  decay [8]. The higher-order QCD corrections that couple to the virtual top quark are calculable but small due to the large mass of the top quark [9]. A long-distance interaction contributes little to the  $K_L^0 \rightarrow \pi^0 \nu \bar{\nu}$  decay [7, 10, 11], because neutrinos are weakly interacting particles. Consequently, an uncertainty in the theoretical calculation is estimated to be only a few percent, and the  $K_L^0 \rightarrow \pi^0 \nu \bar{\nu}$  decay will offer clean information on an important basic parameter of current elementary particle physics.

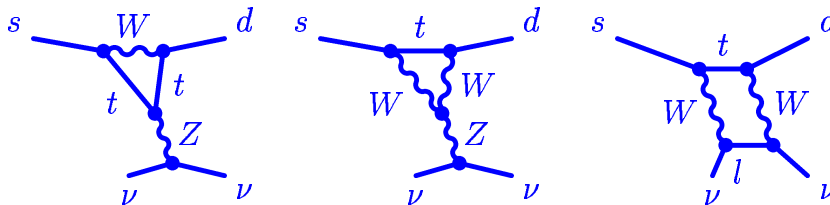


Figure 1: SM diagrams for the  $K_L^0 \rightarrow \pi^0 \nu \bar{\nu}$  decay.

In the Standard Model, the decay amplitude of  $K_L^0 \rightarrow \pi^0 \nu \bar{\nu}$  is proportional to the imaginary part of a product of CKM matrix elements,  $Im(V_{ts}^* V_{td})$ , which corresponds to the height of the unitarity triangle as shown in Fig. 2. The unitarity of the CKM matrix has been considered as one of the most critical checks for new physics beyond the Standard Model. The pure and clean information obtained by the  $K_L^0 \rightarrow \pi^0 \nu \bar{\nu}$  decay is crucial for checks of the SM as well as those by  $B$  decays. By using current estimates for SM parameters, the branching ratio for  $K_L^0 \rightarrow \pi^0 \nu \bar{\nu}$  is predicted to be

$$\mathcal{B}(K_L^0 \rightarrow \pi^0 \nu \bar{\nu}) = (2.20 \pm 0.07) \times 10^{-10} \left( \frac{\lambda}{0.2248} \right)^8 \left[ \frac{Im(V_{ts}^* V_{td})}{\lambda^5} X(x_t) \right]^2, \quad (1)$$

and is expected to lie in the range  $(2.8 \pm 0.4) \times 10^{-11}$  [12]. Here  $\lambda \equiv |V_{us}|$ ,  $X(x_t) = 1.464 \pm 0.041$  is the value of Inami-Lim loop function [13] (including the QCD correction), and the parameter  $x_t$  is the square of the ratio of the top quark and W masses. Because  $\eta$  in  $Im(V_{ts}^* V_{td}) = -A^2 \lambda^5 \eta$  measures directly the height of kaon unitarity triangle, the decay amplitude  $K_L^0 \rightarrow \pi^0 \nu \bar{\nu}$  violates CP directly and offers the best opportunity for measuring the Jarlskog invariant:

$$J_{\text{CP}} \equiv -Im(V_{ts}^* V_{td} V_{us}^* V_{ud}) = -\lambda \left( 1 - \frac{\lambda^2}{2} \right) Im(V_{ts}^* V_{td}), \quad (2)$$

which is proportional to twice the area of the unitarity triangle [14].

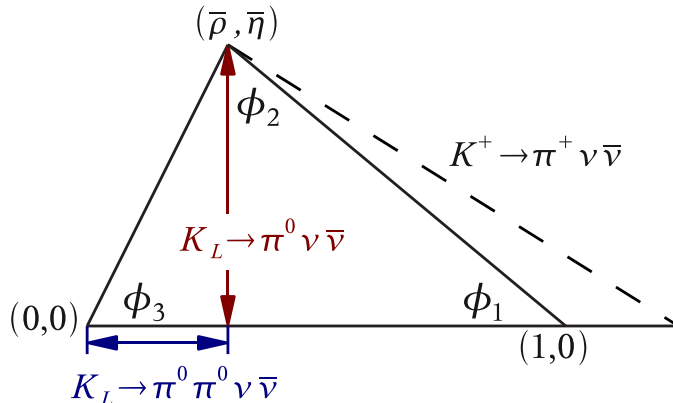


Figure 2: Kaon unitarity triangle.

Although the best direct experimental information on the  $K_L^0 \rightarrow \pi^0 \nu \bar{\nu}$  mode will be from the full E391a data set, the first preliminary result for the branching ratio is  $\mathcal{B}(K_L^0 \rightarrow \pi^0 \nu \bar{\nu}) < 2.1 \times 10^{-7}$  as a 90% confidence-level (C.L.) upper limit [15]. A more stringent constraint can be derived by using the information on the charged mode [16] and isospin symmetry, and is called ‘‘Grossman-Nir (GN) bound’’ [17]:

$$\mathcal{B}(K_L^0 \rightarrow \pi^0 \nu \bar{\nu}) \leq 4.4 \times \mathcal{B}(K^+ \rightarrow \pi^+ \nu \bar{\nu}) \quad (3)$$

which gives

$$\mathcal{B}(K_L^0 \rightarrow \pi^0 \nu \bar{\nu}) < 1.4 \times 10^{-9}. \quad (4)$$

As discussed in Ref. [17], this bound is valid in virtually any extension of the Standard Model. By comparing this model-independent bound and the SM prediction, it is clear that there is still considerable room for new physics in  $K_L^0 \rightarrow \pi^0 \nu \bar{\nu}$ . But even if the experimental measurement of  $\mathcal{B}(K_L^0 \rightarrow \pi^0 \nu \bar{\nu})$  was found to be in agreement with the SM expectation with a small relative error, this information would translate into a unique and precious insight about the CP and flavor structure of any extension of the SM. These features make the experimental search for  $K_L^0 \rightarrow \pi^0 \nu \bar{\nu}$ , at the SM level and below, a must-do experiment.

The super-weak model, which causes CP violation only in the mixing ( $\Delta S = 2$  transition), is almost ruled out by the recent  $\epsilon'/\epsilon$  experiments at Fermilab [18] and CERN [19]. However, the other primary explanation, the CKM matrix (*i.e.* the Standard Model), accommodates the experimental

results but has basic problems, such as the strong CP problem and the lack of strength for baryogenesis. Problems of CP violation are not solved yet. One of the best ways to understand profoundly the physics of CP violation is to measure precisely its strength in all FCNC processes,  $\Delta S = 1, 2$  and  $\Delta B = 1, 2$ . For  $\Delta B = 1, 2$ ,  $B$ -factory experiments such as Belle, Babar and LHCb can provide answers at the level of a few percent. For  $\Delta S = 2$ , lattice calculations may soon solve the problem of the large theoretical ambiguity for  $\epsilon$ . However, the precise value of  $\Delta S = 1$  can only be obtained from a measurement of  $K_L^0 \rightarrow \pi^0 \nu \bar{\nu}$  decay.

A recent paper by Buras, Gorbahn, Haisch, and Nierste [12], who completed the next-to-next-to-leading order (NNLO) QCD calculation of the charmed penguin contribution to  $K^+ \rightarrow \pi^+ \nu \bar{\nu}$ , has improved the theoretical accuracy by a factor of 4 and reduced the error of the charmed penguin uncertainty in the charged mode from  $\pm 9.8\%$  down to  $\pm 2.4\%$ . Their results are translated into the following theoretical uncertainties in the  $K \rightarrow \pi \nu \bar{\nu}$  system on the quantities of interest as:

$$\frac{\sigma(|V_{td}|)}{|V_{td}|} = \pm 1.0\%, \quad \sigma(\sin 2\phi_1) = \pm 0.006, \quad \text{and} \quad \sigma(\phi_3) = \pm 1.2^\circ, \quad (5)$$

implying a better constraint on the CKM parameters in the future.

## 2.2 Beyond the Standard Model

Extensions of the Standard Model in principle can modify the physics discussed above in many ways. Extended models usually introduce a variety of new degrees of freedom and many unknown parameters, and it is therefore difficult to obtain definite predictions. However, one can make some general remarks relevant for  $K_L^0 \rightarrow \pi^0 \nu \bar{\nu}$  and the comparison with information from the  $B$  sector.

Various models beyond the SM predict sizable effects on the  $K_L^0 \rightarrow \pi^0 \nu \bar{\nu}$  decay. For example, in the Minimal Supersymmetric extensions of the SM (MSSM) with new sources of flavor mixing, there is considerable room for possible enhancements in the  $K_L^0 \rightarrow \pi^0 \nu \bar{\nu}$  branching ratio even after taking into account all of the available constraints from other CP-violating observables and rare decays [20, 21].

A clean SM test is provided by comparing  $\eta$  from  $K_L^0 \rightarrow \pi^0 \nu \bar{\nu}$  with the measurements of  $|V_{ub}|/|V_{cb}|$  in  $b \rightarrow u$  versus  $b \rightarrow c$  decays, and  $x_d/x_s$  in  $B_d-\bar{B}_d$  vs.  $B_s-\bar{B}_s$  mixing. Similarly, if the branching ratio  $\mathcal{B}(K^+ \rightarrow \pi^+ \nu \bar{\nu})$  is measured precisely, a very clean test is to compare the value of  $\sin 2\phi_1$

obtained from the two kaon rare decays with that determined from the CP-asymmetry in  $B \rightarrow J/\psi K_S$ . Other incisive tests involve comparisons of the Jarlskog invariant obtained from  $\mathcal{B}(K_L^0 \rightarrow \pi^0 \nu \bar{\nu})$  with indirect determinations of the same quantity from the  $B$  system. Any discrepancy would clearly indicate new physics.

In some new physics scenarios, such as multi-Higgs doublets models [22] or the specific MSSM in which the CKM matrix remains the sole source of CP violation (called the ‘‘Minimal Flavor Violation’’ hypothesis) [23, 24], the extraction of  $\sin 2\phi_1$  and  $\sin 2\phi_2$  from CP asymmetries in  $B$  decays would be unaffected. Such effects might show up in a comparison with  $K_L^0 \rightarrow \pi^0 \nu \bar{\nu}$ , where the charged Higgs contributions modify the top quark loop contribution [25]. In other new physics scenarios, such as Supersymmetric flavor models [26] or extra dimensions [27], the effects in  $K \rightarrow \pi \nu \bar{\nu}$  tend to be small, while there can be large effects in the  $B$  (and also in  $D$ ) systems. In these models, the rare  $K$  decays are the only clean way to measure the true CKM parameters. Examples for new physics scenarios that show drastic deviations from the SM are provided by some of the extended Higgs models [28], topcolor-assisted technicolor models [29], left-right symmetric models [30], models with extra quarks in vector-like representations [31], lepto-quark exchange [17], and four-generation models [32]. Figures 3 [33, 3] and 4 [24] show examples of possible new physics scenarios [5] that can drastically change the SM predictions.

Even in the  $K$ -decay observables, the additional beyond-the-SM effects change the SM predictions in different directions. For example, the  $\epsilon$  parameter in  $K^0$ - $\bar{K}^0$  mixing and in  $K_L^0 \rightarrow \pi^0 \nu \bar{\nu}$  decay change values in opposite directions [34, 35]. Thus, measuring the  $K_L^0 \rightarrow \pi^0 \nu \bar{\nu}$  decay branching ratio to an accuracy of a few percent will provide a critical check on effects beyond the Standard Model.

### 2.3 $K_L^0 \rightarrow \pi^0 \nu \bar{\nu}$ and Flavor Physics in the next decade

Observation of  $K_L^0 \rightarrow \pi^0 \nu \bar{\nu}$  enables us to perform the stringent test of the quark flavor sector in the Standard Model. Figure 5 shows how we can discover or discriminate several new physics scenarios by improving the sensitivity. An experiment with 100 SM events tells us whether the  $s \rightarrow d$  transition is consistent with the SM or not. If signatures of new physics are observed in the LHC experiments beginning in 2007, we can study whether the flavor structure is in the Minimal Flavor Violation hypothesis or more generic ones.

An experiment with a sensitivity of  $3 \times 10^{-13}$  determines  $\eta$  and  $\sin 2\phi_1$

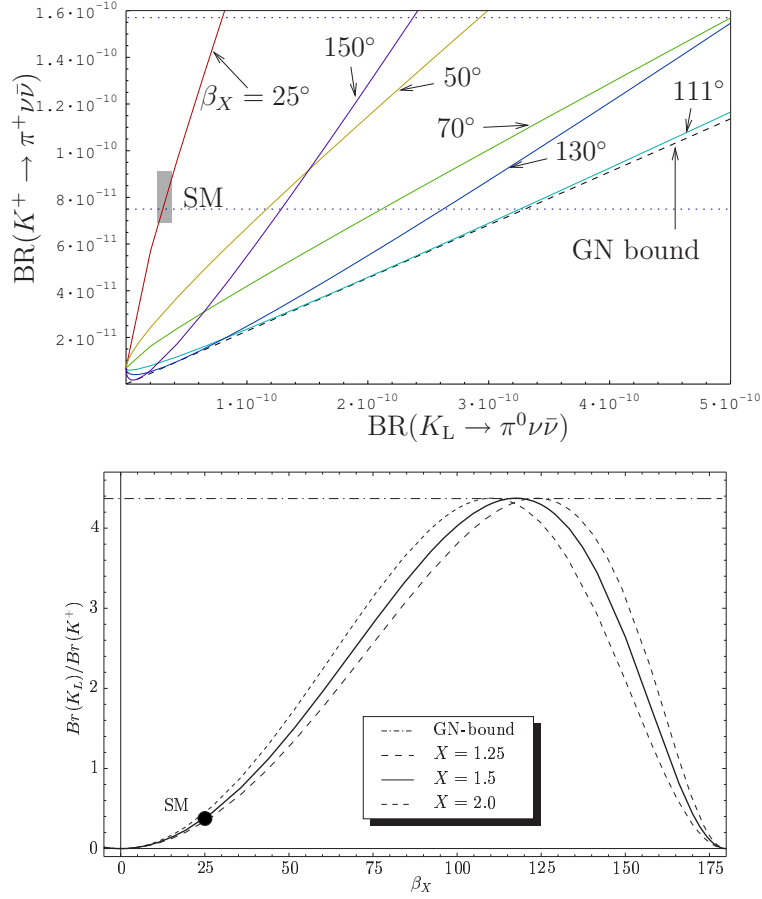


Figure 3: Top: correlation of  $\mathcal{B}(K_L^0 \rightarrow \pi^0 \nu \bar{\nu})$  and  $\mathcal{B}(K^+ \rightarrow \pi^+ \nu \bar{\nu})$  for various values of  $\beta_X$ , which is the difference of  $\phi_1$  in the SM from the new CP-violating phase  $\theta_X$  beyond the SM [33]. Bottom: ratio of  $\mathcal{B}(K_L^0 \rightarrow \pi^0 \nu \bar{\nu})$  to  $\mathcal{B}(K^+ \rightarrow \pi^+ \nu \bar{\nu})$  as a function of  $\beta_X$  for  $|X| = 1.25, 1.5, 2.0$ , where  $X \equiv |X|e^{i\theta_X}$  is the short-distance function, instead of the Inami-Lim function, beyond the SM [3].

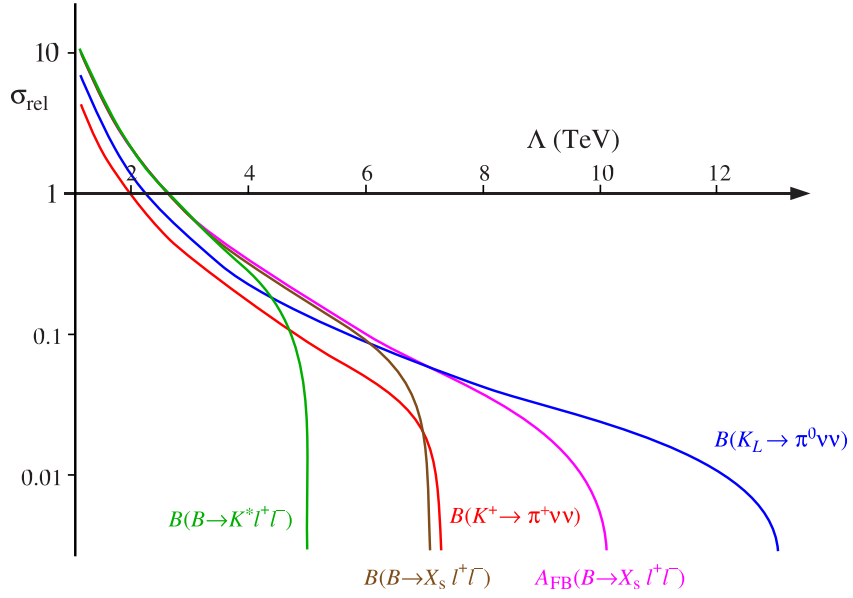
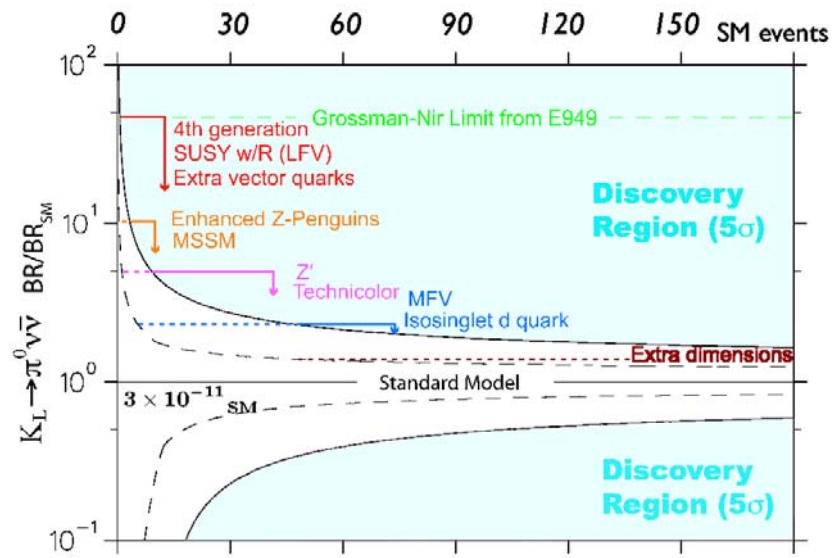


Figure 4: Comparison of the effectiveness of different observables in rare  $K$  and  $B$  decays in setting future bounds on the energy scale of new physics operators [24]. The vertical axis indicates the relative precision of a hypothetical measurement of the observable, with the central value equal to the SM expectation. The curves are obtained by assuming an uncertainty of 1% precision on the corresponding overall CKM factor.



based on Bryman-Buras-Isidori-Littenberg, hep-ph/0505171

Figure 5: A  $5\sigma$  discovery region (shaded area) and 95% CL upper and lower exclusion limits versus the number of  $K_L^0 \rightarrow \pi^0 \nu \bar{\nu}$  events, assuming the SM, from the study by Bryman, Buras, Isidori and Littenberg [5]. The maximal enhancement of the branching ratio (BR) expected in various non-SM scenarios are also included.

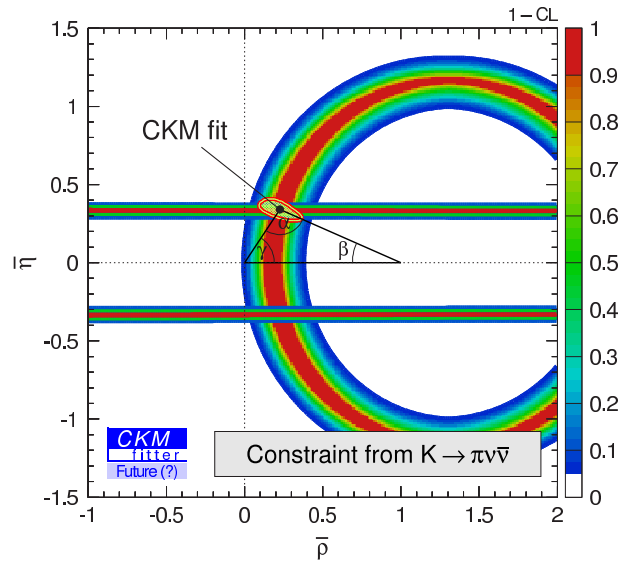


Figure 6: Constraints in the  $\rho - \eta$  plane from future measurements of  $\mathcal{B}(K_L^0 \rightarrow \pi^0 \nu \bar{\nu})$  and  $\mathcal{B}(K^+ \rightarrow \pi^+ \nu \bar{\nu})$  with an accuracy of  $\pm 10\%$ . The constraints from the CKM global fit obtained by the CKMfitter Group [36] are overlaid.

in the SM with the accuracies of 6.3% and 7.0%, respectively [3]. These precisions are comparable to those obtained by the CKM global fits in 2005 (6.8% and 4.7%, respectively<sup>1</sup>) [36, 37], as shown in Fig. 6. In order to identify the signature of new physics, deviations of  $\sin 2\phi_1$  measured in several  $B$  and  $K$  decay modes ( $\equiv S_m$ ) from that in  $B \rightarrow J/\psi K_S^0$  ( $\equiv S_{J/\psi K_S^0}$ ),  $\Delta S_m \equiv S_m - S_{J/\psi K_S^0}$ , are useful because  $S_{J/\psi K_S^0}$  will be precisely measured in the near future. The precision of  $\Delta S_{\pi^0 \nu \bar{\nu}}$  with the sensitivity of  $3 \times 10^{-13}$  is  $\pm 0.05$  [3],<sup>2</sup> while the precision of  $\Delta S_{\phi K_S^0}$  from the  $B \rightarrow \phi K_S^0$  decay, which is the most promising mode for new physics in the future Super- $B$  factories, is expected to be  $\pm 0.08$  with  $5 \text{ ab}^{-1}$  and  $\pm 0.03$  with  $50 \text{ ab}^{-1}$  integrated luminosity, respectively [38]. We would point out that a  $\sigma(\Delta S_{\pi^0 \nu \bar{\nu}})$  of  $\pm 0.05$  is comparable to  $\sigma(\Delta S_{\phi K_S^0})$  from Super- $B$  running for a few years ( $15 \text{ ab}^{-1}$ ), which indicates the competitiveness of the J-PARC  $K_L^0$  program to the other flavor-physics experiments in the 2010's (Fig. 7).

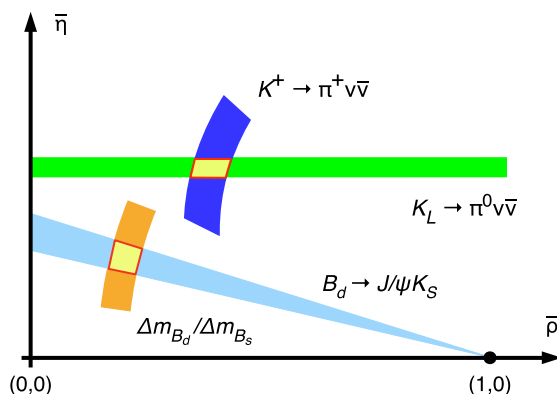


Figure 7: Schematic determination of  $(\rho, \eta)$  from the  $B$  system ( $B_d \rightarrow J/\psi K_S$  and  $\Delta m_{B_d}/\Delta m_{B_s}$ ) and from  $K \rightarrow \pi \nu \bar{\nu}$  [39].

<sup>1</sup>The  $K_L^0 \rightarrow \pi^0 \nu \bar{\nu}$  measurement determines  $\eta$  directly, while  $B$ -factory experiments measure  $\sin 2\phi_1$  from the  $B \rightarrow J/\psi K_S^0$  and related decays. The precision of  $\sin 2\phi_1$  in  $B$  experiments is always better than the precision of  $\eta$ .

<sup>2</sup>Here we assume the number of  $K_L^0 \rightarrow \pi^0 \nu \bar{\nu}$  events to be 100 as in the SM. The precision gets better if the branching ratio is larger than the prediction in the SM.

## 2.4 Other physics decay modes

Table 1 is a list of kaon decays anticipated as byproducts in the  $K_L^0 \rightarrow \pi^0 \nu \bar{\nu}$  experiment. The physics of the first three topics in the table are explained in this subsection.

Table 1: Other physics decay modes in the J-PARC  $K_L^0$  experiment. "NP" means the prediction in New Physics.

decay mode	physics	(past result) prediction	Ref.
$K_L^0 \rightarrow \pi^0 \pi^0 \nu \bar{\nu}$	FCNC, $\rho$	$1.4 \times 10^{-13}$	[40]
$K_L^0 \rightarrow \pi^0 \pi^0 X_{\text{invisible}}^0$	light sgoldstino	$10^{-3}$ in NP	[41, 42]
$K_L^0 \rightarrow \pi^0 \pi^0 X_{\mu^+ \mu^-}^0$	HyperCP events	$10^{-8}$ in NP	[44, 45, 46, 47]
$K_L^0 \rightarrow \pi^0 \pi^0 X_{\gamma\gamma}^0$	HyperCP events	$10^{-4}$ in NP	[44, 45, 46, 47]
$K_L^0 \rightarrow \pi^0 \gamma \gamma$	ChPT	$M_{\gamma\gamma}$ spectrum ( $1.5 \times 10^{-6}$ )	[49, 50]
$K_L^0 \rightarrow \pi^0 \pi^0 \gamma$	ChPT	$7 \times 10^{-11}$ $\sim 1 \times 10^{-8}$ ( $< 5.6 \times 10^{-6}$ )	[51]
$K_L^0 \rightarrow \gamma \nu \bar{\nu}$	new physics	$0.7 \times 10^{-11}$	[52, 53, 54]
$K_L^0 \rightarrow \pi^0 \gamma \nu \bar{\nu}$	new physics	$4.4 \times 10^{-15}$	
$K_L^0 \rightarrow \gamma \gamma \gamma$	Bose/gauge sym.	$3 \times 10^{-19}$ ( $< 2.4 \times 10^{-7}$ )	[55, 56]

### 2.4.1 $K_L^0 \rightarrow \pi^0 \pi^0 \nu \bar{\nu}$

The CP conserving decay  $K_L^0 \rightarrow \pi^0 \pi^0 \nu \bar{\nu}$  is a Flavor Changing Neutral Current process and involves an  $s \rightarrow d \nu \bar{\nu}$  transition. Similar to the  $K_L^0 \rightarrow \pi^0 \nu \bar{\nu}$  decay, this mode is not sensitive to long-distance contributions. The branching ratio, which is proportional to the square of the CKM matrix parameter  $\rho$  (Fig. 2), is predicted to be  $(1.4 \pm 0.4) \times 10^{-13}$  with little theoretical uncertainty [40]. We have started working on this decay mode with the E391a data set, and expect to improve the upper limit further at J-PARC.

### 2.4.2 Light sgoldstinos in $K_L^0 \rightarrow \pi^0 \pi^0 X^0$

The decay mode  $K_L^0 \rightarrow \pi^0 \pi^0 X^0$ , where  $X^0$  is a neutral weakly-interacting particle, allows one to search for a low-mass supersymmetric particle, called the “sgoldstino” [41, 42].<sup>3</sup> The masses of scalar and pseudoscalar sgoldstinos are model dependent and could be below a few  $\text{GeV}/c^2$  or a few  $\text{MeV}/c^2$ . Sgoldstinos are light in some gravity-mediated theories and gauge-mediated models. If the pseudoscalar sgoldstino  $P$  is light enough, ( $m_P < m_{K_L} - 2m_\pi$ ), then the decay of a neutral kaon to  $2\pi^0$  and the pseudoscalar sgoldstino, identified as  $K_L^0 \rightarrow \pi^0 \pi^0 X^0$ , is a very interesting probe of the physics.<sup>4</sup> Depending on the phases of the quark-sgoldstino coupling, the allowed branching ratio can be as high as  $10^{-3}$ .

The Fermilab HyperCP experiment recently reported [43] evidence for the decay  $\Sigma^+ \rightarrow p\mu^+\mu^-$  and suggested that the  $\mu^+\mu^-$  pair was due to the decay of a new neutral particle  $X^0$  at  $214 \text{ MeV}/c^2$ . A boson of such mass has never been searched for in the past. Theoretical studies [44, 45, 46, 47] pointed out that the branching ratios of  $K \rightarrow \pi\pi X^0$  following  $X^0 \rightarrow \mu^+\mu^-$  and  $X^0 \rightarrow \gamma\gamma$  could be as high as  $10^{-8}$  and  $10^{-4}$ , respectively. We have started a search with the E391a data set [48], and will continue at J-PARC.

### 2.4.3 $K_L^0 \rightarrow \pi^0 \gamma\gamma$

Two experiments, Fermilab E832 [49] and CERN NA48 [50], measured  $K_L^0 \rightarrow \pi^0 \gamma\gamma$  and showed strong evidence for the decay in the region of low  $\gamma\gamma$  invariant mass, as predicted by recent  $\mathcal{O}(p^6)$  calculations in chiral perturbation theory (ChPT) that include vector meson exchange contributions. However, their results differ by three standard deviations in both the branching ratio ( $\sim 1.5 \times 10^{-6}$ ) and the pole parameter  $a_V$ . This decay mode is important for the determination of the CP conserving amplitude of

---

<sup>3</sup>The spontaneous breaking of any global symmetry results in a massless Nambu-Goldstone mode with the same quantum numbers as the symmetry generator. In the case of supersymmetry, the symmetry generator is fermionic resulting in a Nambu-Goldstone fermion named “goldstino.” The exact nature of the goldstino depends on the specific model of supersymmetry. For example, in the case of supergravity theories, the superpartner of the graviton, the gravitino, absorbs the goldstino and thereby acquires a mass. As the goldstino is part of a superfield, it should have a superpartner, the complex scalar field  $z = (S + iP)/\sqrt{2}$  named “sgoldstino.” The real component  $S$  is the scalar sgoldstino, and the imaginary part  $P$  is the pseudoscalar sgoldstino.

<sup>4</sup>This possibility is not an unreasonable one as it arises in a variety of models. The coupling constants are constrained by the limits on the mass difference between  $K_L$  and  $K_S$  and requiring that the contribution to the CP violation parameter  $\epsilon$  in the kaon system is less than its measured value.

$K_L^0 \rightarrow \pi^0 e^+ e^-$ , which has a large direct CP-violating component. A high statistics study ( $\sim 10^4$  events) of  $K_L^0 \rightarrow \pi^0 \gamma \gamma$  is needed to resolve this issue. We expect to do such a measurement in the J-PARC experiment.

## 3 Strategy

### 3.1 Basic strategy of the experiment

The  $K_L \rightarrow \pi^0 \nu \bar{\nu}$  decay is a theoretically clean decay mode, but also a difficult decay mode to study experimentally. The incoming  $K_L$  cannot be observed before decaying, and only two photons are visible. The branching ratio expected from the Standard Model is very low,  $\simeq 3 \times 10^{-11}$ . One of the major backgrounds is  $K_L \rightarrow \pi^0 \pi^0$ , where two of the four photons are missed. Because the branching ratio of  $K_L \rightarrow \pi^0 \pi^0$  is  $8.83 \times 10^{-4}$ , the background has to be suppressed by 8 orders of magnitude or more.

In order to cope with these difficulties, we will use the following basic techniques.

- *Use a detector with a high acceptance.*  
This requirement is necessary for increasing the signal yield from a limited number of  $K_L$  decays. We will place an electromagnetic calorimeter downstream of the decay region to catch two photons from the  $K_L \rightarrow \pi^0 \nu \bar{\nu}$  decay. There will be a beam hole at the center of the calorimeter to let neutral particles go through.
- *Cover the decay region with hermetic photon veto counters with a low detection inefficiency.*  
This technique will suppress the  $K_L \rightarrow \pi^0 \pi^0$  decay backgrounds by detecting the extra two photons. Note that the background level is proportional to the product of the detection inefficiencies for those extra photons.
- *Place detectors inside high vacuum*  
The decay volume has to be evacuated, in order to suppress the number of  $\pi^0$ 's produced by neutrons interacting with residual gas. Also, placing the detector components inside instead of outside the vacuum tank eliminates dead material (*e.g.*, the vacuum tank) that could absorb photons before hitting the detector.
- *Use a  $K_L$  beam with a small size.*  
There are two reasons.
  - First, a small size allows us to minimize the beam hole in the calorimeter, and reduces the chance that photons from  $K_L \rightarrow \pi^0 \pi^0$  decays go through the beam hole. Such photons are likely to hit a veto detector with a higher inefficiency due to its high rates.

- Second, the error on the transverse momentum of  $\pi^0$ ,  $P_T$ , will be kept small. The decay vertex along the beam is reconstructed by assuming that the two photons hitting the Calorimeter has the invariant mass of  $\pi^0$ . The  $P_T$  is calculated by assuming that the decay vertex is at the center of the beam, so the error on  $P_T$  due to the finite beam size will be limited with a small beam size.
- *Require events with only two photons that together have a large transverse momentum.*  
We require  $P_T$  to be large ( $>120$  MeV/c). This requirement is useful:
  - to suppress background from  $K_L \rightarrow \gamma\gamma$  decays,
  - to require missing photons to have higher energies, and reduce the probability of missing them, and
  - to suppress  $K_L \rightarrow \pi^0\pi^0$  backgrounds where two higher-energy photons from different  $\pi^0$ 's are detected.

In order to collect more than 100 signal events, we have to improve the sensitivity from the current KTeV limit  $BR(K_L \rightarrow \pi^0\nu\bar{\nu}) < 5.9 \times 10^{-7}$  (90% CL)[1] using  $\pi^0 \rightarrow e^+e^-\gamma$  in the final state, by 6 orders of magnitude or more. Because such improvements cannot be done easily in a single step, we will pursue the experiment in a *step-by-step* approach as follows.

### 3.2 E391a

We ran a first experiment dedicated for the  $K_L \rightarrow \pi^0\nu\bar{\nu}$  decay, the KEK PS E391a experiment, using the existing 12-GeV Proton Synchrotron at KEK. As shown in Fig.8, the detector consists of a pure CsI electromagnetic calorimeter at the downstream end, and photon veto detectors surrounding the decay region, all located inside a vacuum tank. There was also a set of photon veto detectors located downstream of the calorimeter. The typical beam intensity was  $2.5 \times 10^{12}$ /pulse, and the average  $K_L$  momentum was 2.6 GeV/c.

We had three data taking runs, totaling 6 months. The first preliminary result  $BR(K_L \rightarrow \pi^0\nu\bar{\nu}) < 2.1 \times 10^{-7}$  (90% CL)[15] was obtained from one-week sample of the first physics run.

### 3.3 Step 1

The Step 1 experiment will be the first one to be run at J-Parc. We will use the  $K_L$  beam line coming off the T1 target on the A-line, along with the

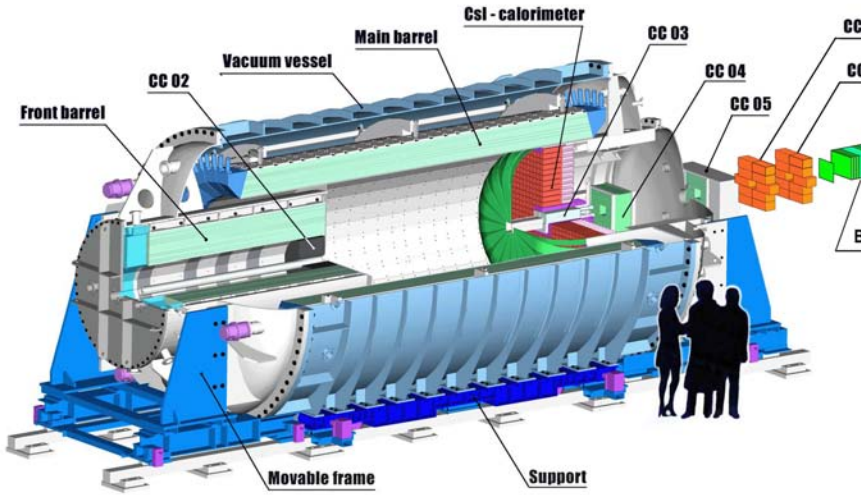


Figure 8: KEK PS E391a detector.

E391a detector with necessary modifications. The purpose of this experiment is to

- make the first observation of the signal event,
- search for new physics events with branching ratios higher than predictions from the Standard Model, and
- gain experience at the J-Parc beam line environment, in preparation for the next Step 2 experiment.

Running the Step 1 experiment at Time 0, before going to the ultimate Step 2 experiment, is also practical from the point of view of laboratory resources. We can produce physics results while the beam intensity is still low initially, and the budget for the beamline and experiments is still limited. Also, because the same target is shared by multiple slow extraction experiments, we can run simultaneously without interfering each other.

### 3.4 Step 2

After Step 1, we plan to build an optimized  $K_L$  beam line with higher yield and energy, and build a larger detector with a longer decay volume and capability for higher rates. The purpose of Step 2 is to collect more than

100 signal events, as per the Standard Model, and measure the  $K_L \rightarrow \pi^0 \nu \bar{\nu}$  branching ratio to  $<10\%$ . In this proposal, we will describe our plan on how to proceed to Step 2.

## 4 Step 1

### 4.1 Goal of Step 1

The goal of Step 1 is the first observation of  $K_L \rightarrow \pi^0 \nu \bar{\nu}$  decay with a sensitivity of  $8.0 \times 10^{-12}$ . With this sensitivity, we should be able to detect 3.5 events if its branching ratio is  $2.8 \times 10^{-11}$  as predicted by the Standard Model with the currently known parameters.

As described in Chapter 2, the  $K_L \rightarrow \pi^0 \nu \bar{\nu}$  decay is very sensitive to new physics beyond the Standard Model. A number of observed events that is significantly different from the Standard Model prediction will be evidence for new physics.

### 4.2 Beamline

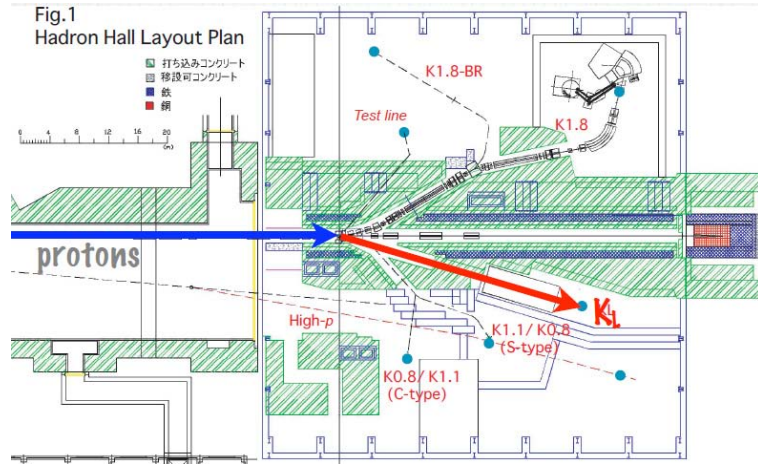


Figure 9: Layout of the hadron hall and  $K_L$  beamline.

Figure 9 shows the layout of the hadron hall and  $K_L$  beam line for Step 1. The common T1 target will be shared with other secondary beamline experiments, and with simultaneous running. Because there is a geometrical limitation in the layout of the experimental hall, the  $K_L$  beam line is extracted at  $16^\circ$  from the primary proton beam line.

The  $K_L$  beam is collimated to have a solid angle of  $9 \mu\text{sr}$ . The  $K_L$  flux at the exit of the beamline (20-m downstream of the target) is estimated to be  $8.1 \times 10^6$  per spill assuming  $2 \times 10^{14}$  protons on the T1 target. Compared to the  $4^\circ$  extraction angle at the KEK-PS K0 beam line (PS-K0), the  $K_L$  yield

per solid angle per incident proton is reduced and its momentum distribution is softer than at PS-K0. As shown in Fig. 10, the  $K_L$  momentum has a peak at 1.3 GeV/ $c$  and the average momentum is 2.1 GeV/ $c$ , lower than 1.8 GeV/ $c$  and 2.6 GeV/ $c$  at the PS-K0 line.

However, the extraction at a larger angle is an advantage because high momentum neutrons are significantly suppressed as shown in Fig. 10. Because the higher momentum neutrons have a larger probability for contributing to background, the softer momentum distribution reduces the number of neutron-induced background events.

Table 2 summarizes the parameters of the beam line.

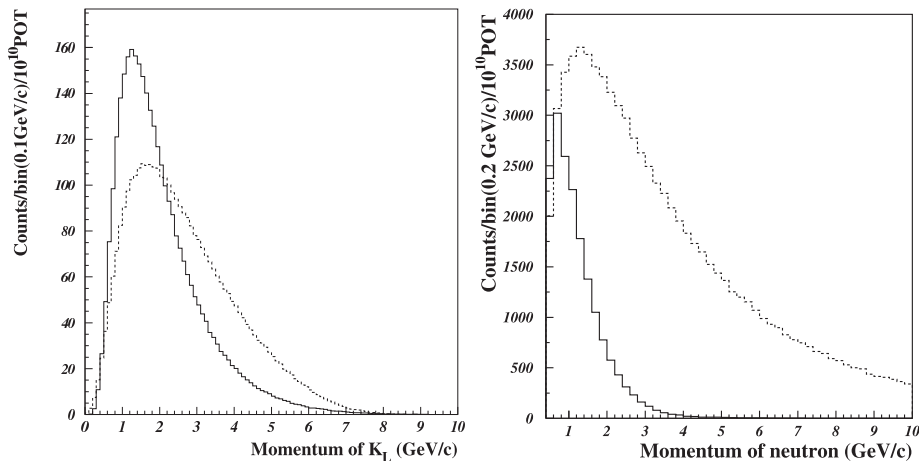


Figure 10: Momentum distribution of  $K_L$  (left) and neutron (right). The solid line is for the  $K_L$  beamline in Step 1, and the dashed line is for the PS-K0.

The total length of the beam line is 20 meters which is long enough to remove hyperon contamination and to install additional collimators for further suppression of halo neutrons.

The PS-K0 beam line has the greatest suppression of beam halo in the world, about five orders of magnitude lower than the beam core. This suppression is obtained with five stages of thick tungsten collimators as shown in Fig. 11. The amount of the beam halo is well reproduced by GEANT-based Monte Carlo calculations. Most of beamline components will be reused. Because the collimators are thick enough to prevent neutrons from passing through, the upgrade of the beamline is focused on removing a source of halo neutrons identified in the E391a experiment.

The main source of halo neutrons in the PS-K0 beam line is multiple

Table 2: Parameters of the  $K_L$  beamline for Step 1

Item	J-Parc Step 1	KEK E391a
Primary proton energy	30 GeV	12 GeV
Proton intensity	$2 \times 10^{14}$	$2.5 \times 10^{12}$
Spill length / Beam repetition	0.7 s / 3.3 s	2 s / 4 s
Production Target	Common T1 target	Pt rod ( $L=60$ mm, 8-mm $\phi$ )
Extraction angle	$16^\circ$	$4^\circ$
Solid angle	$9 \mu\text{sr}$	$12.6 \mu\text{sr}$
$K_L$ yield/spill (beam exit)	$8.1 \times 10^6$	$3.3 \times 10^5$
Average momentum of $K_L$	2.1 GeV/ $c$	2.6 GeV/ $c$
Decay probability in $3 < z(m) < 5$	3.6%	2.7%
Core Neutrons/spill		
$E_n > 0.1$ GeV	$3.4 \times 10^8$	$2.0 \times 10^7$
$E_n > 1$ GeV	$6.9 \times 10^7$	$1.4 \times 10^7$

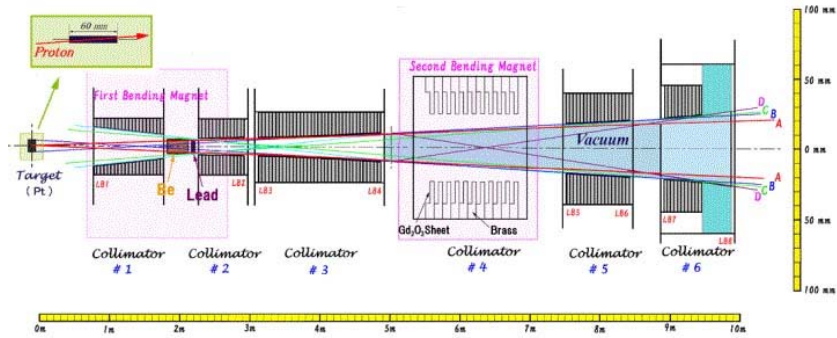


Figure 11: Schematic view of KEK-PS K0 beam line for E391a.

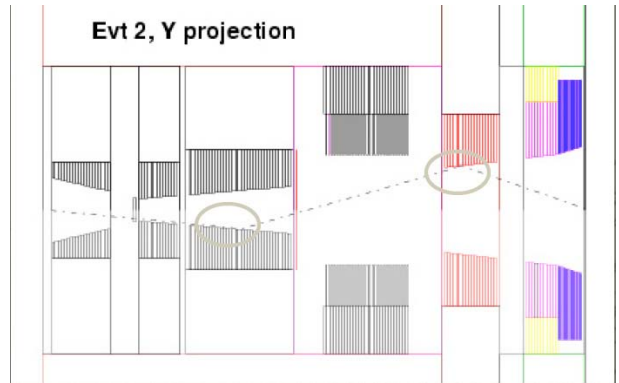


Figure 12: An example of a halo neutron event found in the Monte Carlo simulation for the PS-K0, which is caused by multiple scattering at the surface of collimators.

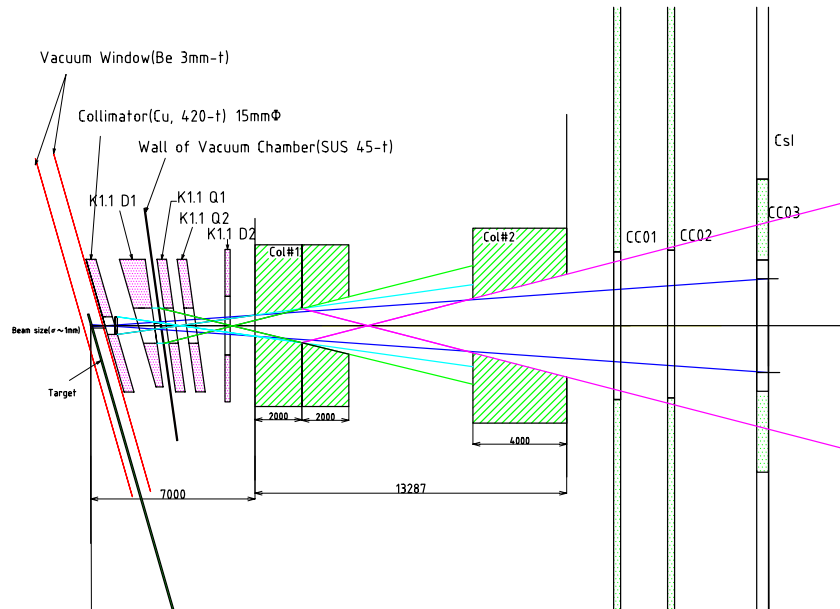


Figure 13: Conceptual design of the beam line for Step 1.

scattering at the surface of the collimator as shown in Fig. 12. In order to remove the halo neutrons, the collimators in **Step 1**, will be arranged as shown in Fig. 13. With this design, the neutrons scattered in the first half of the first collimator will not hit the inner surface of the second collimator. (The rate of neutrons scattered at the second half of the first collimator should be low, because its inner surface is not visible from the target.) Our goal is to reduce the ratio of halo to core neutrons by another factor of 5. If this goal is achieved, the number of halo neutrons increases by only a factor of 3.4, while the number of  $K_L$ 's increases 24.5 times compared to those of the PS-K0.

### 4.3 Detector

Figure 14 shows a schematic view of the detector setup after upgrading the existing E391a detector. Here, we define our coordinate system. The  $z$  axis is the center of the neutral beam line,  $+z$  pointing downstream. The origin is set at the upstream surface of the "Front Barrel". The positive  $y$  direction points vertically up, and the positive  $x$  direction is defined in the right-handed coordinate system.

We will use the same concept as in E391a, which is summarized as follows:

- Hermetic veto system completely enclosing the decay region;
- Double decay chambers;
- Highly evacuated decay region;
- High detection efficiency for photons and charged particles.

The  $\pi^0$  in the  $K_L \rightarrow \pi^0 \nu \bar{\nu}$  decay is detected by measuring the positions and energies of two photons with the CsI Calorimeter. Because most of the other  $K_L$  decays are multiparticle final states (*e.g.*,  $2\pi^0$ ), they will be rejected by detecting additional photons and/or charged particles with a hermetic veto system. In order to reject  $K_L$ 's that decay upstream of the fiducial region, we adopt a double decay-chamber scheme. The main decay chamber is enclosed by Main Barrel (MB), and an upstream chamber consists of counters CC01, CC02, and a Front Barrel (FB). In order to detect photons escaping through the beam hole, a series of collar counters (CC04, CC05, and CC06) and the Beam Hole Veto (BHCV and BHPV) counters are located downstream of the Calorimeter.

Another background is  $\pi^0$  production from beam neutrons interacting with residual gas in the decay region. In order to suppress this background, the decay volume is evacuated to  $10^{-5}$  Pa, as was obtained in E391a by separating the detector and the decay region with a thin film.

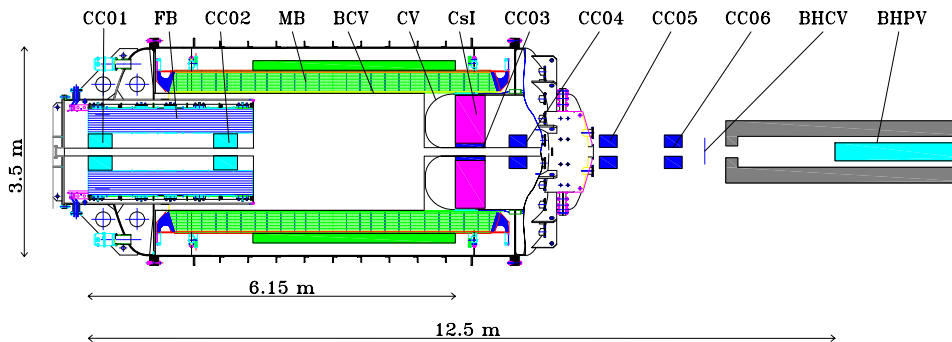


Figure 14: Schematic view of detector setup.

#### 4.3.1 Calorimeter

The electromagnetic calorimeter measures the positions and energies of photons to reconstruct  $\pi^0$  in the  $K_L^0 \rightarrow \pi^0 \nu \bar{\nu}$  decay. In the E391a experiment, the Calorimeter was made of 576 pure CsI crystals. Each crystal was  $7.0 \times 7.0$  cm<sup>2</sup> and 30-cm long ( $16 X_0$ ) [59].

For the experiment at J-PARC, we plan to replace these crystals with the pure CsI crystals used in the calorimeter of the Fermilab KTeV experiment. The crystals, called “KTeV CsI crystals” hereafter, are smaller in the cross section and longer in the beam direction (50 cm,  $27 X_0$ ) than the crystals in E391a, which ensures us much better performance in the new experiment. Figure 15 shows the layout of the new Calorimeter, which then consists of 2576 crystals. These crystals are of two sizes,  $2.5 \times 2.5 \times 50$  cm<sup>3</sup> for the central region (2240 blocks), and  $5.0 \times 5.0 \times 50$  cm<sup>3</sup> for the outer region (336 blocks) of the Calorimeter.

The reasons for replacing the calorimeter are as follows.

- *Reduce the probability of missing photons due to fused clusters.*

If two photons hit the Calorimeter close to each other, the generated showers will overlap and be misidentified as a single photon. Figure 16 shows an event display for two photons that enter the CsI Calorimeter with 6-cm separation. By using the KTeV CsI crystals, two photons

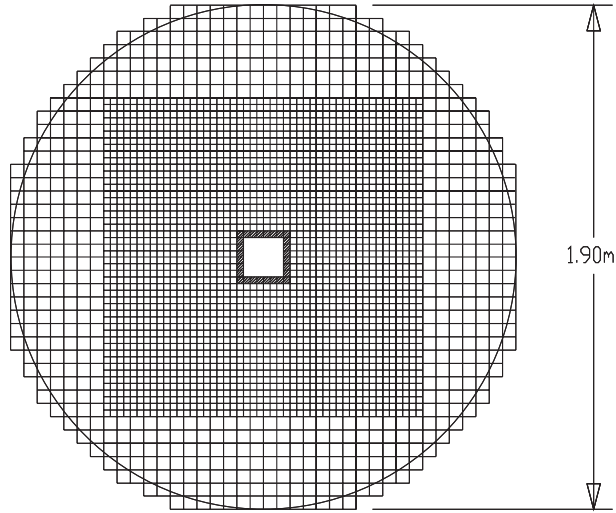


Figure 15: Layout of the Calorimeter for the J-PARC experiment with the KTeV CsI crystals. The  $2.5 \times 2.5 \times 50\text{-cm}^3$  crystals are used for the inner region, and  $5.0 \times 5.0 \times 50\text{-cm}^3$  crystals are used for the outer region.

as close as  $\sim 5$  cm can be identified as two clusters, compared to  $\sim 15$  cm in E391a. Each cluster is required to have a transverse energy distribution consistent with an electromagnetic shower, which is easier to achieve with KTeV crystals.

- *Eliminate the photon detection inefficiency due to punch-through.*  
In the case of the 30-cm-long ( $16 X_0$ ) crystals used in E391a, the probability that a photon passes through a crystal without interacting is comparable to the inefficiency due to photonuclear interactions. However, with the 50-cm-long ( $27 X_0$ ) crystals, the probability is reduced to a negligible level as shown in Fig. 17.
- *Reduce background due to shower leakage.*  
When a photon hits a calorimeter, some part of the shower leaks from the back. The amount of the leakage depends on the depth where the first  $e^+e^-$  pair in the shower is created. Because the decay vertex is reconstructed by assuming a  $\pi^0$  mass, the energy leakage shifts the decay vertex downstream. The  $\pi^0$ 's produced by halo neutrons in CC02 are then reconstructed as if they were from the decays inside of the fiducial region. As shown in Fig. 18 (Left), the longer KTeV CsI

crystals will have significantly less leakage, and thus suppress such a background.

In E391a, we performed a special run to calibrate Calorimeter with known vertex position, in which a 5mm-thick aluminum plate was inserted in the beam at 5.5 cm downstream of CC02, as a  $\pi^0$  production target. As indicated in Fig. 18 (Right), we observed a long tail in the reconstructed vertex distribution, extending far downstream. This can be explained by the energy leakage behind the Calorimeter. By using longer crystals, we can reduce the tail, as indicated by the hatched histogram (expected by our simulation) in the figure. As well as narrower width by better position resolution, this improvement of the vertex reconstruction is quite effective to reduce backgrounds due to halo neutrons interacting with CC02, which is one of the major backgrounds observed in E391a.

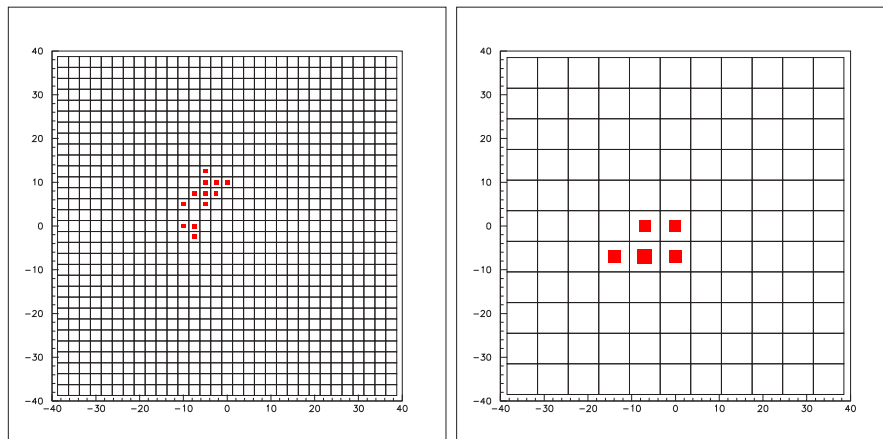


Figure 16: Event display for two photons in the calorimeter close to each other for Step 1 (Left) and E391a (Right).

The Calorimeter has a square beam pipe at the center to let the neutral beam pass through. The beampipe is made of an ultra-high modulus carbon fiber/epoxy combination (4mm thick). It serves the purpose of supporting the weight of the crystals ( $\sim 210$  kg) with minimum dead space. The beam pipe is surrounded by an upgraded veto counter (Collar counter, CC03) as described in Sec. 4.3.4. Figure 19 shows one of the configurations around the square beampipe. In this option, the two most inner rows and columns

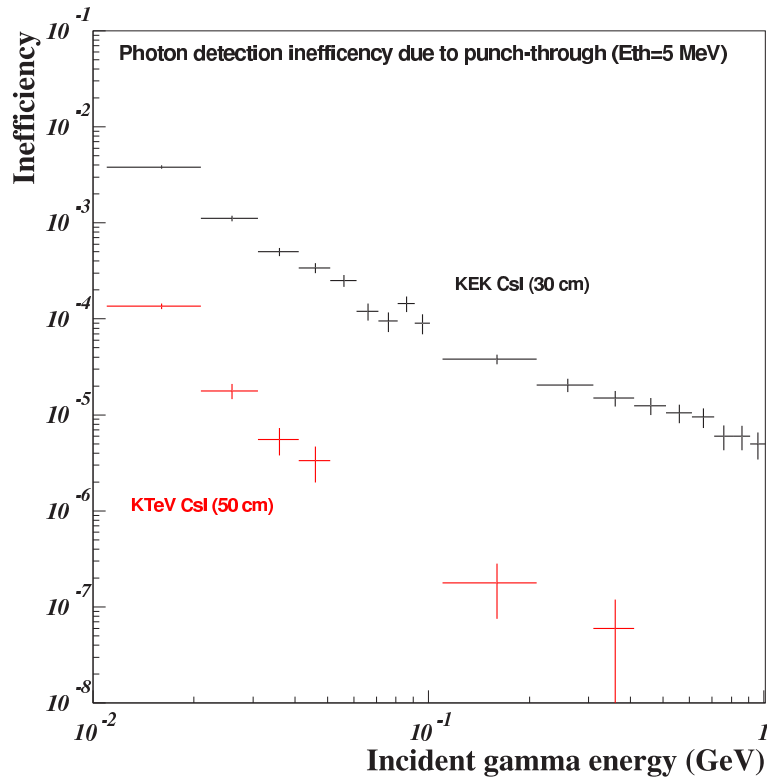


Figure 17: Photon detection inefficiency of the Calorimeter due to punch-through. In the KTeV CsI crystals, the inefficiency is negligible compared to that due to photonuclear interactions, while these inefficiencies are comparable in the E391a CsI crystals.

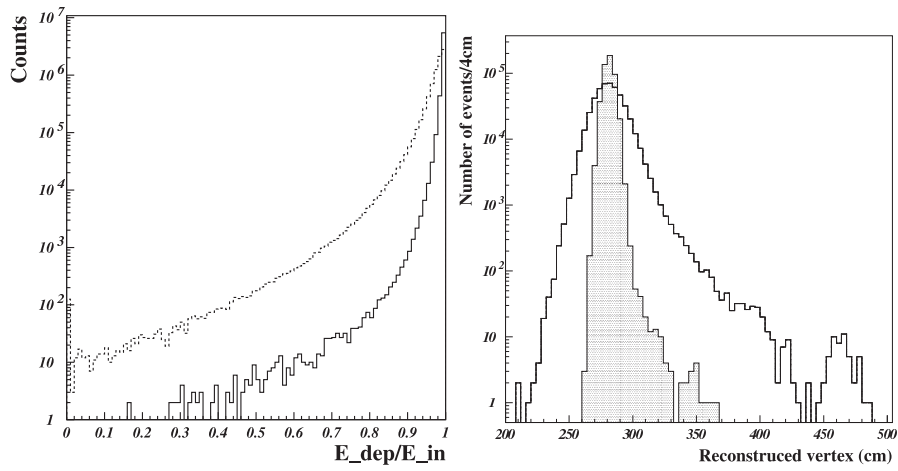


Figure 18: Monte Carlo study of the shower leakage. Left: the ratio between the deposited energy in the CsI crystals and the true incident energy for the photons in the energies between 0.1GeV and 1GeV. The dotted line is for E391a crystals ( $16 X_0$ ), and the solid line is for KTeV crystals in Step 1 ( $27 X_0$ ). Right: reconstructed vertex distribution for  $\pi^0$  events produced by an aluminum plate located downstream of CC02 (true position = 280.5 cm in the plot) only during calibration runs for E391a (open histogram) and for Step 1 (hatched histogram).

surrounding the beampipe will have 112 blocks of  $1.25 \times 1.25 \times 50 \text{ cm}^3$   $\text{PbWO}_4$  crystals. Another option is to use a spaghetti-type counter.

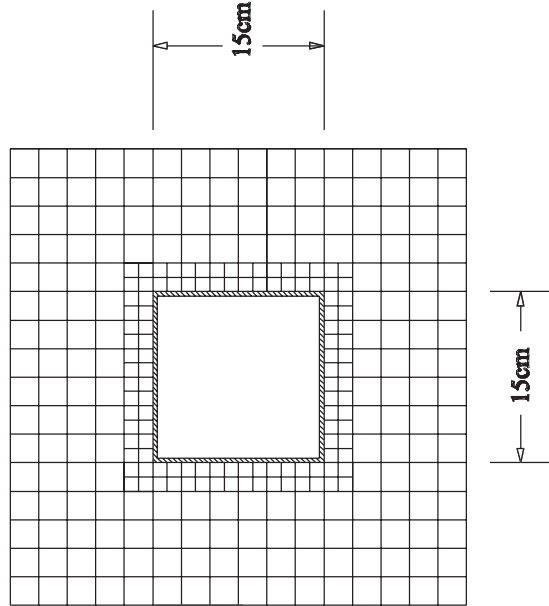


Figure 19: Layout of the CsI around the beam-hole region of the Calorimeter. In this configuration, the inner-most 2.5-cm layer consists of  $1.25 \times 1.25 \times 50.0\text{-cm}^3$   $\text{PbWO}_4$  crystals, a total of 112 blocks. The square carbon fiber pipe is 4 mm thick.

In the KTeV experiment, the scintillation light from each CsI block was collected by 5-stage 3/4" R5364 Hamamatsu phototubes for the small crystals, while 6-stage 1.5" R5330 tubes were used for the larger crystals. The signal was read out by a device named "digital photomultiplier tube" (DPMT), in which the PMT anode was connected by a very short cable (a few cm) to a circuit that digitized the signal, buffered the digitized value, and transmitted it on demand. It involved two ASICs and was operated synchronously with the beam RF of Tevatron at 53 MHz. However, it is important to note that this technique provided the timing of only  $\sim 5$ -ns precision. The position and energy resolutions achieved were  $\sim 1$  mm and  $\sim 2\%$ , respectively, for 1-GeV electromagnetic showers. Details of the calibration and performance of the calorimeter in the KTeV experiment are documented in Ref. [58].

Due to the requirements on vacuum, cooling, and timing for the proposed

experiment, we plan to reinstrument each CsI block, retaining only the crystals and the phototubes from the KTeV calorimeter system. New bases, HV and signal cables, and front/back-end electronics will be redesigned. To reduce the total number of HV cables, a special system to distribute HV directly to the dynodes may be employed. A short length ( $\sim 1$  meter) of anode cable carries the signal from a phototube base to a pulse shaper and an asynchronous waveform digitizer located outside the vacuum vessel, as described in Sec. 4.4. We expect the timing resolution of better than 1 ns while retaining the position and energy resolutions by the new calorimeter with KTeV crystals.

### 4.3.2 Barrel Photon Veto

The Barrel Photon Veto surrounds the decay volume to detect additional photons from  $K_L$  decays. In order to cover the large volume of the fiducial region, this detector is made as a sampling calorimeter with alternating lead and plastic-scintillation plates. Two different sets of detectors are used to form a double decay chamber, the *Front Barrel* and the *Main Barrel*.

We will transfer the Front and Main Barrels for the KEK PS E391a experiment to J-Parc, and apply necessary modifications for Step 1.

The Main Barrel for E391a is made of 32 modules. Each module consists of 5-mm-thick scintillator plates and lead plates that are 1-mm thick for the inner 15 layers and 2-mm thick for the outer 29 layers. The total thickness of the module is 14 radiation lengths ( $X_0$ ), and the length is 5.5 meters. In the most inner part of the Main Barrel, a pair of scintillators (Barrel Charged Veto, or BCV) are located to identify charged particles. Figure 20 shows drawings of the Main Barrel module and of the full assembly.

Wavelength shifting (WLS) fibers are used to read out the scintillation light. We have developed a Green-extended high-QE PMT having a prism-type photo-cathode, which increases the photoelectron yield by a factor of 1.8 [60]. We attached PMTs to both ends of the module, separately for the BCV, inner, and outer modules (6 channels for one module). A light yield of 13.8 photoelectrons was obtained at the center of a module for a 1-MeV energy deposit (Fig. 21). By using cosmic ray data, the timing resolution was obtained as 0.6 ns for the inner module and 0.5 ns for the outer module, respectively. Details of main barrel performance is reported in [61]. In the E391a data, the response of the Main Barrel down to a 1-MeV deposit is well reproduced by Monte Carlo simulation as shown in Fig. 22.

For Step 1, we will improve the Main Barrel in two ways:

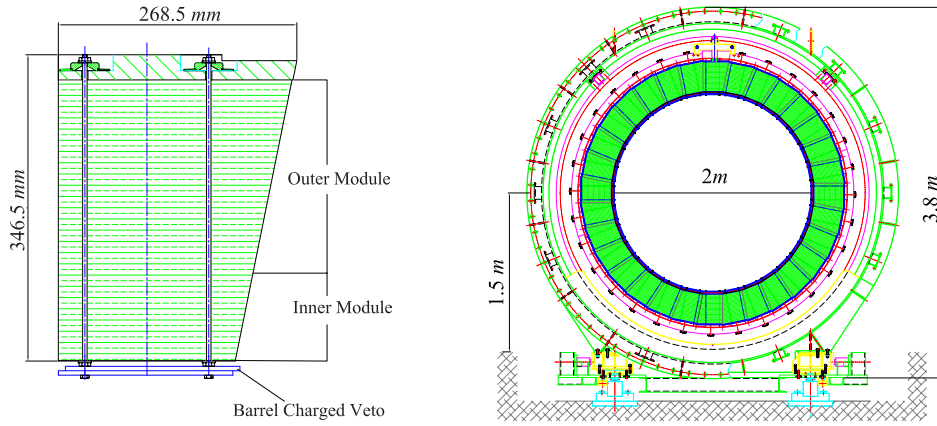


Figure 20: Left: A module of the Main Barrel. Right: Cross section of the Main Barrel.

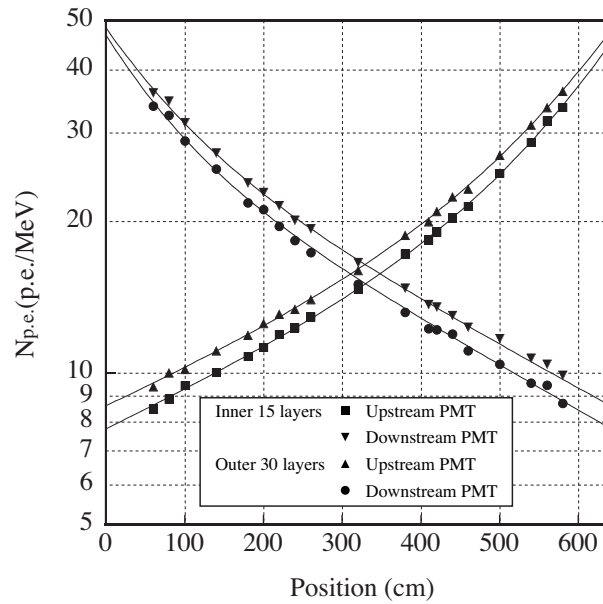


Figure 21: The light yield of the Main Barrel as a function of distance from the PMT.

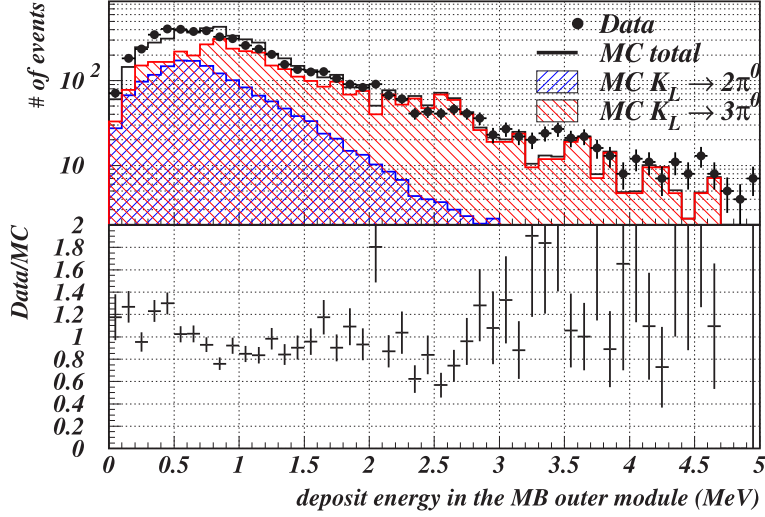


Figure 22: Top: The distribution of the energy deposit in the Main Barrel for the data (dots) and Monte Carlo (M.C.) results to  $K_L \rightarrow \pi^0\pi^0$  decay (blue hatched) and  $K_L \rightarrow \pi^0\pi^0\pi^0$  decay (red hatched). Bottom: Ratio of the data to M.C.

- Pipeline readout of the pulse shape with waveform digitizers.
- Addition of extra layers behind the Main Barrel.

Because the Main Barrel is a long detector, timing provides important information to prevent acceptance loss due to accidental hits and back-splash. In E391a, we observed *back-splash* that arises from particles generated as a part of the Calorimeter shower that enter back into the Main Barrel, as shown in Fig. 23. This back-splash, which is a main source of acceptance loss due to vetoing from the Main Barrel, is well identified when we use timing information. As shown in Fig. 24, the correlation between incident position and time of the back-splash is opposite to that of real photons. However, the timing information obtained from TDC is frequently destroyed in a high-rate environment due to pile-up of signal specially for a large detector like Main Barrel. It is important to get timing information for small signals without significant dead time caused by discrimination, which will be achieved through a pipeline readout of the pulse shape with waveform digitizers.

To improve the efficiency for photon detection, more layers will need to be added because the thickness of Main Barrel is only  $14 X_0$ . By adding additional layers behind the current Main Barrel, the photon detection inef-

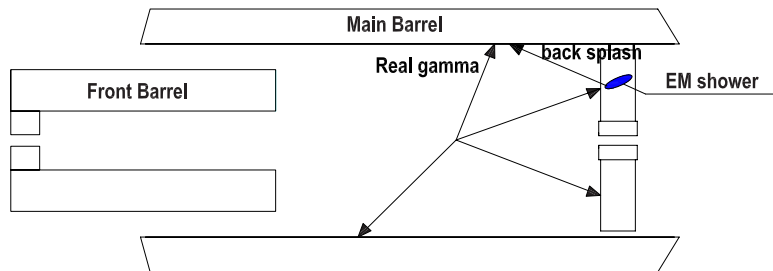


Figure 23: Schematic view of a shower back-splash.

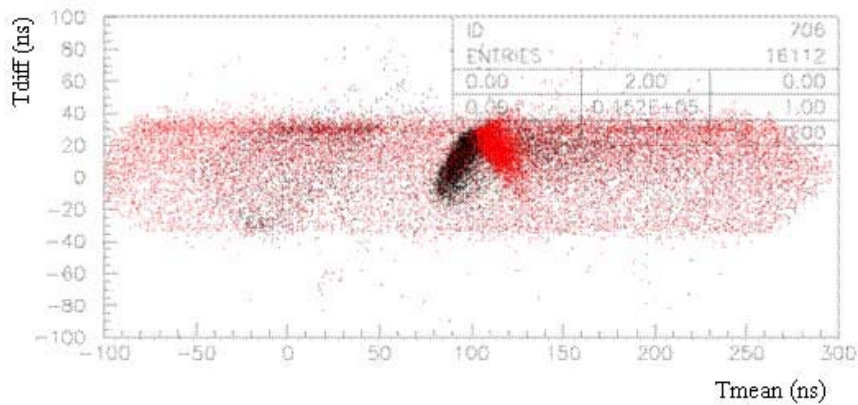


Figure 24: Distribution of incident time (horizontal axis) and the effective incident position (vertical axis; downstream points up) for photons hitting the Main Barrel for the events in which 4 photons are detected in the Calorimeter in the E391 data. The black dots represent the photons from decays. The red dots represent the back-splash, as the timing is later for upstream hits.

efficiency due to punch-through will be greatly improved as shown in Fig. 25. We will use the current vacuum chamber with a little modification.

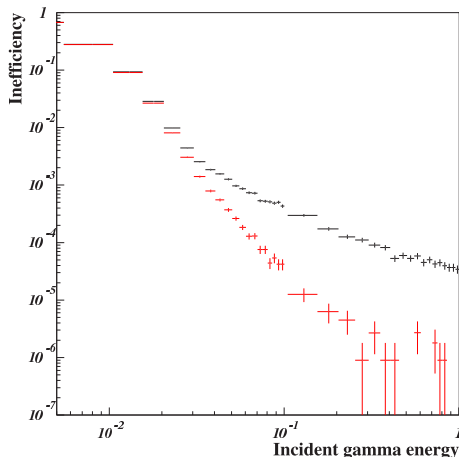


Figure 25: Comparison of the  $\gamma$ -detection inefficiency of the Main Barrel between E391a and Step 1. In Step 1, we will add additional modules made of 5 layers of alternating 5-mm-thick lead and 5-mm-thick scintillation plates. Black points are the inefficiency of the E391a Main Barrel, and red ones are for Step 1.

As shown in Fig. 26, the Front Barrel and the collar counters CC01 and CC02 form an upstream decay chamber in order to suppress  $K_L$  decays in front of the fiducial region. As shown in Fig. 27, the Front Barrel consists of 16 trapezoidal-shaped modules that are made of 59 layers of alternating lead and plastic-scintillator plates (16.5  $X_0$  thickness and 2.75 meters long). The light yield is obtained as 20 (10) photoelectrons per 1-MeV deposit at the nearest (farthest) point from the PMT.

Table 3 summarizes the parameters of the Barrel Photon Vetos.

### 4.3.3 Charged Veto

Most  $K_L$  decays include charged particles such as  $K_L \rightarrow \pi^+\pi^-\pi^0$  (12%),  $K_L \rightarrow \pi^\pm\mu^\mp\nu$  (27%), and  $K_L \rightarrow \pi^\pm e^\mp\nu$  (40%), and these decays can become backgrounds both in the trigger stage and in the analysis stage. For example,  $K_L \rightarrow \pi^+\pi^-\pi^0$  contains a  $\pi^0$  in the final state and can fake the signal of interest if the two charged pions are missed. Thus, the decay region must be surrounded by charged particle veto detectors, as well as photon veto detectors. There are three categories of charged detectors: the main

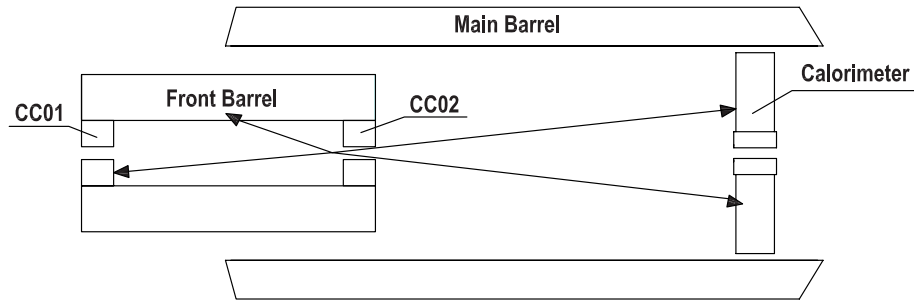


Figure 26: Schematic view of the role of the upstream decay chamber.

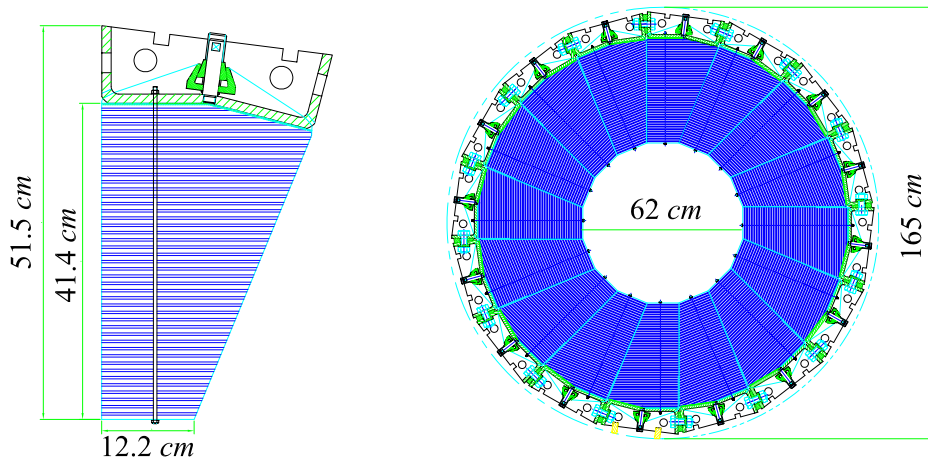


Figure 27: Left: A module of Front Barrel. Right: Cross section of the Front Barrel.

Table 3: Parameters of Barrel Photon Vetos. The thicknesses of the lead and scintillator sheets are show in parentheses.

	Front Barrel	Main Barrel (E391a)	Main Barrel (Step 1 )
Length (m)	2.75	5.5	5.5
Outer diameter (m)	1.6	2.8	3.0
Inner diameter (m)	0.6	2.0	2.0
No. of modules	16	32	32
No. of channels	32	128	192
No. of Scin. layers	59 (5 mm)	45 (5 mm)	51 (5 mm)
No. of lead layers	58 (1.5 mm)	15 (1 mm) 29 (2 mm)	15 (1 mm) 29 (2 mm) 5 (5 mm)
Thickness ( $X_0$ )	16.5	14.0	18.5
Module mass (kg)	850	1,500	1,940

Charged Veto (CV) which covers the Calorimeter, the Barrel Charged Veto (BCV) which lines the Barrel Photon Veto, and the Beam Hole Charged Veto (BHCV), which will be described in a later section.

The CV consists of two layers of hodoscopes, each of which is a 5-mm-thick plastic scintillator array aligned in horizontal and vertical directions, as shown in Fig. 28. In the region that does not include the beam hole, there are twelve 15-cm-wide scintillator slabs in a layer. Both ends of a slab are bent and extended to the downstream region along the outer circumference of the Calorimeter and are read out by photomultipliers. The region in the horizontal (vertical) line of the beam hole is covered by two 7.5-cm-wide counters in each side. In order to be read from both ends, their inner ends are extended to the downstream region, lining the inside wall of the Calorimeter, while their outer structure is the same as others. This scheme of reading out from both ends enables us to obtain good timing information, and thus to set tight veto windows which are important in the high-rate environment of the experiment. Furthermore, we can calculate the hit position in one scintillator by using the time difference of both ends, which is useful for distinguishing signals and back-splashes from the Calorimeter. The CV is located 50 cm upstream of the Calorimeter surface in order to resolve two photons from  $e^+$  annihilation and/or  $\pi^0$ s from  $\pi^-$  charge exchange interactions in the CV material, and thus to prevent  $K_L \rightarrow \pi^\pm e^\mp \nu$  from faking a real signal.

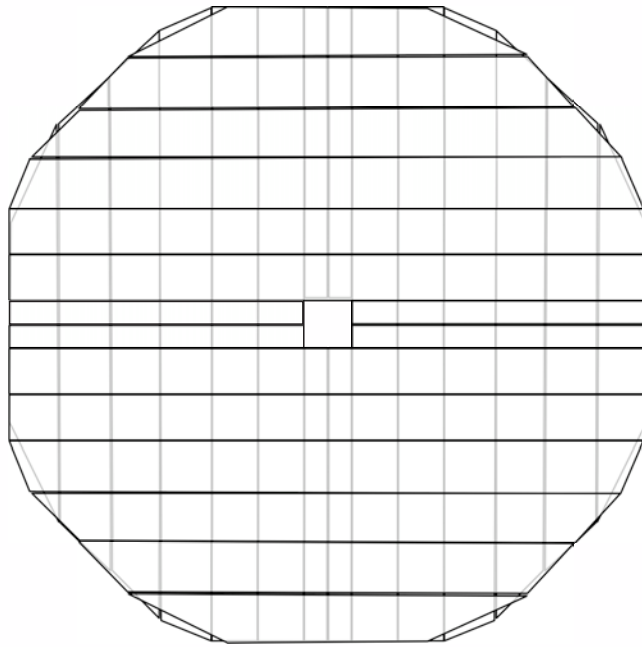


Figure 28: The schematic drawing of the Charged Veto in front of the Calorimeter (CV).

The BCV is a liner of the Barrel Photon Veto Counter, the same as used in the E391a experiment. It consists of 32 plastic scintillators 20-cm wide by 550-cm long by 1-cm thick. There are 38 wavelength shifting fibers in each slab, embedded in a longitudinal direction, and they are collected onto photomultiplier tubes with a prism photocathode at both ends.

From the E391a experiment we have learned the performances of charged particle detectors, such as the achieved light yield and counting rate, and we can use these parameters for estimating the performances in the J-PARC experiment. The expected efficiency of the Charged Veto counter will be described in Appendix A.3.

#### 4.3.4 Collar Counters

We will arrange collar counters, which are sensitive to both charged particles and photons, along the beam as in E391a. Their crucial roles are not only to cover the gap near the beam region tightly, but also to prevent a true signal from being rejected by beam-induced activities. Typical examples of the latter role are a reduction of the halo neutrons by CC01 and CC02, a shield against products from  $K_L^0$  decays along the beam near the CsI calorimeter by CC03, and a shield against the back-splash from the BHPV by the downstream collar counters. The flexibility to take care of special demands for each collar counter is a principal merit of the present plan to arrange several separate collar counters. Another merit is that they are relatively small in size to fabricate and to modify later.

At present we have a basic plan for the collar counters as follows. We will reuse the CC02 of E391a and add CC01. Both are Shashlik-type counters with the lead sheets in the direction perpendicular to the beam. We are considering two options for CC03, PWO crystals or a spaghetti-type counter that has tungsten and scintillator fibers as shown in Fig. 29. The lamination direction of CC04 must be perpendicular to the beam, because it must mask the stacking gaps in CC03. For the downstream collar counters after CC04, we are planning to reuse the CsI blocks used for the E391a calorimeter. A single and separate readout of the first layer of scintillator of the downstream collar counters is necessary to make a tight veto for charged particles, especially to reject the background from the decay  $K_L^0 \rightarrow \pi^+\pi^-\pi^0$ . A smaller leakage from the rear end of the CsI calorimeter is a very important advantage compared to E391a, where we were perhaps overly cautious about the leakage of true photon signals through relatively thin CsI crystals.

The single-counting rates, estimated by extrapolating the rate observed in E391a, are kept at a tolerable level for all of the collar counters except

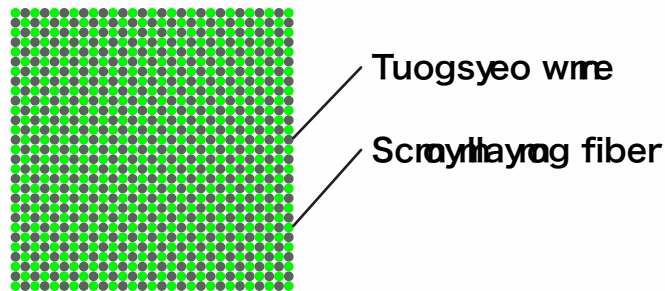


Figure 29: An option of CC03 which is made of alternating tungsten wires and scintillating fibers.

for CC07. The most downstream counter CC07 received very strong back-splash from the BA (name of BHPV at E391a). We will install the BHPV inside the cave as shown in the setup.

#### 4.3.5 Beam Hole Veto

The purpose of the Beam Hole Veto detector is to detect extra particles in the  $K_L$  decay which escape through the beam hole. It is placed in the neutral beam at the end of our detector system. Because it is exposed to a high flux of neutrons,  $K_L$ 's, and beam photons, there would be a high probability of generating fake hits, which inhibit a proper function of the detector. Thus, the detector should be insensitive to those unwanted particles, while keeping a high sensitivity to products from  $K_L$  decays in the fiducial volume. The detector consists of two components; one is for the detection of charged particles, and the other is for photons.

**Beam Hole Charged Veto counter (BHCV)** The BHCV is set at 4 m downstream of the CsI Calorimeter, where the neutral beam size is about 10 cm in diameter. The current design of the BHCV is based on the usual techniques of charged particle detection. It is composed of 2 (horizontal) by 8 (vertical) slabs of plastic scintillators, each of which has a dimension of 10 cm (horizontal) by 2.5 cm (vertical) by 3 mm (thickness), and thus covers the region of  $\pm 10$  cm from the beam axis. Each scintillator is read out by a photomultiplier tube attached at one end. According to the experience in the E391a experiment, its counting rate is estimated to be about 1 MHz per counter for energy deposits of more than 300 keV. As discussed in Appendix A.3, the expected efficiency of the BHCV is estimated to be 99.5%, where

the source of inefficiency is dominated by masking effects due to the high counting rates.

**Beam Hole Photon Veto (BHPV)** The Beam Hole Photon Veto counter is at the downstream end of our detector system. It starts at 6.3 m downstream of the CsI calorimeter, corresponding to about 34 m from the target. At this point, the diameter of the neutral beam is 11.6 cm and the BHPV should cover this region. In order to suppress shower components going back to the Calorimeter, the BHPV will be placed in a shield.

The BHPV is designed on a new concept of photon detection. One feature utilizes Čerenkov radiation to detect electrons and positrons produced by an electromagnetic shower. This feature enables us to be blind to heavy (and thus slow) particles, which are expected to be the main products in neutron interactions. The other feature is to use directional information. Photons to be caught and vetoed come from the fiducial region 6 m or more upstream through a narrow beam hole, and thus their electromagnetic showers are spread over in the forward direction. On the other hand, secondary particles from neutron interactions tend to go isotropically. Therefore, neutron signals can be reduced further, without losing photon efficiency, by requiring shower development along the beam direction.

Based on this concept, the BHPV is designed to be an array of Pb-Aerogel counters. Figure 30 shows the schematic view of the BHPV module. Each module is composed of 2-mm-thick lead as a photon converter, a stack of aerogel tiles as a Čerenkov radiator, a light-collection system of a mirror and a Winston cone, and a 5-inch photomultiplier tube. In order to identify a genuine signal when it is smeared by accidental hits, 500-MHz waveform digitizers are used in the readout.

The aerogel array has a cross section of 30 cm by 30 cm, a thickness of 5 cm, and the refractive index of 1.03. These modules are lined up in 25 layers along the beam direction, each of which is placed 35 cm apart as shown in Fig. 31. The total length and thickness of the BHPV are 8.75 meters and  $8.9 X_0$ , respectively. This configuration enables us to select events that have their shower development in the forward direction, and thus reduce the sensitivity to neutrons. The parameters of the BHPV are summarized in Table 4.

A full-size prototype of the BHPV module was constructed and tested in the actual neutral beam during the third period of the E391a experiment (Run III). Even though the intensity was 25 times of lower than that expected in Step 1 at J-PARC, we were able to examine various performances,

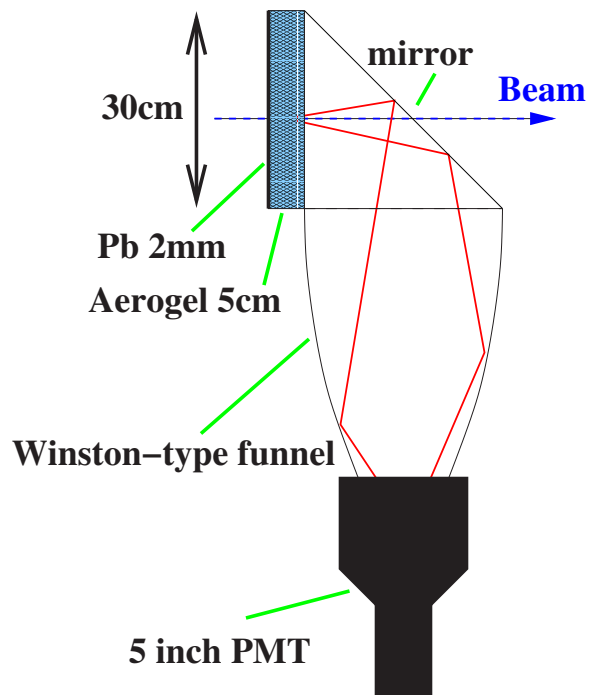


Figure 30: Schematic view of the BHPV module.

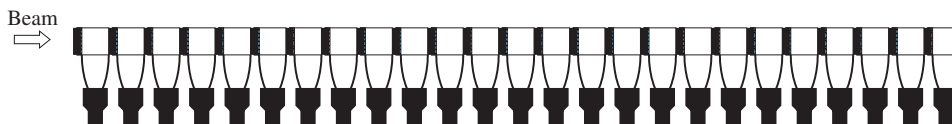


Figure 31: Schematic side view of the BHPV arrangement.

Table 4: The base parameters of the BHPV.

Items	Parameters
size of module	30 cm (H) by 30 cm (V)
Pb converter	2-mm thick
aerogel	refractive index=1.03 30 cm (H) by 30 cm (V) 10-mm-thick×5 tiles
main mirror	flat, 45° degree inclined
light funnel	Winston cone ( $d_{in}$ =30 cm, $d_{out}$ =12 cm)
photomultiplier	Hamamatsu R1250 (5-inch)
number of modules	25
layer spacing	35 cm
size in beam direction	875 cm
radiation length	8.9 $X_0$

such as the light yield for photons and the gain stability, and found that it worked according to expectations. In addition, the counting rate was well reproduced, without unknown excess, by a E391a beam simulation and BHPV detector simulation. This result enables us to conclude that we can understand the BHPV performance in the beam line and to be convinced of the validity of our expectation in Step 1 at J-PARC, which is described in detail in Appendix A.4.

#### 4.3.6 Vacuum

There are two tight requirements for the vacuum in the proposed experiment: a high vacuum of  $10^{-5}$  Pa along the beam axis, and a very thin ( $\leq 50$  mg/cm<sup>2</sup>) layer of dead material in front of the detectors. The former is required for reducing interactions of the beam with the residual air. The latter requirement is for reducing the detection inefficiency for decayed particles that could be absorbed in the dead material. We will use the “differential pumping method” developed in the E391a experiment, where we have two different vacuum levels across a thin layer.

We will be able to reuse much of the equipment from E391a, such as the pumps, duct, *etc.*. The separator between the high- and low-vacuum regions, a membrane, should be newly fabricated to match the changes of

the detector setup and to improve its supporting system.

#### 4.4 Frontend electronics, Trigger, and DAQ

In the proposed experiment, events will be accumulated not only for the  $K_L \rightarrow \pi^0 \nu \bar{\nu}$  decay, but also for other decays such as  $K_L \rightarrow \pi^0 \pi^0$  and  $K_L \rightarrow \pi^0 \pi^0 \pi^0$  for calibration and monitoring. The rates from  $K_L$  decays are expected to be several MHz. Upgrades of the frontend electronics, trigger and DAQ are major parts of the upgrades from the E391a.

##### 4.4.1 Electronics

Waveform digitization will be necessary to distinguish pile-up signals from legitimate two-photon signals under the high-rate conditions we expect to have. The precise timing information for each signal will help to identify and separate the events, and to reduce losses arising from accidentals in the high counting rates of the detectors. Multihit TDCs will also be necessary with these conditions.

VME-based frontend electronics are currently being considered for the entire DAQ system, instead of the FASTBUS, CAMAC and TKO systems that have been widely used in the past, in order to avoid complications of the system management between different electronics standards, either for the hardware or the software.

In order to reduce the dead-time during data acquisition, fully-pipelined electronics modules are required.

**Waveform Digitizer.** The number of channel for the waveform digitizer is dominated by the CsI calorimeter. Basically there are two known techniques. The first is the “digital scope” method, *i.e.* each phototube signal will be digitized by a  $\sim 500$ -MHz FADC. The major concerns here will be cost and the immediate processing power for the throughput. The second method takes advantage of a sophisticated electronic filter. That is, the well defined pulse shape from the CsI light/phototube, when input to a 7-pole Bessel low-pass LC filter, will produce a fixed-width Gaussian shaped output pulse. This technique has been used by the LHC ATLAS hadron calorimeter Tilcal group, and considerable data have been published about the performance. With a Gaussian shaped output, one could use a lower-speed FADC for the sampling for both timing and charge information. For the CsI calorimeter,  $\sim 50$  MHz will be adequate. A timing resolution of better than 1 ns was achieved by the Tilcal group. For overlapping pulses,

the filter technique seems to work as well as the conventional one. Studies on performance, cost, and system issues are needed before a choice can be made. The digital backends for the FADC implementation include a COPPER-II platform [62] where add-on modules can be added, or FPGA (field-programmable gate array)-based digital processors. We plan to build prototypes and measure the performance with beam tests.

The cables to and from the waveform digitizers should be as short as possible to avoid undesirable noise on the signal lines so that the signal pulse shapes are not significantly distorted. Because the detector is located inside the vacuum, vacuum feedthroughs for the signal cables are mandatory. The waveform digitizers must be located outside the vacuum, and the feedthroughs might distort the pulse shapes. The effect of feedthroughs on the distortion of the signal shape for the waveform digitizers will also be examined in the beam tests.

**Multihit TDC.** We will measure the timing of signals with multihit TDCs with a timing resolution of  $\sim 1$  ns. Although this timing measurement is redundant with that provided by the waveform digitizers, it has some advantages. First, the timing resolution is better than the resolution obtained from a waveform analysis using 500-MHz FADCs. Second, multihit TDCs will also be able to record longer time periods such as tens of  $\mu\text{s}$  and with less data output than those waveform digitizers. Because accidental activities will be one of the limitations of the experiment, particularly for high-rate conditions, it is crucially important to have redundancy checks with different systems such as waveform digitizers and multihit TDCs.

A prototype of pipeline TDC modules [63], which was originally developed for the CDF experiment, is a possible candidate. It has 96 channels per board, each channel of which has 10-hits of buffer depth per trigger, and has  $\sim 1.2$  ns of timing resolution. The FPGA-based signal processor allow us the further modification of the signal processing scheme if we require better performance.

Another possibility is the COPPER-II platform. It has recently been developed at KEK as the next-generation DAQ system for near-future experiment at such as Super B-factory, J-PARC, LHC, etc.. It consists of a VME 9U-size mother-board which mounts the add-on modules for analog-to-digital(A/D) signal processor, trigger controller, CPU and network-interface modules. Various kinds of signal processors such as FADCs and TDCs are being developed and tested. Among them, Time Memory Cell(TMC)-based pipeline-TDC add-on module, which utilises the AMT3 chip developed for

LHC ATLAS experiment, will be applicable for our experiment. It has 24 channels per add-on module, and each channel has 0.8 ns of timing resolution with at maximum 256 depth of buffer. If we require even better performance, custom-made add-on module could be developed with little difficulty and costs, because only the A/D processing part, not the entire function of the module, has to be developed as a small add-on module, thanks to the “add-on” scheme of the COPPER-II platform.

#### 4.4.2 Trigger and DAQ

A multi-stage triggering scheme has been adopted to reduce event rates so that the events of interests can be selected with high efficiency. The scheme will also reduce the amount of recorded data by discarding most of the unnecessary background events, which would otherwise dominate the triggered events in the early stages of processing.

**Level-1 Trigger.** The first-level trigger is used to store the waveforms and the timing of the signals from each detector to the pipelined FIFO buffers on the FADC/TDC modules. The trigger signal is produced by hardware logic modules. Data from the CsI Calorimeter crystals and other veto systems are used to count roughly the number of photons in the CsI crystals along with additional activities in the veto systems. The goal for the rate after the Level-1 trigger is a few hundreds kHz.

**Level-2 Trigger.** The Level-2 trigger signal is produced by FPGA modules. A clever cluster counting for the CsI crystals will be performed in order to identify not only the two-photon signals that are candidates for the events of interest, but also four-photon or six-photon events for calibration and monitoring. The goal for the rate after the Level-2 trigger is a few tens kHz.

**Level-3 Trigger.** Data in the Level-2 buffer will be sent to an online PC farm. The computers will build the event by using all the data from the subdetectors. A more thorough event reconstruction and filtering will be performed at this stage. The event processing will be done in parallel by distributing the data to the CPUs of the PC farm via fast network switches. All of the events after this filter will be recorded to long-term storage for offline analysis. The goal for the event rate after this filtering is a few kHz.

**Data Acquisition System.** Figure 32 shows the basic schematics of the data acquisition system. The data size is expected to be about 30 kB per event, which requires a data recording speed of 30 MB/sec. The accumulated data size on long-term storage media for one-year (*i.e.*,  $10^7$  seconds) of operation will be about 0.3 PB.

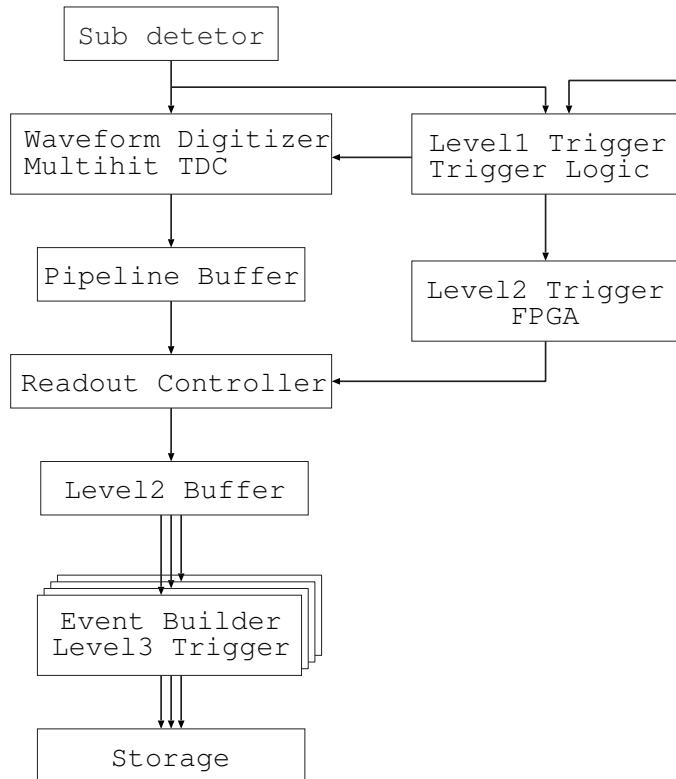


Figure 32: Schematics of data acquisition system

## 4.5 Rates

We estimated the rates at J-Parc by scaling the E391a data.

In E391a, we measured the accidental rates in the detector system with a 1-MeV visible-energy threshold. Table 5 summarizes the singles counting rates per channel for various detector elements in E391a. The rates in the neutral beam was 165 kHz for  $K_L$ 's, and 10 MHz for neutrons ( $E_n > 0.1$  GeV).

The Beam Hole Photon Veto has the highest rate, and the rate in CC07 is also high because of back-splash from the BHPV. This problem will be solved by using the new version of BHPV placed inside a shield.

Table 6 shows the multiplicity of accidental hits in a 100-ns time window for the full E391a detector except for Beam Anti, CC06, and CC07. Summing the rates for different multiplicities, we get the overall veto rate of 450 kHz.

In Step 1, with  $2 \times 10^{14}$  protons on target per pulse, we expect 11.6 MHz of  $K_L$ 's and 486 MHz of neutrons ( $E_n > 0.1$  GeV), *i.e.*, a 49 times higher beam flux. We estimate the accidental rate to be  $450 \text{ kHz} \times 49 = 22 \text{ MHz}$  from the beam, and an additional 4 MHz from  $K_L$  decays in the 21-m region between the front of the detector and the end of BHPV. Thus the overall accidental rate is estimated to be 26 MHz.

Table 5: Summary of counting rates for detector components in E391a with a 1-MeV detection threshold. For the BCV, BHCV, and CV, we applied a 100-keV threshold.

Detector	Counting Rates (kHz)
Main Barrel	7.5
Front Barrel	10
Charged Veto (CV)	3.5
Inner CV	11
Barrel CV	15
Beam hole CV	45
CC02	8
CC03	11
CC04	24
CC05	28
CC06	50
CC07	125
Beam Hole Photon Veto	600

## 4.6 Sensitivity

### 4.6.1 Detector acceptance

In order to identify events for the  $K_L \rightarrow \pi^0 \nu \bar{\nu}$  decay, the following kinematic selection cuts are required. Detailed descriptions of the applications of these

Table 6: Multiplicities of accident hits for all detector components except for Beam Anti, CC06, and CC07, with 100-ns time windows.

Multiplicity	Counting Rates (kHz)
1	312
2	67
3	25
4	14
5	8
> 5	30

cuts for suppressing backgrounds are given in Sec. 4.7.

- $E_\gamma$  cut:  
There are two photons in the Calorimeter with the energy greater than 0.1GeV each. This requirement rejects most of accidental hits. Besides these two photons, there are no clusters with energies above 1MeV.
- Photon veto counters have no energy deposit above 1 MeV. Charged veto counters, BCV, BHCV and CV, have no energy deposit larger than 100 keV.
- Calorimeter fiducial cut:  
The incident position of photons on the Calorimeter should be between 17.5 cm and 85 cm from the center of the beam. This is to ensure that the shower is well contained in the Calorimeter, and the energies and positions of the photons are properly reconstructed.
- Vertex cut:  
The reconstructed vertex position, assuming a  $\pi^0$  mass is between 300 cm and 500 cm in the detector coordinate system.
- $P_T$  cut:  
The reconstructed  $\pi^0$  has transverse momentum between 0.12 GeV/ $c$  and 0.25 GeV/ $c$ . The vertex cut and  $P_T$  cut optimize the background rejection and signal acceptance.
- Collinearity angle cut:  
The collinearity angle is defined as the projected angle of two photons

in the Calorimeter plane ( $x - y$  plane). The collinearity angle is required to be less than  $150^\circ$  to reject  $K_L \rightarrow \gamma\gamma$  background events.

- $E$ - $\theta$  cut:  
The relationship between the incident angle of each photon calculated from the reconstructed vertex and the energy of a photon should satisfy  $\pi^0$  kinematics. This cut is to reduce the odd-pairing  $K_L \rightarrow \pi^0\pi^0$  background, as shown in Fig. 36.
- $E$ -ratio cut:  
The ratio between the lower and the higher energy of the two photons is greater than 0.2. This cut further rejects the odd-pairing background for  $K_L \rightarrow \pi^0\pi^0$  decays, as will be described in Sec. 4.7.1.
- $E$ -total cut:  
The sum of the energies of the two photon is greater than 0.5 GeV. This cut rejects  $\pi^0$ 's produced downstream of the Calorimeter, with photons traveling back upstream.

Figure 33 shows the distribution of  $P_T$  vs. the reconstructed  $z$  position for the  $K_L \rightarrow \pi^0\nu\bar{\nu}$  signal events. For the  $K_L$ 's that exit the beam line at 20 m from the production target, 3.6% of them decay within the fiducial region ( $300 \text{ cm} < z < 500 \text{ cm}$  in our coordinate system). The signal acceptance for the  $K_L \rightarrow \pi^0\nu\bar{\nu}$  decays in the fiducial region, after all the above cuts, is 9.4%.

#### 4.6.2 Acceptance Loss

In addition to the selection cuts explained above, we have to take into account the acceptance loss caused by tight vetoing. We simply estimate the effects by scaling the E391a values, although they surely depend on various experimental conditions.

- Accidental activities: 27%.  
Accidental activities in the detector originate from the high intensity of the beam and back-splash from the Calorimeter.  
With a total accidental rate of 26 MHz, as estimated in Sec. 4.5, and a 10-ns resolving time for vetos, we expect a 26% loss in acceptance.  
As described in Appendix A.4, the acceptance loss due to the BHPV is expected to be 2%.

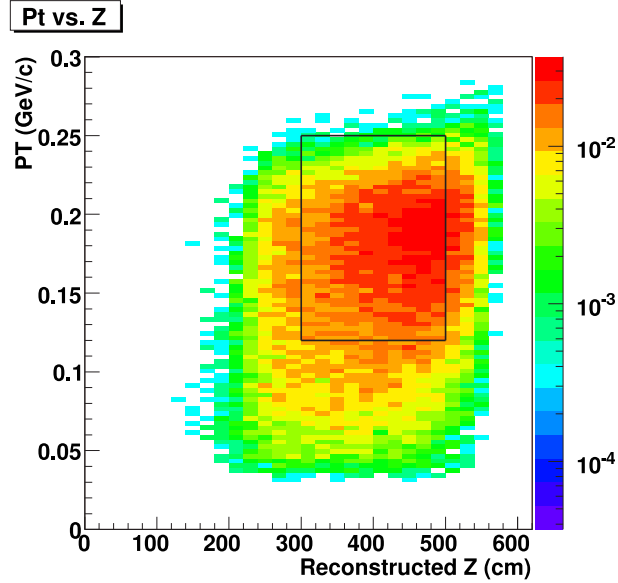


Figure 33: Distribution of  $P_T$  vs. the reconstructed  $z$  position for the  $K_L \rightarrow \pi^0 \nu \bar{\nu}$  signal events. The box shows the signal region.

- Cluster shape cut: 20%.  
In order to identify photon clusters from hadronic showers, and to identify fused clusters, we require the transverse energy distribution within a cluster to be consistent with an electromagnetic shower. A tight shape cut will reject photons and introduce an acceptance loss. The loss should be less for the KTeV CsI crystals, and we assume 20% for it.
- Collateral clusters: 10%.  
Sometimes, a photon cluster in the Calorimeter is associated with an isolated low-energy cluster nearby (“collateral cluster”). As we carefully studied the E391a data [64], we concluded that these collateral clusters are made by low-energy neutrons and photons within the shower. Such a collateral cluster will veto the signal event itself. However, the acceptance loss due to this effect can be reduced by relaxing the veto thresholds in the close vicinity of energetic clusters. We assume that the loss is 10%.

As a result, we expect/assume a 50% acceptance loss in total.

### 4.6.3 Single event sensitivity

In Step 1, assuming  $2 \times 10^{14}$  protons every 3.3 seconds and three Snowmass years ( $3 \times 10^7$  s) of data taking, we expect a total of  $7.3 \times 10^{13}$   $K_L$ 's at the exit of the beam line. With a decay probability of 3.6% in the fiducial region ( $300 \text{ cm} < z < 500 \text{ cm}$ ) and 9.4% acceptance, the single event sensitivity is:

$$\text{S.E.S.} = 1/(N_K \times \text{decay probability} \times \text{acceptance}) = 4.0 \times 10^{-12}$$

With a Standard Model prediction of  $\mathcal{B}(K_L \rightarrow \pi^0 \nu \bar{\nu}) = 2.8 \times 10^{-11}$ , we expect to observe 7.0 events in Step 1. If the acceptance loss is 50% as we estimated, the S.E.S. is  $8.0 \times 10^{-12}$  and 3.5 Standard Model events are expected.

## 4.7 Backgrounds

There are several background sources for the  $K_L \rightarrow \pi^0 \nu \bar{\nu}$  decay, as follows.

- Other kaon decays with particles escaping detection.  
All other  $K_L$  decays except for the  $K_L \rightarrow \gamma\gamma$  decay have four or more photons, or two or more charged particles in the final state. If two or more of these particles are not detected, and the remaining particles are identified as two photons, then the decay will become a source of background. For example,  $K_L \rightarrow \pi^0 \pi^0$ ,  $K_L \rightarrow \pi^+ \pi^- \pi^0$ ,  $K_L \rightarrow \pi^\pm e^\mp \nu$ , *etc.* fall into this category. Therefore, it is crucial to have photon veto and charge veto counters with extremely low inefficiencies. In this proposal, we used the photon veto and charged veto inefficiencies as described in Appendices A.2, A.3, and A.4.
- $K_L \rightarrow \gamma\gamma$ .  
The  $K_L \rightarrow \gamma\gamma$  decay has the same observable final-state particles with the signal decay. However, this decay will be rejected by requiring high transverse momentum ( $P_T$ ) of the  $\pi^0$ .
- $\pi^0$ 's produced by neutron interaction.  
Single  $\pi^0$ 's can be produced by a neutron interaction,  $nA \rightarrow \pi^0 A'$ . Such examples include neutrons in the beam interacting with residual gas in the decay region, and neutrons outside the beam (halo neutrons) interacting with detector materials. Therefore, the decay volume has to be highly evacuated, and detector materials should be placed far from the fiducial region.

- $\Lambda \rightarrow n\pi^0$ .  
 $\Lambda$ 's in the beam can decay into  $n\pi^0$ . This background can be reduced by placing the detector far from the production target to let  $\Lambda$ 's decay away, and by requiring the  $P_T$  of  $\pi^0$  to be larger than the maximum  $P_T$  for the  $\Lambda$  decay.

Table 7 summarizes the estimated background levels. The estimated levels for these backgrounds will be described in the following subsections.

Table 7: The estimated number of background events for Step 1. The single event sensitivity is  $4.0 \times 10^{-12}$ , with which 7.0 standard model events are expected. With a 50% of acceptance loss, both the number of expected signal events and background events would be scaled accordingly.

Background source	#Background events
Other $K_L$ decays	
$K_L \rightarrow \pi^0\pi^0$	3.65
$K_L \rightarrow \pi^+\pi^-\pi^0$	0.93
$K_L \rightarrow \pi^-e^+\nu$	0.01
$K_L \rightarrow \gamma\gamma$	negligible
$K_L \rightarrow \pi^0\pi^0\pi^0$	negligible
Neutron Interaction	
With Residual gas	0.07
At the CC02	0.26
At the C.V.	negligible
Accidental Coincidence	0.20

#### 4.7.1 $K_L \rightarrow \pi^0\pi^0$ background

The  $K_L \rightarrow \pi^0\pi^0$  ( $K_{\pi 2}$ ) decay mode is considered to be the main source of background because of its relatively large branching ratio ( $8.83 \times 10^{-4}$ ) [65] and its 4-photon final state. There are two kinds of  $K_{\pi 2}$  backgrounds: *even pairing* and *odd pairing* according to the missed two photons, which have different characteristics in the event reconstruction.

The even-pairing events are those in which two photons generated from a single  $\pi^0$  decay enter the Calorimeter, and the other two photons from another  $\pi^0$  enter the veto system. The  $\pi^0$ 's are correctly reconstructed and have similar vertex ( $Z_{\text{vert}}$ ) and transverse momenta distributions ( $P_T$ ) to

those of the signal. As shown in Fig. 34, at least one photon has relatively high energy ( $> 50$  MeV) and enters veto counters that provide a high efficiency of vetoing.

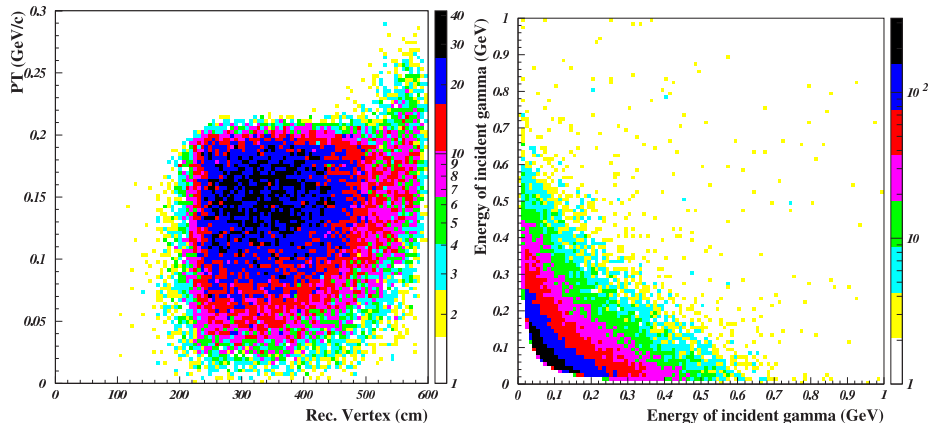


Figure 34: Left: reconstructed vertex and  $P_T$  distribution for even pairing  $K_L \rightarrow \pi^0\pi^0$  background. It has a distribution similar to that of the  $K_L \rightarrow \pi^0\nu\bar{\nu}$  decay. Right: Energy distribution of gammas that enter the veto counters. At least one photon has sufficiently high energy to trigger the counter with a high detection efficiency.

On the other hand, the odd-pairing events have two photons from different  $\pi^0$  decays in the Calorimeter. As a result, the events have smaller probabilities of entering the signal-gating box because the reconstructed vertex is incorrect (moved upstream) and the  $P_T$  distribution tends to be low, as shown in Fig. 35. Even though many events have two low energy photons entering the veto counters, the events are rejected through the high- $P_T$  selection. As a result, the photons that need to be rejected by the veto counters have distributions similar to those for even pairing. However, there is an additional kinematical constraint related to the wrong reconstructed vertex, as shown in Fig. 36. The incident angle of photons deduced from the reconstructed vertex is incorrect and is located in an unphysical region for a given incident energy ( $E$ - $\theta$  cut). Also, the high- $P_T$  selection requires a large imbalance between the energies of the two photons as shown in Fig. 36 ( $E$ -ratio cut). These constraints provide further suppression for odd-pairing events.

The  $K_{\pi 2}$  background level is estimated by using  $7.3 \times 10^7$   $K_L \rightarrow \pi^0\pi^0$ 's decaying between  $z = 0$  m and 6.15 m in the Monte Carlo simulations. For each event, we assigned an event weight as a product of detection inefficien-

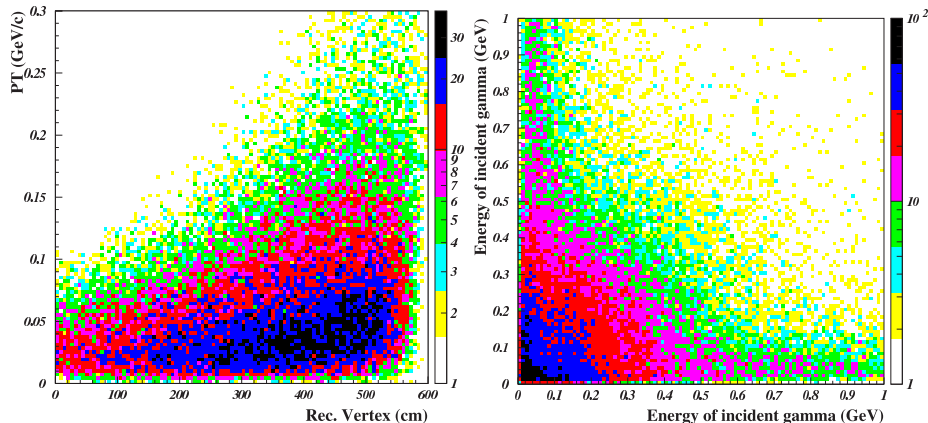


Figure 35: Left: reconstructed vertex and  $P_T$  distribution for odd-pairing  $K_L \rightarrow \pi^0\pi^0$  background. The reconstructed vertex is not correct which make the  $P_T$  lower than the signal box. Right: Energy distribution of photons that enter the veto counters. Even though many events have low energies for both of the photons, the events are rejected through the high- $P_T$  selection. As a result, the photons needed to be rejected by the veto counters have distributions similar to those for even pairing.

cies for all the photons that entered veto counters. The inefficiencies are a function of energy and incident angle of the photon, as described in Appendix A.2. The background level is obtained from the sum of the weights for the events passing all the signal selection cuts.

In the case that three photons enter the Calorimeter, we treated them as one even-pairing and two odd-pairing events according to the assumed missing photon at the Calorimeter. With separate analyses as explained above for each case, the event weights are summed up as a background level.

Another background source is fused events. Among the three photons in the Calorimeter, two photons are mis-identified as one cluster when they enter very close together. These 'fused' clusters can be identified by requiring that the transverse energy distribution within each cluster is consistent with a typical electromagnetic shower. The probability of failing to identify the fusion was studied by the KAMI experimental group, as shown in Fig. 37[66]. We used the fusion probability curve, together with the detection inefficiency of the photon entering the veto counters, to estimate the background.

Table 8 summarizes the sequential acceptance factors for signal events and the  $K_L \rightarrow \pi^0\pi^0$  background, normalized to the number of  $K_L$ 's entering

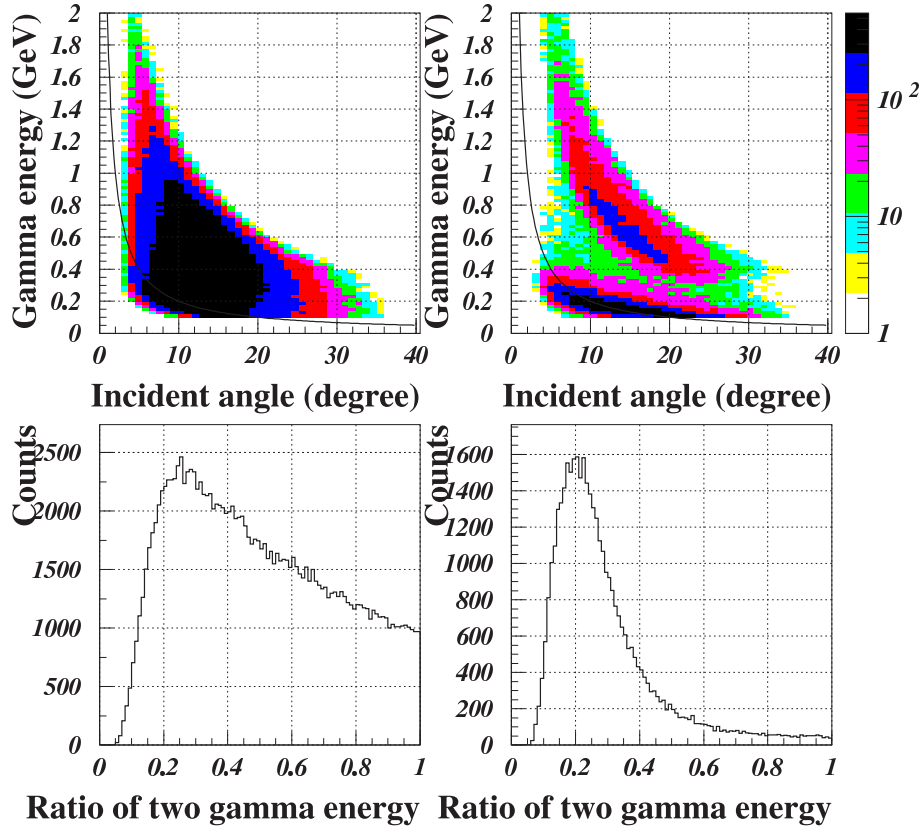


Figure 36: Top-left: Relation between incident energy and reconstructed angle for even-pairing  $K_L \rightarrow \pi^0\pi^0$  background events in the event-gating box. Because the incident angle is correctly reconstructed, the events are located in the allowed region, which is same as that of the signal. Top-right: Relation between incident energy and reconstructed angle for odd-pairing background. The relation is broken due to wrong vertex reconstruction and many events are shifted to an unphysical region. Bottom-left: Energy Ratio between two photons in even pairing, which has the same distribution as signal events. Bottom-right: Ratio between two photons in odd pairing. A large difference between the energies of two photons is needed to satisfy the condition of high  $P_T$ .

the detector setup. Based on  $1.8 \times 10^{21}$  protons on the T1 target in **Step 1** with  $3 \times 10^7$  seconds data taking, 3.65  $K_{\pi 2}$  background events are expected, compared to 7.0 Standard Model signal events. If the 50% acceptance loss on the signal is imposed, the number of background events will be also reduced to 1.8.

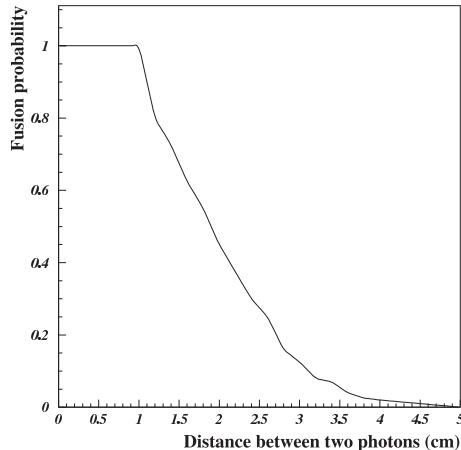


Figure 37: Monte Carlo study of the fusion probability as a function of the distance between two incident photons for the KTeV CsI crystals. [66]

#### 4.7.2 $K_L \rightarrow \gamma\gamma$ background

The  $K_L \rightarrow \gamma\gamma$  decay is easily rejected by kinematic constraints. First, as shown in Fig. 38(right), the reconstructed  $P_T$  of two photons is small. Second, as shown in Fig. 38(left), the collinearity angle between the two photons in the Calorimeter plane (Fig. 39) is peaked at  $180^\circ$ . This would be true even if the energy of a photon is mismeasured due to photonuclear interaction within the Calorimeter. Third, the reconstructed vertex with the assumption of a  $\pi^0$  mass is shifted upstream. As a result, the background from the  $K_L \rightarrow \gamma\gamma$  decay is negligible.

#### 4.7.3 $K_L \rightarrow \pi^0\pi^0\pi^0$ background

Even though the  $K_L \rightarrow \pi^0\pi^0\pi^0$  decay has a large branching fraction of 21%, it is not a serious background source because there are four additional photons. In order to suppress the  $K_L \rightarrow \pi^0\pi^0\pi^0$  decay down to 0.1 events in **Step 1**, we need a rejection factor of  $6.4 \times 10^{-14}$ , which is not difficult

Table 8: Summary of sequential acceptance factors for signal events and the  $K_L \rightarrow \pi^0\pi^0$  background normalized to the incident  $K_L$ 's into the detector setup (including decay probabilities). The decay probability and acceptances are shown for the kaon decays in  $3 \text{ m} < z < 5 \text{ m}$  for  $K_L \rightarrow \pi^0\nu\bar{\nu}$ , and  $0 \text{ m} < z < 6.15 \text{ m}$  for  $K_L \rightarrow \pi^0\pi^0$  decays. For fusion events, the fusion probability is included in the photon veto cut. The number of events is deduced based on  $1.8 \times 10^{21}$  protons on the T1 target.

	$K_L \rightarrow \pi^0\nu\bar{\nu}$	$K_L \rightarrow \pi^0\pi^0$		
		EVEN	ODD	Fusion
Decay Probability	$3.6 \times 10^{-2}$	$11.4 \times 10^{-2}$		
$E_\gamma > 0.1 \text{ GeV}$	$1.53 \times 10^{-2}$	$2.05 \times 10^{-2}$	$3.46 \times 10^{-2}$	$4.65 \times 10^{-5}$
Calorimeter fiducial	$1.05 \times 10^{-2}$	$1.48 \times 10^{-2}$	$2.56 \times 10^{-2}$	$3.01 \times 10^{-5}$
Vertex	$6.98 \times 10^{-3}$	$9.60 \times 10^{-3}$	$1.23 \times 10^{-2}$	$1.48 \times 10^{-5}$
$P_T$	$5.12 \times 10^{-3}$	$7.73 \times 10^{-3}$	$2.41 \times 10^{-3}$	$5.95 \times 10^{-6}$
Collinearity angle	$4.89 \times 10^{-3}$	$7.43 \times 10^{-3}$	$2.25 \times 10^{-3}$	$5.77 \times 10^{-6}$
$E_{\gamma 1} + E_{\gamma 2} > 0.5 \text{ GeV}$	$4.71 \times 10^{-3}$	$7.25 \times 10^{-3}$	$2.16 \times 10^{-3}$	$5.55 \times 10^{-6}$
E- $\theta$ , E-ratio	$3.41 \times 10^{-3}$	$5.28 \times 10^{-3}$	$8.48 \times 10^{-4}$	$4.42 \times 10^{-6}$
Photon Veto	$3.41 \times 10^{-3}$	$5.09 \times 10^{-11}$	$1.95 \times 10^{-12}$	$3.95 \times 10^{-12}$
Branching Ratio	$9.56 \times 10^{-14}$	$4.49 \times 10^{-14}$	$1.72 \times 10^{-15}$	$3.49 \times 10^{-15}$
Number of events	7.0	3.28	0.12	0.25

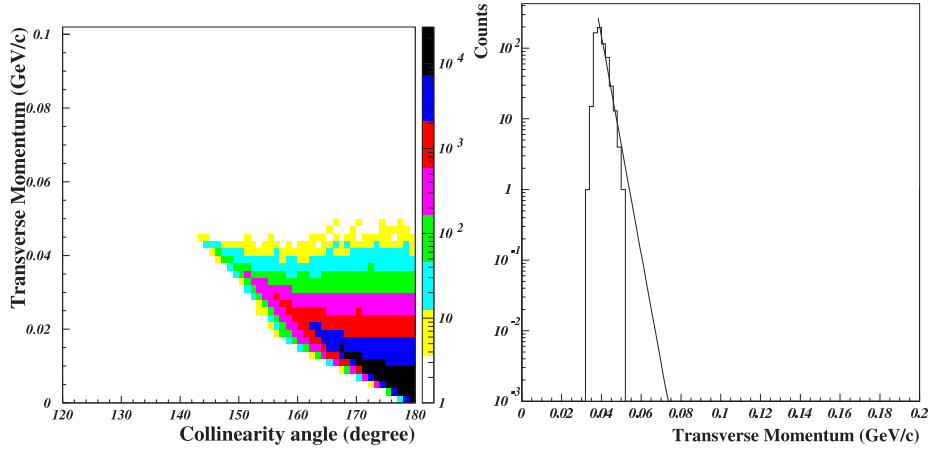


Figure 38: Monte Carlo study for the  $K_L \rightarrow \gamma\gamma$  decays. Left: Distribution of collinearity angle vs.  $P_T$ . Right:  $P_T$  distribution. The total number of generated events is equivalent to  $9.7 \times 10^{10}$  of the  $K_L$ 's entering the detector setup, which is 0.05% of the total number of  $K_L$ 's in Step 1.

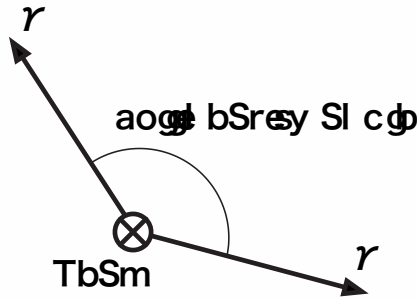


Figure 39: The collinearity angle is the opening angle between the momenta of two photons projected on the Calorimeter plane (x-y plane).

to achieve with the four photons. There is also a further rejection by imposing the high- $P_T$  selection.

#### 4.7.4 $K_L \rightarrow \pi^+\pi^-\pi^0$ Background

One of the major decay modes of the  $K_L$  is  $K_L \rightarrow \pi^+\pi^-\pi^0$ . Because it contains one  $\pi^0$ , it could fake the signal of interest if two charged pions escape detection. There are two methods for reducing this background. One is the kinematic limit of  $K_L \rightarrow \pi^+\pi^-\pi^0$ . The transverse momentum of the  $\pi^0$  ( $P_T$ ) is relatively low, limited to 0.133 GeV/c, and thus the  $P_T$  cut, described in the Sensitivity section, can greatly reduce this background. Second, the charged particle veto counters surrounding the decay region can detect additional charged pions and reject faked events.

Figure 40 shows the distribution of  $P_T$  versus the reconstructed  $Z$  position before and after the charged veto cut. We use here the inefficiency functions for charged particles which are discussed in Appendix A.3 (see Fig. 57), and weigh the remaining events by the inefficiencies of the two pions. As can be seen in Fig. 40, only a small fraction of  $K_L \rightarrow \pi^+\pi^-\pi^0$  comes in the high  $P_T$  region even though the  $P_T$ 's are mis-measured due to the Calorimeter resolution and finite beam size. After applying all the cut and veto weights, the estimated number of background events for the  $3\pi$  mode in the signal box is found to be small, namely 0.93 after requiring  $P_T > 0.12\text{GeV}/c$ .

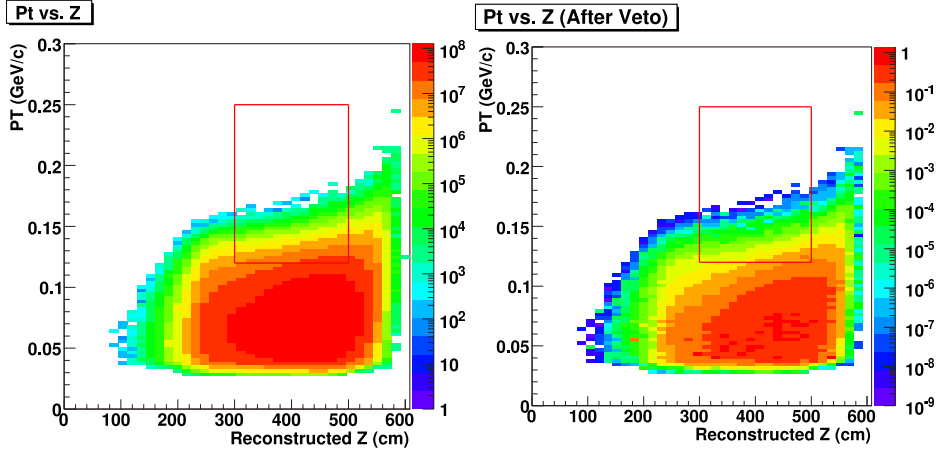


Figure 40: Distributions of  $P_T$  vs. the reconstructed  $Z$  position for the  $K_L \rightarrow \pi^+ \pi^- \pi^0$  background. The left and right plots indicate the distribution before and after charged veto cuts, respectively. The boxes indicate the selection region for the  $K_L \rightarrow \pi^0 \nu \bar{\nu}$  decay mode.

#### 4.7.5 $K_L \rightarrow \pi^- e^+ \nu$ Background

The  $K_L \rightarrow \pi^- e^+ \nu$  background is caused by detection inefficiencies of the  $\pi^-$  and  $e^+$  particles. The momentum distributions of the  $\pi^-$  and  $e^+$  generated from the decay are given in Fig. 41. We generated  $\pi^-$  and  $e^+$  following the distributions for particles that enter a 1-cm-thick plastic scintillator and obtained a detection inefficiency as  $1.4 \times 10^{-4}$  for  $\pi^-$ , and  $7.5 \times 10^{-5}$  for  $e^+$  with a 100-keV detection threshold.

Because the inefficiency is due to charge-exchange interactions, the events not rejected by the Charged Veto involve multi-photon final states which fake 2-photon events. Thus, the most probable background source is that the  $\pi^-$  is missed due to a  $\pi^- p \rightarrow \pi^0 n$  interaction and  $e^+$  is missed due to annihilation into two photons. In order to identify these interactions, we will place the Charged Veto 50 cm away from the Calorimeter. After this distance, the two photons from the  $\pi^0$  and annihilation will open up large enough to be identified as two clusters, as shown in Fig. 42.

Monte Carlo calculations for the Charged Veto inefficient events estimate the acceptance as  $7.6 \times 10^{-6}$  after passing the event selection and photon vetoing. As a result, we expect 0.01 events as a background in Step 1.

The case in which an  $e^+$  enters the beam hole and a  $\pi^-$  enters the Calorimeter would be another source of background because the Beam Hole Charged Veto has a slightly worse detection efficiency. However, the accep-

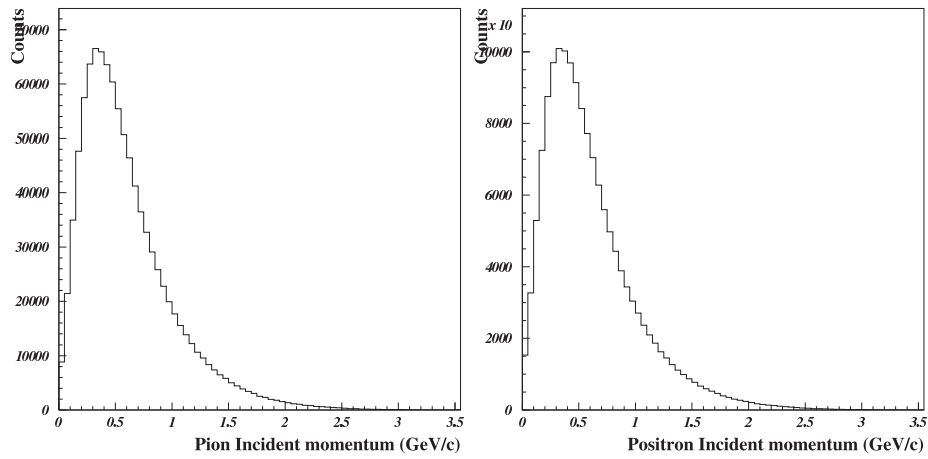


Figure 41: Incident momentum distribution of  $\pi^-$  (Left) and  $e^+$  (Right).

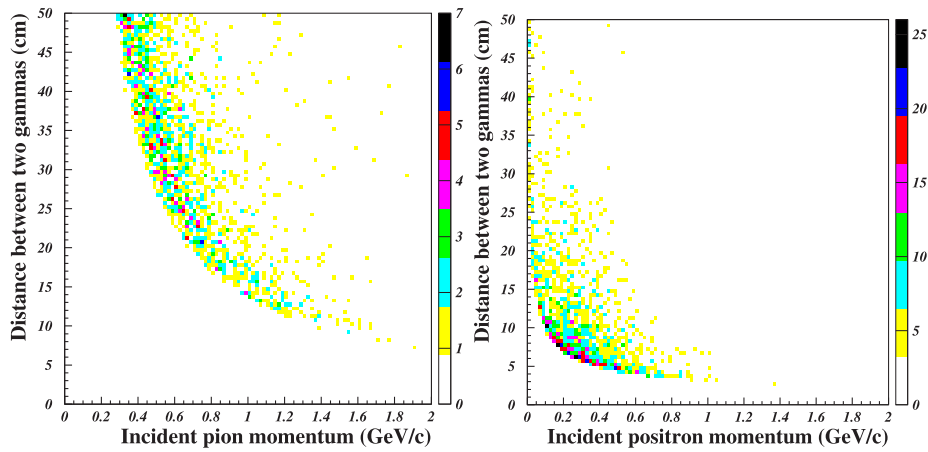


Figure 42: Separation of two photons according to incident momentum by placing the Charged Veto 50 cm away from the Calorimeter as illustrated in the case of  $\pi^-$  (left) and  $e^+$  (right).

tance of the events is estimated as negligibly small.

#### 4.7.6 Neutron Background

The production of  $\pi^0$ 's by neutron interactions through  $nA \rightarrow \pi^0 A'$  is an important source of background. Since the cross section of  $\pi^0$  production is very small for low energy neutrons less than 1 GeV, we take into account the flux of neutrons with energies above 1 GeV. As shown in Table 2, the neutron flux per spill increases by a factor of 4.9 at the **Step 1** compared to E391a, while the  $K_L$  flux increases by a factor 25. This corresponds to a 5-fold reduction of the neutron to K ratio ( $n/K$ ).

In order to reject  $\pi^0$  production by neutrons that interact with residual gas, the decay region is evacuated to  $10^{-5}$  Pa, which was achieved in the E391a experiment. In E391a, we used three different simulation packages to estimate this background level. Even with the largest number of expected background events among the three calculations, we get 0.06 events for the standard model sensitivity ( $3 \times 10^{-11}$  at the E391a study). With the improvement of the  $n/K$  ratio of 0.2, we estimate 0.07 events as a background due to beam neutron interaction in **Step 1**.

Another background source is an interaction of halo neutrons with detector materials, especially at the CC02 (CC02 event) and the Charged Veto (CV event) because these detectors are located close to the fiducial region. In E391a, we observed a clear enhancement of  $\pi^0$  events at the position of these detectors. Because the events are isolated in the reconstructed vertex, we can reject the events with the condition that the fiducial region should be far from these interaction points.

The momentum spectrum of halo neutrons shown in Fig.43 was obtained by calculating the ratio of halo neutrons to beam neutrons in the E391a experiment as a function of the neutron momentum[67], and multiplying the ratio to the beam momentum spectrum for the **Step 1**.

As shown in Fig. 44, the CV events are negligibly small in **Step 1** with the fiducial region 50-cm distant from the position of CV.

On the other hand, the CC02 events have a long tail in the reconstructed vertex distribution, which extends into the fiducial region due to shower leakage explained in Sec. 4.3.1. As shown in Fig. 18, we can get rejection of  $3.7 \times 10^{-5}$  against the events after considering the shower leakage. There is another reduction factor for the CC02 events at the **Step 1**. The calorimeter acceptance for two photons of the CC02 events increases according to the incident momentum of halo neutrons (Fig. 45). Since the neutron spectrum in **Step 1** is softer than E391a, the acceptance at **Step 1** is 13% of the

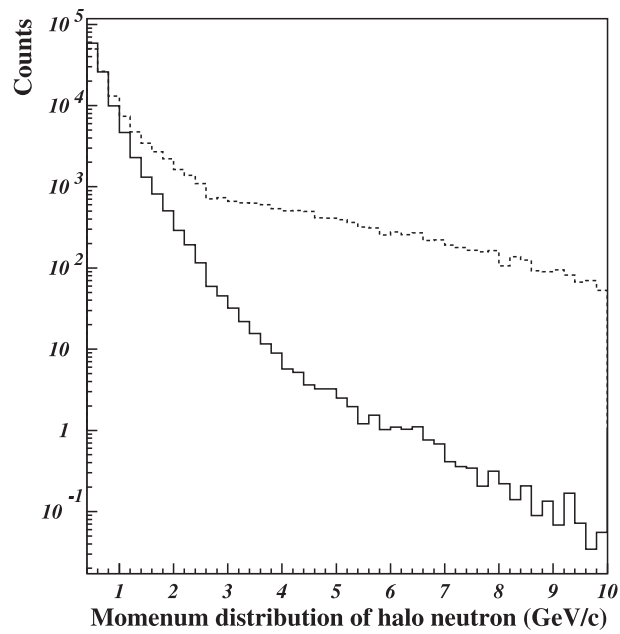


Figure 43: Momentum spectrum of halo neutrons at **Step 1** (solid line) which is scaled by E391a M.C. result (dashed line) according to the ratio of momentum spectra of beam neutrons between **Step 1** and E391 those are give in Fig. 10.

acceptance at E391a.

The number of the CC02 events in E391a is 83 for  $9.6 \times 10^{11}$  neutrons entering detector. With  $1.8 \times 10^{21}$  protons in total for Step 1, we expect  $6.2 \times 10^{14}$  neutrons and  $5.4 \times 10^4$  CC02 events. As a results, we estimate 0.26 events as CC02 background.

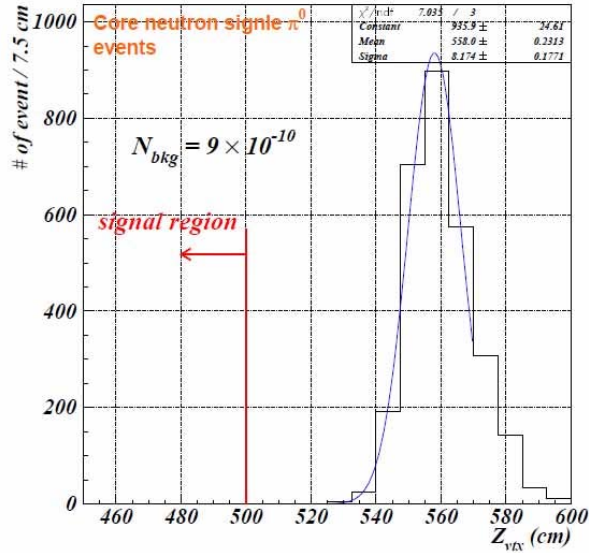


Figure 44: Reconstructed vertex for the  $\pi^0$  events produced at the Charged Veto. In E391a, the background level is estimated to be  $\sim 9 \times 10^{-10}$  for the experiment with a single event sensitivity of  $9 \times 10^{-8}$ . The  $\pi^0$  background from Charged Veto is still negligible in Step 1 with  $10^{-12}$  sensitivity.

#### 4.7.7 Accidental halo neutron background

If two halo neutrons hit the Calorimeter accidentally at the same time and produce showers that mimics electromagnetic showers, they can be a source of background. In the E391a Monte Carlo study, we estimated a 12.5-Hz rate of accidental hits for energy deposits greater than 100 MeV at the CsI together with 1-MeV veto thresholds for other detectors (events mainly from halo neutrons). With a random combination of two generated halo neutron events, we estimated the probability for the event to pass all of the selection cuts, which is found to be  $5.9 \times 10^{-2}$ . The acceptance change according to the neutron momentum is estimated as 0.88.

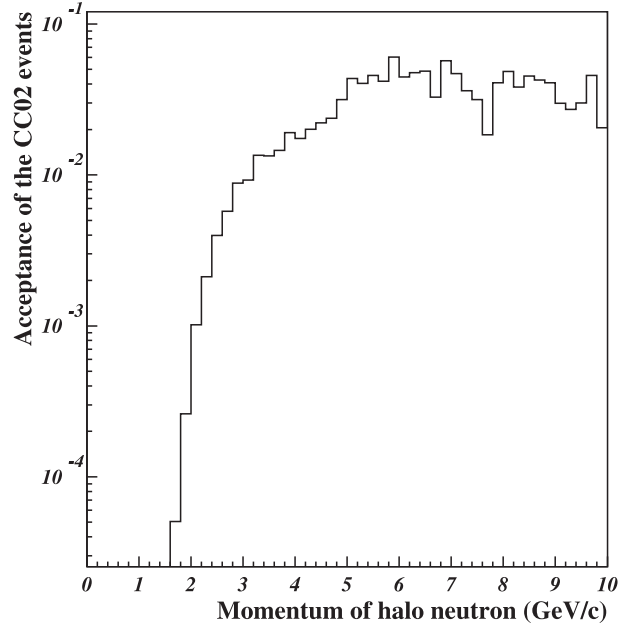


Figure 45: Acceptance of CC02 events as a function of neutron momentum.

For the E391a data, we have developed a neural net analysis to separate the CsI responses to neutrons and true photons based on shower shapes. It removes about 72% of neutron events with a 15% loss of photon events. With the finer segmented CsI crystals in **Step 1**, the performance will be improved.

With 4.9 times larger number of neutrons during the 0.7 s beam spill in **Step 1**, the singles hit rate due to halo neutrons of  $12.5 \times 4.9 \times (1/0.7) = 87.5$  Hz, which is reduced to 24.5 Hz by using the shower shape analysis. The number of background events is given by

$$\begin{aligned}
 N_{\text{B.G.}} &= \text{Rate}^2 \times 2 \cdot \Delta\tau \times T \times \text{Acceptance} \\
 &= 24.5^2 \times 10^{-9} \times ((0.7/3.3) \times 3.0 \times 10^7) \times (5.19 \times 10^{-2}) \\
 &= 0.20
 \end{aligned}$$

where  $\Delta\tau$  is a coincidence resolving time and  $T$  is the effective running time for  $3 \times 10^7$  s of data taking. As a result, we expect 0.23 event in **Step 1** due to accidental coincidences.

## 5 Step 2

In this section we briefly describe the  $K_L^0$  experiment defined as Step 2 in Sec. 3, to be done subsequently to the Step 1 experiment. The goal of Step 2 is to do a precise measurement of the branching ratio for  $K_L^0 \rightarrow \pi^0 \nu \bar{\nu}$  so as to fully determine the direct CP violation in the  $s \rightarrow d$  transition. We assume here that such a measurement has a single event sensitivity of  $3 \times 10^{-13}$ , which is equivalent to about 100 signal events in the Standard Model. We plan to proceed to Step 2 once we understand the beam-related issues at J-PARC and establish the experimental techniques to achieve our physics goal.

### 5.1 New beamline

With the area in the current design of the Hadron Experimental Hall for the neutral beamline and detector, the  $K_L$  yield is not large enough to achieve our physics goal. Thus we will propose, in Step 2, to have a new primary proton beam ( $B$ -line), target, and beam dump in the hall (Fig. 46) and construct a new and optimized  $K_L^0$  beam line. The detector will be located 50 m from the target, and  $K_L^0$ 's will be transported through a narrow "pencil" beam as in the E391a and Step 1 experiments.

The basic parameters of the beamline, whose study is now in progress, are summarized in Table 9. The proton energy is 30 GeV. A distinct advantage of 50-GeV protons over 30 GeV is not yet observed in our studies of detector simulation. We might request, for the accelerator, a longer beam spill and higher duty cycle instead. A new nickel production target (one interaction length) and a lead absorber (7-cm thick) will be used to produce a higher  $K_L^0$  flux with lower photon contamination, respectively. With 30-GeV protons and an extraction angle of  $5^\circ$ , the  $n/K_L^0$  ratio is 30 at the entrance of the detector. The average  $K_L^0$  momenta are higher than those in E391a and Step 1, which is an advantage for removing the  $K_L^0 \rightarrow \pi^0 \pi^0$  background with its extra photons. A 50-m-long beamline is necessary to suppress the background from  $\Lambda$ 's. With several stages of collimators in the long beamline, the flux of beam-halo neutrons to the detector can also be suppressed.

In order to design the new target and beam dump<sup>5</sup> in the hall, we need advice from experts on technical issues, in particular on radiation safety.

---

<sup>5</sup>The beam dump should be located as close as reasonably possible to the target in order to absorb pions before they decay into muons.

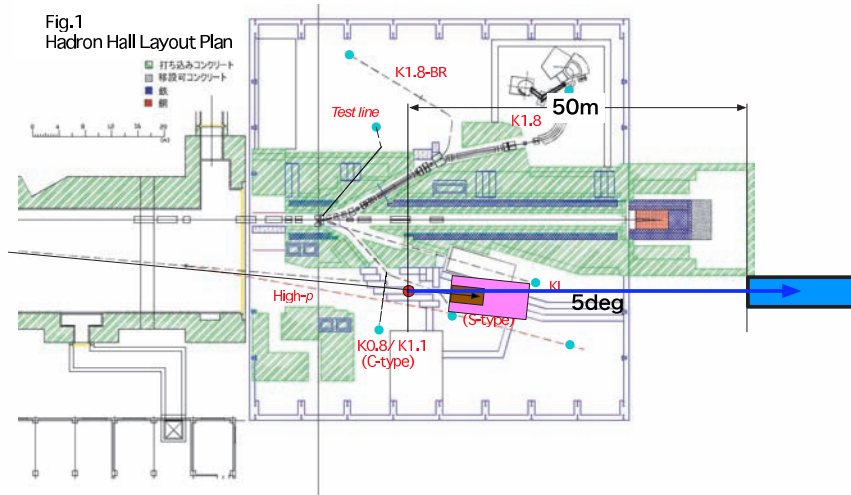


Figure 46: Plan view of the Hadron Hall layout with the  $B$ -line, target (circle in red) and beam dump (rectangles in brown and pink). If the hall is not extended further, the area for the detector (rectangle in blue) will be located outside the hall.

Table 9: Parameters of the new  $K_L^0$  beamline for Step 2.

item	J-PARC Step 2
Primary proton energy	30 GeV
Proton intensity	$3 \times 10^{14}$
Spill length / Beam repetition	0.7 s / 3.3 s
Production Target	new Ni Target ( $1 \lambda_I$ ) Pb absorber (7 cm)
Extraction angle	$5^\circ$
Solid angle	$2 \mu\text{sr}$
$K_L^0$ Yield/spill (beam exit)	$4.4 \times 10^7$
Average momentum of $K_L^0$	5.2 GeV/ $c$
Decay probability in $2 < z(m) < 13$	6 %
Core neutrons/spill	$1.3 \times 10^9$

## 5.2 Detector

The concept of the new  $K_L^0$  detector (Fig. 47) is basically the same as those in E391a and in Step 1. A crystal-based Endcap Calorimeter, with a diameter of 3 meters, detects two photons from the  $\pi^0$  in the  $K_L^0 \rightarrow \pi^0 \nu \bar{\nu}$  decay. Other photon detectors are located at the front, barrel, collar, and beam-hole regions in order to obtain hermetic photon detection<sup>6</sup> and suppress the background from  $K_L^0 \rightarrow \pi^0 \pi^0$ .

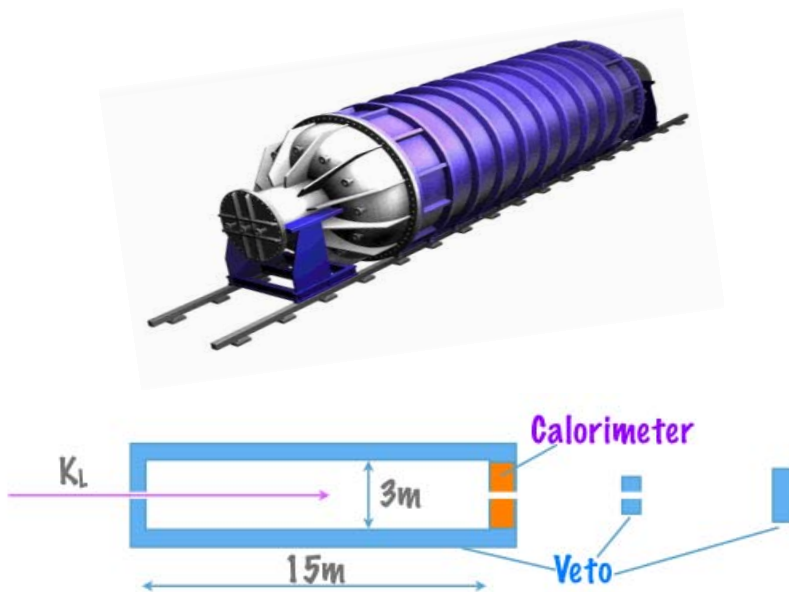


Figure 47: Conceptual view of the new  $K_L^0$  detector for Step 2.

The size of the detector (3 meters radius) and the length of the decay volume (15 meters total) are much larger than those for Step 1, which are based on the existing E391a detector, in order to achieve better sensitivity (the number of  $K_L^0$  decays and  $\pi^0$  acceptance) as well as tighter background rejection. The  $K_L^0$  decays along the beam axis between 2–13 meters from the entrance of the detector, in vacuum, are used for the measurements. This region is 2m away from the upstream Collar Counter and the Charged

<sup>6</sup>A note: We pursued the idea of using the Barrel Calorimeter, covering the long decay volume, for measurements of the  $\pi^0$ 's from  $K_L^0 \rightarrow \pi^0 \nu \bar{\nu}$ . We concluded that, because shower leakage from the Barrel Calorimeter hits the Endcap Calorimeter and vetoes the signal event itself, the sensitivity of the experiment is not improved.

Veto counters at the downstream, to avoid  $\pi^0$  backgrounds produced by halo neutrons in those counters. The large volume of the CsI crystals in the **Step 1** Endcap Calorimeter will be reused, unless we observe some limitations and conclude that we need smaller and/or faster crystals. The Barrel Calorimeter, which is totally 15 m long, should be segmented in the beam direction in order to take care of the back-splash from the showers in the Endcap as well as to have a better rate capability. The Collar and Beam Hole counters, which are located close to or in the beamline, will be designed carefully based on their performance at **Step 1**. The beam hole is set to be as narrow as possible to minimize the number of photons and charged-particles (in particular the  $\pi^+$  and  $\pi^-$  from the  $K_L^0 \rightarrow \pi^0\pi^+\pi^-$  decay) that escape downstream.

### 5.3 Sensitivity and Background

The latest but not yet finalized results of our simulation studies of the beamline and detector for **Step 2** are reported here. We assume the neutral beamline parameters listed in Table 9 and the running condition of  $3 \times 10^{14}$  protons per spill for three Snowmass years ( $3 \times 10^7$  s), which corresponds to  $2.73 \times 10^{21}$  protons on the target and  $4 \times 10^{14}$   $K_L^0$ 's at the entrance to the detector. In order to detect the photons and charged-particles escaping downstream, the Beam Hole Charged Veto and Photon Veto counters, with diameters of 15 cm, are located in the beamline at 10 meters downstream of the Endcap Calorimeter. The same offline selection criteria and photon and charged veto cuts as used in the **Step 1** studies are imposed.

Some results from the simulation studies are shown in Fig. 48. The larger box in the plots indicates the signal region we assume for **Step 2**:

$$200 < Z < 1300 \text{ cm} \quad \text{and} \quad 0.12 < P_T < 0.25 \text{ (GeV}/c\text{)}.$$

We expect to observe  $133.2 \pm 0.4$   $K_L^0 \rightarrow \pi^0\nu\bar{\nu}$  events in the SM with a S/N ratio of 4.8, and with background levels of  $19.4 \pm 0.7$  from  $K_L^0 \rightarrow \pi^0\pi^0$  and  $8.13 \pm 0.11$  from  $K_L^0 \rightarrow \pi^0\pi^+\pi^-$ . The background from hyperon decays ( $\Lambda \rightarrow n\pi^0$ , ..) is negligible. By understanding the characteristics of the distribution of each background source in the  $P_T$  vs.  $Z$  plane and by using likelihood techniques, we would be able to measure the branching ratio with even higher significance.

An optimization for **Step 2**, however, will not be completed until we fully understand the expected single rates and the energy spectrum of accidental hits in the detector, which seriously depend on the quality of the slow-extracted proton beam, the radiation environment of the experimental area,

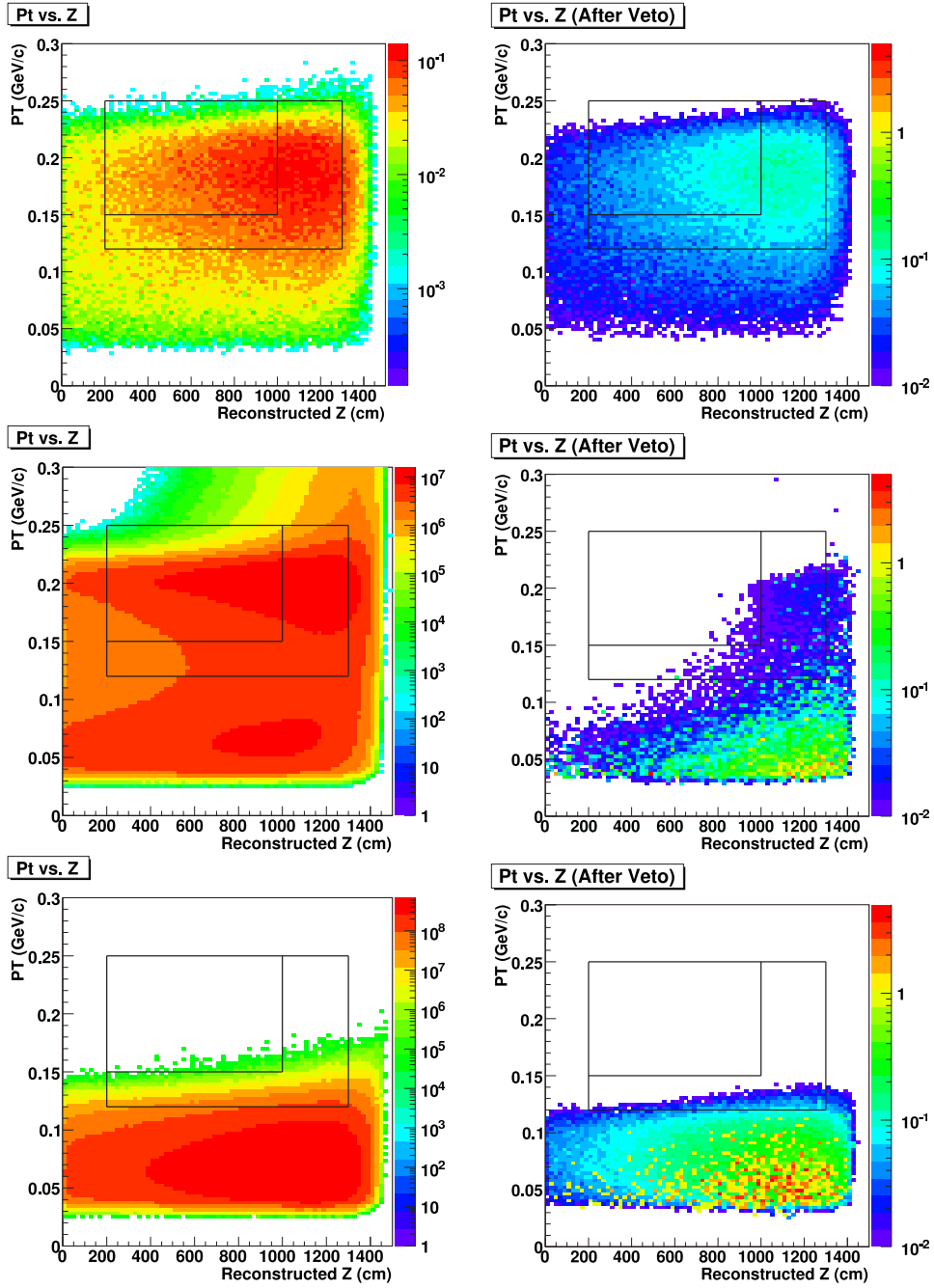


Figure 48: Distributions of  $P_T$  vs. the reconstructed  $Z$  position for  $K_L^0 \rightarrow \pi^0 \nu \bar{\nu}$  signal events (top),  $K_L^0 \rightarrow \pi^0 \pi^0$  (middle) and  $K_L^0 \rightarrow \pi^0 \pi^+ \pi^-$  background events before (left) and after (right) imposing the photon veto cuts, respectively.

and halo neutrons in the collimation of the pencil beamline. What we can learn from the Step 1 experiment in the early stage of J-PARC is therefore very crucial for the success of the Step2 experiment.

## 5.4 Detector R&D

For the Step 2 detector, we are also thinking about introducing new techniques such as photon direction measurements, straw chambers in front of the Endcap, new photo-sensors, *etc.* in order to improve the performance of the detector and the S/N ratio for  $K_L^0 \rightarrow \pi^0 \nu \bar{\nu}$  in the experiment. These techniques will be tested, if possible, as an option or as a potential upgrade within Step 1.

### 5.4.1 Endcap Calorimeter

**PWO crystals.** One of the options for Step 2, if and when the CsI Endcap Calorimeter in Step 1 needs to be changed, is the use of lead-tungstate crystals ( $\text{PbWO}_4$ , PWO). PWO has higher density, a shorter Moliere radius, and faster response than CsI. The electromagnetic shower in PWO is more localized in space and time, thereby reducing the backgrounds due to fusing and blinding effects. Due to the large atomic numbers in PWO, the electromagnetic interaction is much more enhanced in comparison with the photonuclear interaction. Thus a smaller photonuclear inefficiency is expected than for CsI.



Figure 49: PWO crystals for the Beam Hole Photon Veto of E391a before (left) and after (right) being wrapped up.

The manufacturing method of PWO is well established now that a large number of such crystals have been produced for the CMS and ALICE ex-

periments at the LHC. Drawbacks to the material are its small light yield (less than 10% of CsI) and large temperature coefficient ( $-2\%/^{\circ}\text{C}$  at room temperature). It was reported [68] that the light yield is enhanced by a factor of 2.5 if the temperature is decreased from  $20^{\circ}\text{C}$  to  $-25^{\circ}\text{C}$ . However, the short decay time is lengthened (from 10 ns to 20 ns) and the temperature coefficient becomes larger (to  $-4.5\%/^{\circ}\text{C}$ ). In the case of the J-PARC  $K_L^0$  experiment, an operation at  $-25^{\circ}\text{C}$  with high temperature stability is not a fundamental problem, because the crystals are installed in vacuum. We have already studied the performance of PWO when we constructed seventy PWO modules for the Beam Hole Photon Veto in Run 3 of E391a (Fig. 49), and concluded that PWO is a prime option for the Step 2 Calorimeter, should it be upgraded.

**Spaghetti detector.** One of the serious background sources is the  $K_L^0 \rightarrow \pi^0\pi^0$  decay if two photons coming from it are lost due to inefficiencies of the detector system and or cluster fusion in the Endcap Calorimeter. The solution for reducing the cluster-fusion events is to install a photon detector with a good positional isolation capability just in front of the Endcap crystals. A spaghetti calorimeter, consisting of many scintillating fibers embedded in lead, would be a possible candidate.

The R&D for a spaghetti calorimeter has been started for the future Step 2 experiment (Fig. 50). The construction procedure was established by assembling a prototype detector. The performance of the prototype detector with a CCD readout was checked by the beam test held at SPring-8 in March 2006. The main objectives for further R&D were: (1) development of a faster and cheaper readout system by using multi-pixel photon-counters (MPPC), and (2) optimization of the fiber arrangement through Monte-Carlo simulations in order to achieve higher photon-detection efficiency, along with better position and angular resolutions.

#### 5.4.2 Charged Veto

**Straw tubes.** At the University of Chicago, R&D for the possible implementation of vacuum straw tubes (Fig. 51) would proceed forward. The advantages of having tracking capabilities in the experiment are numerous and important. With straw-tube tracking, the  $\pi^+$  and  $\pi^-$  tracks and the vertex from the copious  $K_L^0 \rightarrow \pi^+\pi^-\pi^0$  decay can be reconstructed. Together with the two photons from the  $\pi^0$ , we can (a) calibrate and determinate the absolute energy scale of different detector elements; (b) determine the absolute inefficiencies (with the  $\pi^0$  Dalitz decay); (c) have additional and necessary

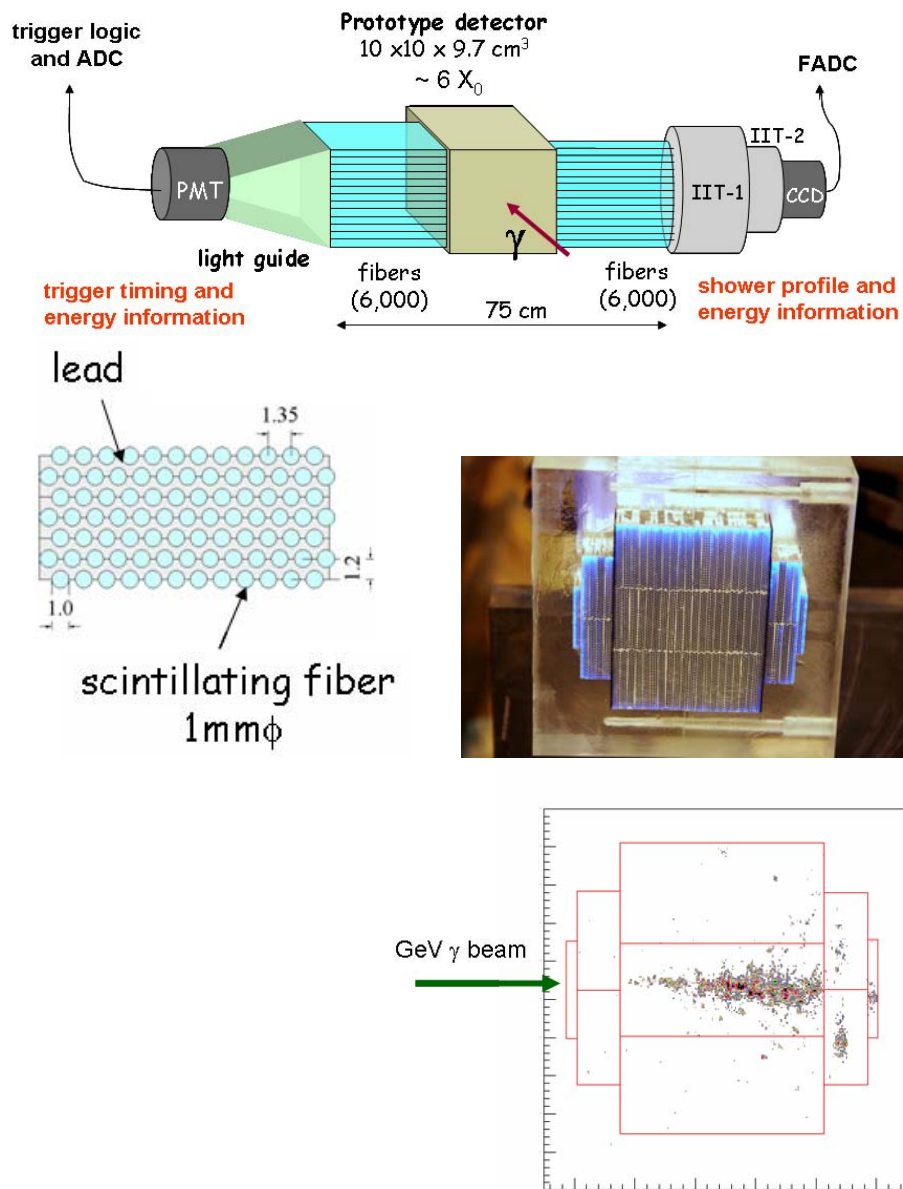


Figure 50: Prototype of the spaghetti calorimeter (top); fiber alignment in lead (middle left); cross section of the prototype (middle right) and shower development of 1-GeV photons recorded in the beam test (bottom).

charged particle vetos to those of the current plastic scintillator panels with redundancy checks on charged-particle veto efficiencies; and lastly, perhaps most importantly, (d) measure the beam shape and halo distributions with the reconstructed transverse positions of the copious  $K_{e3}$ ,  $K_{\mu3}$ , and  $K_{+-0}$  decays.

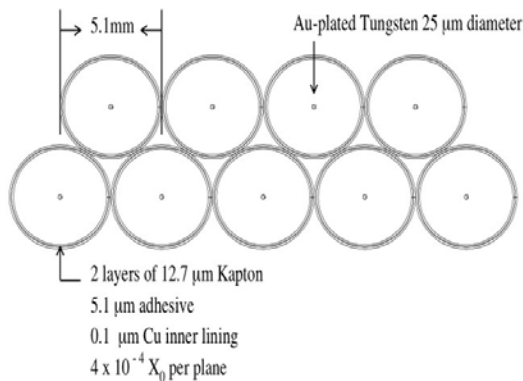


Figure 51: Design of vacuum straw tubes.

Some work has been done already by using the existing Fermilab's straws for the CKM experiment. A beam test was mounted (Fermilab T950) and data were taken in November/December of 2005. The purpose of the beam test is to measure the intrinsic inefficiency (absorption cross sections) of straws.<sup>7</sup> Our physics requirements for straws will be different from those for CKM, and therefore further R&D and likely a second beam test will be needed.<sup>8</sup> A Prototype of full length and with 1/20 full width, double-layer vacuum straws will be tested in a vacuum box. This step is an important one for R&D in that no 2-meter straw tube assembly has ever been tested for performance.

Due to the high density and vacuum requirement of the straws, we wish to start the R&D on the preamps/discriminator circuit and related mechanical infrastructure. This work will be interfaced with the new prototype above, and only 32 channels on one board are needed for evaluation of the

<sup>7</sup>The work was a collaboration of Fermilab, Osaka University, and the University of Chicago. Data analysis is on-going, and we plan to publish the results in the coming months.

<sup>8</sup>We will continue the studies based on the Japan-U.S. Cooperative Research Program in High Energy Physics.

gain/noise performance.

### **5.4.3 Pipeline readout**

VME pipeline TDC modules, which are FPGA programmable with an existing prototype, need extensive software modification to suit our needs. We would like to set up a test bench and build a simple tester system to validate the various properties and proper functions of the module [63].

## 6 Schedule and Cost

### 6.1 Schedule

Table 10 shows our current schedule to prepare and run the experiment.

Table 10: The experiment schedule.

2006	<ul style="list-style-type: none"> <li>• Start preparing the beam collimators.</li> <li>• Prepare for transferring and shipping CsI crystals.</li> <li>• Start designing the new CsI readout electronics.</li> <li>• Start designing the new DAQ.</li> </ul>
2007	<ul style="list-style-type: none"> <li>• Build beam collimators.</li> <li>• Start assembling the additional MB layers.</li> <li>• Ship KTeV CsI crystals.</li> <li>• Move some of the E391a detector parts to J-Parc.</li> <li>• Start assembling the new DAQ.</li> </ul>
2008	<ul style="list-style-type: none"> <li>• Finish installing the beam line by the summer shutdown.</li> <li>• Move most of the E391 detector components from KEK to J-Parc.</li> <li>• Construct the CsI Calorimeter.</li> <li>• Build the DAQ system.</li> <li>• December: Start a beam survey during night.</li> </ul>
2009	<ul style="list-style-type: none"> <li>• Construct and install rest of the detector components.</li> <li>• Continue beam survey, and tune the detector.</li> </ul>
2010	<ul style="list-style-type: none"> <li>• The first physics data taking run.</li> </ul>

### 6.2 Cost

Table 11 shows the estimate on the cost for the **Step 1** experiment. The numbers can still change by a factor of two as detailed designs are developed.

Table 11: Cost estimate for Step 1. Unit: \$1k.

Item	sum	breakdown	cost
Beam line	600	Collimator	200
		Beam shutter	20
		Neutron absorber	20
		Beam pipes and their housing, etc.	260
		Construction	100
Calorimeter	1,110	Disassembling / shipping from FNAL	100
		Storage / fabrication	200
		Front end and ET trigger	600
		Readout	100
		HV	50
		Mechanical infrastructure	50
		Calibration system	10
Main Barrel upgrade	334	Scintillator, lead sheets, WLS fibers	156
		PMT's	55
		Scintillator machining	38
		Mechanical structure, fabrication	85
Vacuum system	250		
BHPV	300	\$11k/module $\times$ 25	275
		PMTs: \$3k $\times$ (25 - existing 18)	25
Collar Counters	200		
Trigger and DAQ	550	HV for non-CsI	200
		Front end for non-CsI	100
		Readout system + CPU	150
		Local Storage	100
Transportation from KEK	500		
Assembling of detector	200		
Total	3,744		

## 7 Conclusion

In order to measure the CP-violation parameters in the  $\Delta S = 1$  transition and to study the flavor physics beyond the Standard Model, we will take a step by step approach to measure the branching ratio of  $K_L \rightarrow \pi^0 \nu \bar{\nu}$ .

As **Step 1**, we will use the common T1 target on the A-line, and use a neutral beam line with a  $16^\circ$  extraction angle. We will use the KEK PS E391a detector with modifications to improve the background rejection. With a total of  $1.8 \times 10^{21}$  protons on target (equivalent to  $2 \times 10^{14}$  protons/spill  $\times 3 \times 10^7$  seconds of running), we expect to observe 3.5 Standard Model events. The S/N ratio is expected to be 1.4.

As **Step 2**, we plan to build a dedicated beam line and upgrade the detector. We expect to observe 133 SM events with a S/N ratio of 4.8 with  $2.73 \times 10^{21}$  protons on target in total.

This experiment will be one of the most precise tools to study CP violation and the physics beyond the Standard Model in the LHC era.

## A Appendices

### A.1 Beam Simulation

A solid understanding of the neutral beam is very important for this type of  $K_L$  rare-decay experiments. To calculate our sensitivity, we need good information for the  $K_L$  yield and spectrum. Higher beam intensities are preferable with regards to sensitivity, but we must then handle a high flux of unwanted particles such as neutrons and beam photons. In order to estimate the beam properties, we have performed Monte Carlo simulations based on the GEANT4 framework. We used the GEANT4/QGSP package for hadronic interactions.

In our calculations, the momentum of primary proton is assumed to be  $30 \text{ GeV}/c$ , and its yield to be  $2 \times 10^{14}$  protons on target (P.O.T.) per beam spill. The spill length and repetition are taken to be 0.7 and 3.3 seconds, respectively.

In Step 1, we use the common target, called the “T1 target”, which is a set of nickel disks, as shown in Fig. 52 [69]. In the simulation, there

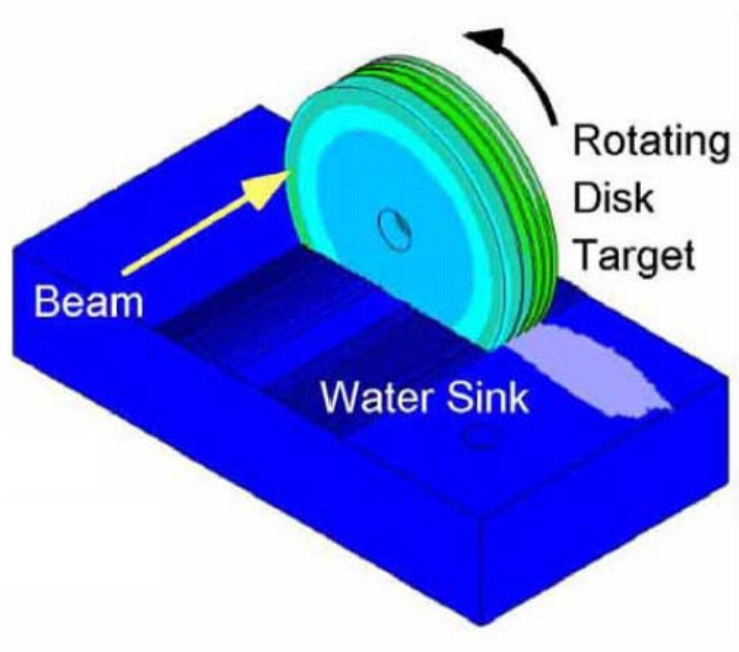


Figure 52: Schematic drawing of the T1 target, prepared by the J-PARC Target Monitor Group.

are five nickel disks of different thickness, 21.7, 11.2, 8.3, 6.8 and 5.9 mm each, and they are placed 3 mm apart. The total thickness is 54 mm, which corresponds to a 36% interaction length ( $\lambda_I$ ). Each disk has a diameter of 280 mm, and the primary protons are injected at 10 mm from the edge. The primary beam size at the target is assumed to be infinitesimal in the calculation.<sup>9</sup>

We adopt the production angle and solid angle of the neutral beam to be  $16^\circ$  and  $9 \mu\text{sr}$ , respectively. To save CPU time, we gathered the secondary products coming between  $15^\circ$  and  $17^\circ$  and calculated the yield by making solid-angle corrections.

As can be seen in the following results, the beam just after the target is dominated by soft photons, which are harmful to the detectors in the beam hole. To reduce such photons, we put the photon absorber made of lead at 2 m downstream from the target.

Figures 53, 54, and 55 show the resultant spectra of our simulations at the detector entrance, *i.e.* 20 m from the target. The Pb absorber can greatly reduce the photon yield, while sacrificing part of the  $K_L$  yield. Table 12 summarizes the calculated yields of  $K_L$ 's, neutrons, and photons, with various thicknesses of the absorber. Considering a realistic handling of the flux, we have decided to use 7-cm-thick lead.

Table 12: Summary of the calculated yields of  $K_L$ 's, neutrons, and photons. All of the numbers are described as the yield per spill, *i.e.* per  $2 \times 10^{14}$  P.O.T.

Absorber thickness	0 cm	5 cm	7 cm	9 cm	Notes
$N(K_L) (\times 10^7)$	1.9	1.0	0.81	0.64	
$N(\text{neutron}) (\times 10^8)$	7.4	4.3	3.4	2.7	$E_n > 0.1 \text{ GeV}$
	1.4	0.84	0.69	0.56	$E_n > 1 \text{ GeV}$
$N(\text{photon}) (\times 10^8)$	230	13	4.5	1.6	$> 2 \text{ MeV}$
	103	2.4	0.61	0.16	$> 10 \text{ MeV}$
	21	0.07	$< 0.01$	$< 0.01$	$> 100 \text{ MeV}$

<sup>9</sup>The size would be 1.3 mm (RMS) according to communications with the Beam Channel Group.

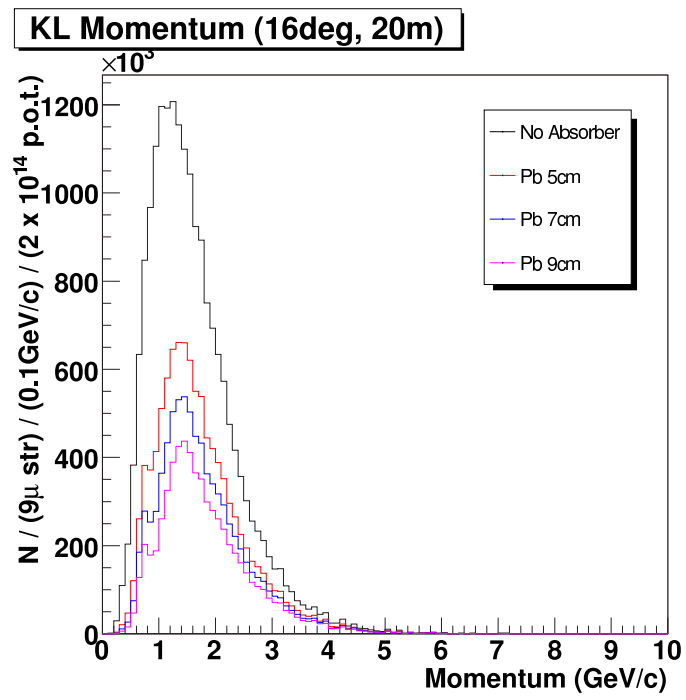


Figure 53:  $K_L$  spectrum with various thicknesses of Pb absorber.

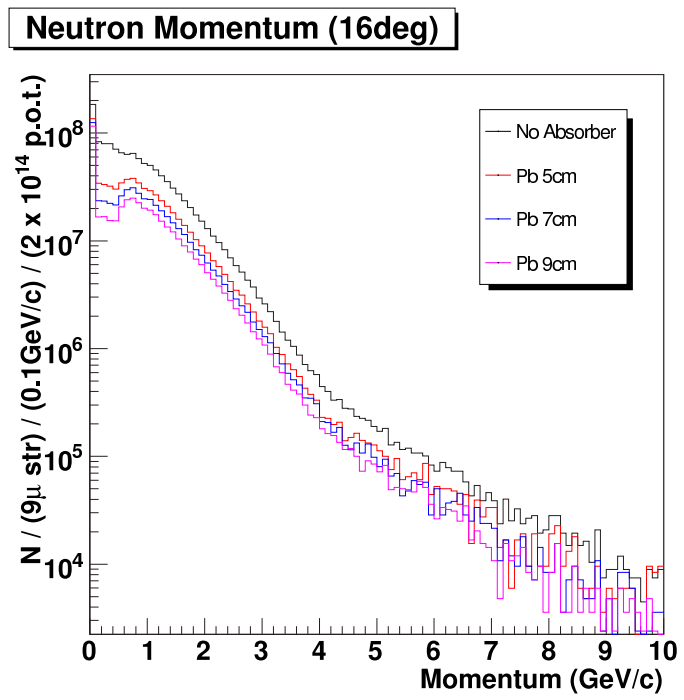


Figure 54: Neutron spectrum with various thicknesses of Pb absorber.

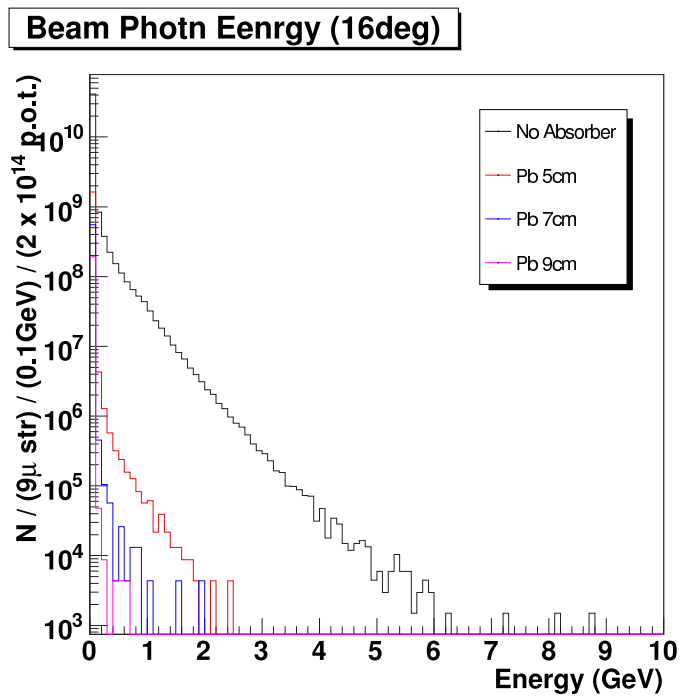


Figure 55: Beam photon spectrum with various thicknesses of Pb absorber.

## A.2 Photon Veto Inefficiency

The detection inefficiency for photons can be caused by the following mechanisms.

**Photonuclear interaction** The inefficiency due to photonuclear interactions is caused by events in which a photonuclear interaction occurs in the Calorimeter prior to an electromagnetic cascade shower, and the secondary particles thus produced do not generate large signals above the detection threshold. For example, neutrons can be produced which then escape the calorimeter.

**Sampling effect** The sampling fluctuation is another source of the inefficiency in sampling calorimeters such as Main Barrel, which consists of alternating lead and plastic scintillation plates. The electromagnetic shower generated in the inactive converter can be totally absorbed and does not produce any signal in the active layers of the detector.

Figure 56 shows the photon detection inefficiencies for CsI and a sampling calorimeter as a function of the incident photon energy. The graphs were used for background estimates. The photon detection inefficiency of the Calorimeter arises when the energy deposition in the Calorimeter is smaller than a given detection threshold. We adopt a 3-MeV detection threshold for the CsI, and 1 MeV for the sampling calorimeter. There are three sources of inefficiency: punch-through, photonuclear interactions, and sampling fluctuations. The punch-through, in which the incident photon penetrates the Calorimeter without any interaction, is well simulated by Monte Carlo calculation and suppressed by having a thick Calorimeter. In Step 1, the full calorimeters are thicker than 16 radiation lengths ( $X_0$ ) and make the punch-through effect sufficiently small.

Even though the total cross sections for photonuclear interactions in calorimeter materials can be evaluated from experimental data [70, 71], it is very difficult to simulate an actual calorimeter response to the produced secondaries with accuracy. Because detection inefficiencies due to photonuclear interactions were measured in a dedicated experiment, they can be used to estimate the backgrounds.

We define the inefficiency functions to represent the inefficiency of the Calorimeter for background estimations. The solid curve in the Left plot in Fig. 56 shows a model inefficiency function that fits the data with a simple power function,  $f = pE^q$ , where  $E$  is the incident photon energy. Because we do not have experimental data for photon energies greater than 2 GeV,

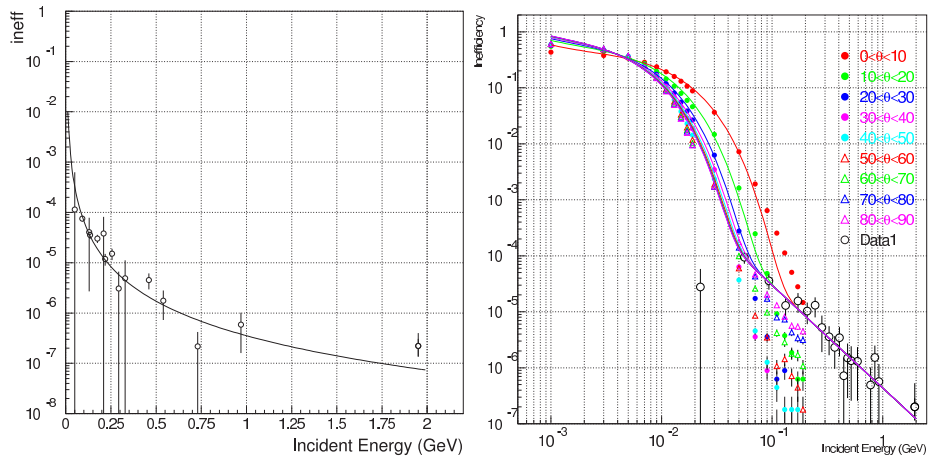


Figure 56: Photon detection inefficiencies for CsI crystals (Left) and a sampling calorimeter (Right) as a function of incident photon energy. The open black circles are experimental data for photonuclear interactions. Monte Carlo results for the inefficiencies due to punch-through and sampling fluctuations are shown in the Right figures as colored points. Different colors indicate different incident angles on the detector. The solid curves are the model inefficiency functions obtained by fitting the data and Monte Carlo results.

we assumed the inefficiency at 2 GeV to be a constant value in the higher energy region. For the very low-energy region where the fit function gives inefficiency values greater than one, we them to the constant value 1, *i.e.* completely inefficient states. Thus we obtain the photon inefficiency function  $f$  for the CsI Calorimeter as

$$f = \begin{cases} 1 & (E < 1.4 \text{ MeV}) \\ 3.54 \times 10^{-7} E^{-2.23} & (1.4 \text{ MeV} < E < 2.0 \text{ GeV}) \\ 7.30 \times 10^{-8} & (2.0 \text{ GeV} < E) \end{cases} \quad (6)$$

For the sampling calorimeter, we evaluated the inefficiency due to punch-through and sampling fluctuations by using Monte Carlo simulations. It is dominant for low-energy photons. We can also expect fluctuations in the photonuclear interaction. They are already included in the obtained data. In the right plot in Fig. 56, the open black circles show the experimental data for photonuclear interactions. A dependence of the photon inefficiency on incident angle arises for the sampling calorimeter because the effective thickness of the inactive converter would be different for the different incident angle photons. Monte Carlo results for the inefficiencies due to punch-through and sampling fluctuations are shown in the right figures as colored points. Different colors indicate the different incident angle to the detector. The solid curves show the model inefficiency functions that fit the data and Monte Carlo results with a sum of power function  $f = pE^q$  and exponential function  $f = ae^{bE}$ , where the power function represents the photonuclear interaction and the exponential function represents the punch-through and sampling fluctuations, respectively. Because we again do not have experimental data for the photon energies greater than 2 GeV, we assumed the inefficiency at 2 GeV to be a constant value for the higher energy region. For the energy region between 5 MeV and 2 GeV, we used the incident-angle-dependent fit functions that categorize the incident angle in nine regions from  $0^\circ$  to  $90^\circ$  in  $10^\circ$  intervals. Below 0.5 MeV, we assumed that the detector is completely inefficient. The energy region between 0.5 MeV and 5 MeV is assumed to be represented by an exponential function connecting the inefficiencies at 5 MeV and 0.5 MeV. Thus we obtain the photon inefficiency function  $f$  for sampling calorimeter as

$$f = \begin{cases} 1 & (E < 0.5 \text{ MeV}) \\ p_1 e^{p_2 E} & (0.5 \text{ MeV} < E < 5 \text{ MeV}) \\ 4.37 E^{-1.83} + p_3 e^{p_4 E} & (5 \text{ MeV} < E < 2.0 \text{ GeV}) \\ 1.23 \times 10^{-7} & (2.0 \text{ GeV} < E) \end{cases} \quad (7)$$

where the parameters  $p_1 \sim p_4$  change for different photon incident angles. These parameters are summarized in the Table 13.

$\theta$ (deg)	$p_1$	$p_2$	$p_3$	$p_4$
5	1.13	-248	0.491	-85.4
15	1.13	-238	0.645	-130
25	1.13	-245	0.729	-162
35	1.13	-249	0.784	-180
45	1.13	-251	0.822	-192
55	1.14	-253	0.845	-199
65	1.14	-255	0.861	-204
75	1.14	-256	0.869	-207
85	1.14	-256	0.873	-208

Table 13: Parameters of the inefficiency functions for the sampling calorimeter defined by Eq. (7). The photon incident angle  $\theta = 90^\circ$  means perpendicular to the detector surface.

### A.3 Charged Particle Veto Inefficiency

Detection inefficiencies for charged particles are due to several reasons. First, it can arise from photoelectron statistics. If the light yield per energy deposit is not sufficient, the probability that pulses will be below the detection threshold is not negligible even if charged particles properly pass through the detector. A second source is the charge-exchange process  $\pi^- p \rightarrow \pi^0 n$  before and/or in the charged particle detector. The  $\pi^-$  can disappear through the process into neutral particles and go undetected. This effect dominates the  $\pi^-$  inefficiency, especially in low-energy region near the large  $\Delta$  resonance. A third source is the  $e^+$  annihilation process in the detector material. Data are available from inefficiency measurements by charged particle beams at KEK [72] and PSI[73]. The former experiment provides data around 1 GeV/ $c$ , and the latter around 300 MeV/ $c$ . We can model the inefficiency function based on these results.

One of the important issues for applying these data to the situation in the J-PARC experiment is the detection threshold. To reduce the inefficiency due to the charge-exchange and annihilation processes, we have to detect a  $\pi^-$  and/or  $e^+$  before it interacts. By setting a lower detection threshold, we can obtain better efficiency. On the other hand, a threshold too low will produce too high a counting rate. We have already had experience with the light yields and counting rates in the E391a experiment, and thus we can

safely estimate reasonable detection thresholds for the J-PARC experiment. In addition, all the sources described above contain charged particles or photons in their final states. The detection efficiency can be improved by using the information of the photon counters behind the charged particle counters. Therefore, the estimates here result from a combination of charged and photon counters.

We performed a Monte Carlo simulation, based on the GEANT4 framework, to obtain inefficiencies for  $\pi^+$  and  $\pi^-$ ,<sup>10</sup> as shown in Fig. 57. Because the result does not reproduce the measured data very well, we decided to use only the shape of the inefficiency curve from the simulation and scale it to fit the data. In these plots, we assumed a detection threshold of 100 keV. Also, we assumed that there exists a 20-mg/cm<sup>2</sup> layer of dead material in front of Charged Veto counters, which accounts for the membrane.

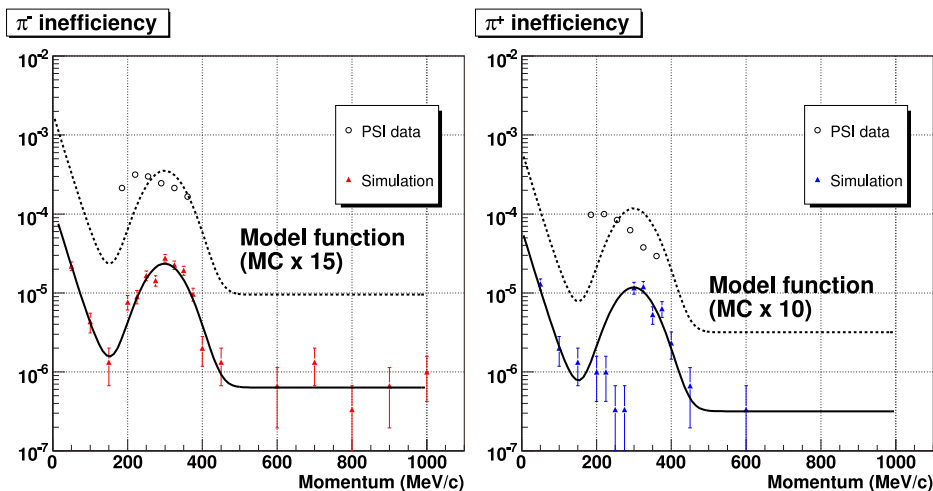


Figure 57: Inefficiencies for negative (left) and positive pions (right), with the combination of charged particle detectors and photon counters behind them. The shape of the curve is obtained by fitting the simulation result, as indicated by the lower curve in the plots. We scaled it to reproduce the measured data by the PSI group, as indicated with dashed line, and used it as the model function of pion inefficiency.

Note that we do not show  $e^+/e^-$  inefficiency functions here because we do not use model functions, unlike the case for charged pions. In our estimates of the  $K_L \rightarrow \pi^\pm e^\mp \nu$  backgrounds, we have fully simulated the

<sup>10</sup>We used the GEANT4/QGSP package for hadronic interactions.

events, including physics processes such as  $e^+$  annihilation, electromagnetic showers, and decay and hadronic interactions of charged particles.

The situation is different for the case of the Beam Hole Charged Veto (BHCV) counter. The BHCV suffers from a high counting rate due to beam photons and neutrons. If a fake signal happens to come just before the particle that we want to veto, wrong timing information is recorded and masks the genuine signal. Even though the BHCV is equipped with waveform digitizers in the readout and has a capability to resolve two adjacent pulses, this effect would be the dominant source of BHCV inefficiency. Extrapolating the counting rate of the Beam Hole Charged Counter in the E391a experiment to the J-PARC environment, we estimate the BHCV inefficiency to be 0.5%, independent of particle species and the energies of the particles.

## A.4 Expected Performance of Beam Hole Photon Veto

In order to estimate the performance of the Beam Hole Photon Veto (BHPV), we have built a simulation tool based on the GEANT3 framework. All of the Čerenkov photons are traced by using our own subroutines. The simulation includes the effects of the measured optical properties of aerogel tiles such as transmittance and Rayleigh scattering length, and the expected reflectivity of the mirror and the Winston cone. The quantum efficiency of the photomultiplier is taken as given in the Hamamatsu catalog, with some correction factors obtained from our beam tests.

Figure 58 shows the expected photon inefficiency as obtained from our Monte Carlo simulations. Here, a hit is defined as a module in which four or more photoelectrons are detected, and we require coincident hits in three consecutive layers. We expect to obtain 99% efficiency for 0.6-GeV photons, and 99.9% for photons of more than 1 GeV, respectively.

Figure 59 shows the hit probabilities for neutrons.<sup>11</sup> As can be seen in the figure, our detection condition gives about 0.2% hit probability for 2-GeV/ $c$  neutrons, which are the main contributors to the false veto probability as described below. By multiplying this neutron sensitivity with the expected neutron spectrum, we can calculate the false hit rate due to neutrons, as shown in the right plot of Fig. 59. Integrating over the neutron momentum, the estimated false hit rate of the BHPV is about 540 kHz.

Figure 60 shows the hit probabilities for  $K_L$ 's that do not decay in the fiducial decay region but rather decay further downstream or interact directly with the BHPV. Similar to the discussion about neutrons, the false hit rates due to neutral kaons were also estimated, as shown in the right plot of Fig. 60. Integrating over the entire momentum region, it is found to be 700 kHz.

In addition to the neutrons and  $K_L$ 's, there exist photons that are produced directly in the production target. These photons also contribute to the false hit rate. From the expected energy spectrum and flux for the beam photons as shown in Appen. A.1, the hit rate due to beam photons is calculated to be 860 kHz, which dominates the false coincidence rate of the BHPV.

A high counting rate in the beam environment causes three problems. One problem is the acceptance loss of  $K_L \rightarrow \pi^0 \nu \bar{\nu}$  events. Because the BHPV is a veto counter, a false hit accidentally kills the real event. This effect can be estimated from the counting rate. From the results above, we estimate the false counting rate due to unwanted beam particles ( $n, K_L, \gamma$ )

<sup>11</sup>We use the GEANT3/GCALOR package for hadronic showers.

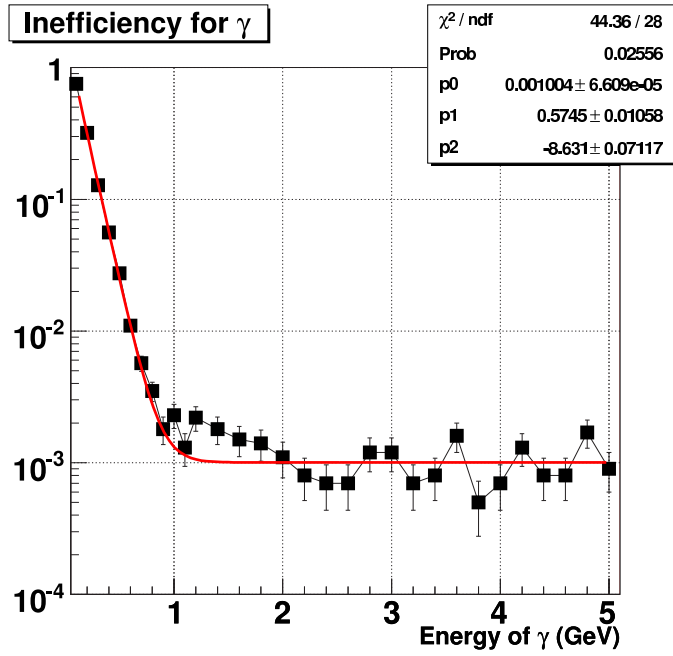


Figure 58: Expected photon inefficiency of the BHPV. We require three or more consecutive hits along the beam direction, where the threshold of each module is set to be 4 photoelectrons. In the calculation, photons are injected randomly in a region of 15-cm diameter and normal to the BHPV face. The red curve indicates our inefficiency function  $\text{Inefficiency} = p0 + \exp(p1 + p2 * E_\gamma)$ , which is used later for background estimations.

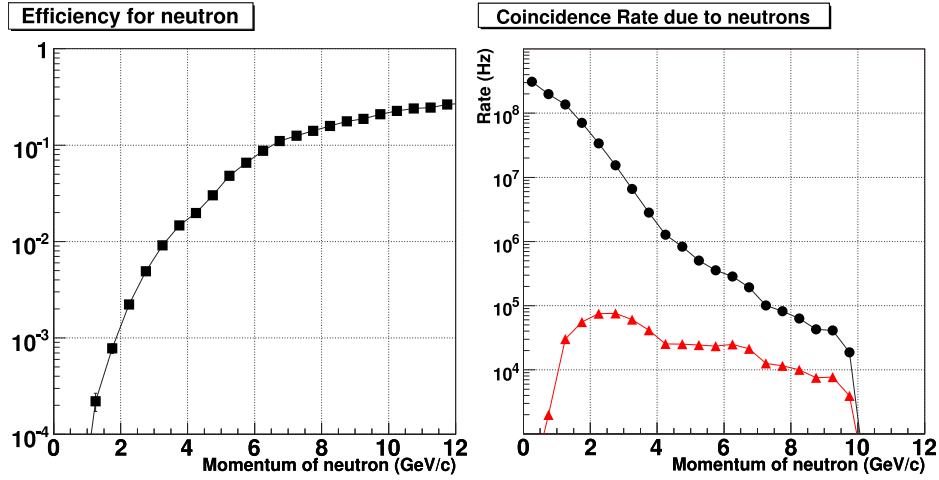


Figure 59: BHPV response to neutrons as a function of momentum. The left plot shows the BHPV hit probabilities for neutrons. The hit condition is the same as the one used in the photon inefficiency calculations, *i.e.* three or more consecutive modules with  $\geq 4$  photoelectrons. Again, the value here is an average over the area of  $\phi$  15 cm. Right plot shows the estimated false hit rate due to neutrons. The upper line with black circles indicates the expected neutron yield. Multiplying by the coincidence hit probability in the left plot, the false hit rate can be calculated, shown as the lower line with red boxes.

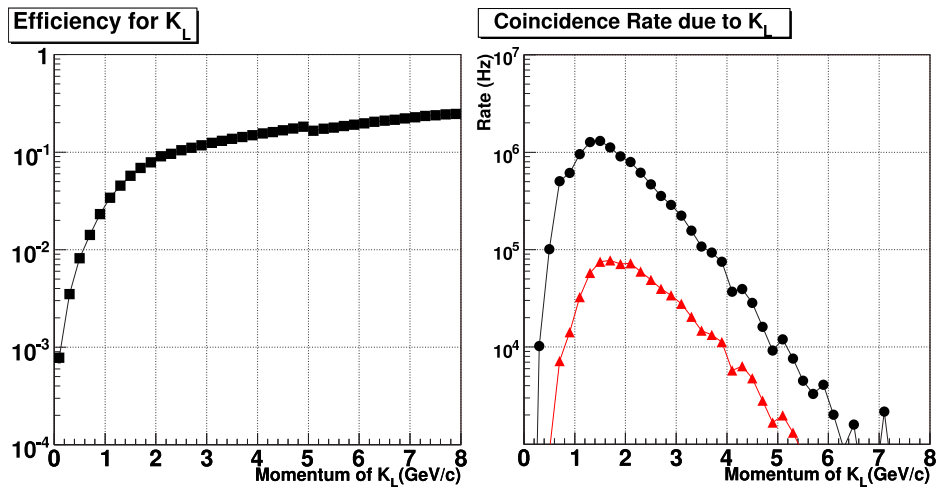


Figure 60: BHPV response to  $K_L$ 's as a function of momentum. Each figure shows the hit probability of the BHPV (left) and the estimated count rate due to  $K_L$ 's.

to be 2.1 MHz in total. Assuming a veto timing window to be 10 ns, the acceptance loss is estimated to be 2%.

Second is the operation of the photomultiplier itself, which is a matter of the singles counting rate of each module. Figure 61 shows the counting rates in the modules as a function of layer number. As can be seen in

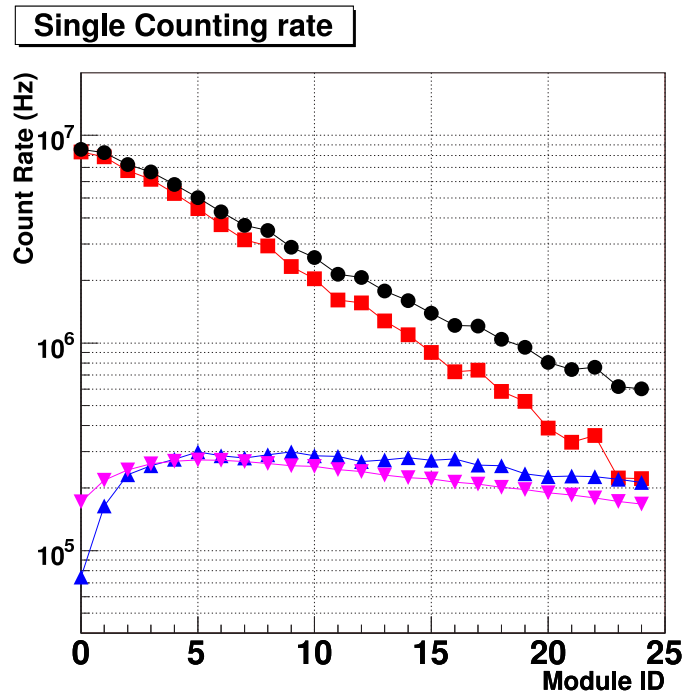


Figure 61: Estimated BHPV counting rates as a function of module ID, where ID 0 (24) means the most upstream (downstream) module. The detection threshold is set to be 4 photoelectrons. The square, triangle, and inverted triangle points show the contributions from beam photons, neutrons, and  $K_L$ 's, respectively, and the circle points indicate their sum.

the figure, the counting rate is dominated by the contribution from beam photons, which reaches a maximum of 8 MHz in the most upstream module. To handle this extremely high rate, each module in the upstream 10 layers is planned to be segmented into quadrants. In addition, there are some options for reducing the singles rates. For example, the photomultiplier tubes can be operated with very low gain and with high speed amplifiers, so as not to suffer a loss in gain. Or the detection threshold can be raised to be 8 p.e. if necessary.

The third problem is the blinding effect. A real photon signal from  $K_L$  decay that we want to catch and veto might be smeared (and thus lost) by adjacent (early or late) particles. In particular, when unwanted signals are larger than the real signal and come just before it, they are likely to cause a loss in efficiency. If we simply assume that a module will be blind for 10 ns once a signal has been generated, based on the double-pulse resolution of the waveform digitizers, we may suffer an efficiency loss of about 1% due to 1-MHz (in average) singles counting rates, as discussed above. The main contributor to the rate is soft photons which do not generate consecutive hits in the BHPV. If the shower size of the photons to be determined, the efficiency loss by accidentals, defined as the probability of destroying coincidences, is expected to be about 0.1%.

We summarize the estimated BHPV performance in Table 14.

Table 14: The summary of the estimated performance.

photon efficiency	$\geq 99\%$ 99.9%	above 0.6 GeV above 1 GeV
neutron hit probability	0.2%	at 2 GeV/ $c$
false hit rate	540 kHz 700 kHz 860 kHz	neutrons $K_L$ 's beam photons
efficiency loss by blindness	0.1%	beam photons

## References

- [1] A. Alavi-Harati *et al.*, *Phys. Rev.* **D 61**, 072006 (2000).
- [2] L.S.Littenberg, *Phys. Rev.* **D39**, 3322 (1989).
- [3] A.J.Buras, F.Schwab, and S.Uhlig, *hep-ph/0405132*, and references therein.
- [4] G.Isidori, *hep-ph/0307014*, *eConf C0304052*, WG304 (2003), and references therein.
- [5] D.Bryman, A.J.Buras, G.Isidori, and L.S.Littenberg, *hep-ph/0505171*, *Int. J. Mod. Phys.* **A21**, 487 (2006), and references therein.
- [6] G.Isidori, *hep-ph/0301159*, *Annales Henri Poincare* **4**, S97 (2003), and references therein.
- [7] G.Buchalla and G.Isidori, *Phys. Lett.* **B440**, 170 (1998).
- [8] W.J.Marciano and Z.Parsa, *Phys. Rev.* **D53**, R1 (1996).
- [9] G.Buchalla and A.J.Buras, *Nucl. Phys.* **B548**, 309 (1999); *ibid.* **B412**, 106 (1994).
- [10] G.Isidori, F.Mescia, and C.Smith, *Nucl. Phys.* **B718**, 319 (2005).
- [11] G.Isidori, G.Martinelli, and P.Turchetti, *Phys. Lett.* **B633**, 75 (2006).
- [12] A.J.Buras, M.Gorbahn, U.Haisch, and U.Nierste, *hep-ph/0603079*; *Phys. Rev. Lett.* **95**, 261805 (2005).
- [13] T.Inami and C.S.Lim, *Progr. Theor. Phys.* **65**, 297 (1981); Erratum-*ibid.* **65** 1172 (1981).
- [14] C.Jarlskog, *Phys. Rev. Lett.* **55**, 1039 (1985).
- [15] K.Sakashita, Ph.D Thesis, Osaka University, 2006; E391a Collaboration, in preparation.
- [16] V.V.Anisimovsky *et al.*, *Phys. Rev. Lett.* **93**, 031801 (2004).
- [17] Y.Grossman and Y.Nir, *Phys. Lett.* **B398**, 163 (1997).
- [18] A.Alavi-Harati *et al.*, *Phys. Rev.* **D67**, 012005 (2003); Erratum-*ibid.* **D70**, 079904 (2004).

- [19] J.R.Batley *et al.*, *Phys. Lett.* **B544**, 97 (2002).
- [20] G.Isidori, F.Mescia, P.Paradisi, C.Smith, and S.Trine, *hep-ph/0604074*.
- [21] A.J.Buras, T.Ewerth, S.Jager, and J.Rosiek, *Nucl. Phys.* **B714**, 103 (2005).
- [22] G.Belanger, C.G.Geng, and P. Turcotte, *Phys. Rev.* **D46**, 2950 (1992).
- [23] C.Bobeth, M.Bona, A.J.Buras, T.Ewerth, M.Pierini, L.Silvestrini, and A.Weiler, *Nucl. Phys.* **B726**, 252 (2005).
- [24] G.D'Ambrosio, G.F.Giudice, G.Isidori, and A.Strumia, *Nucl. Phys.* **B645**, 155 (2002).
- [25] G.Isidori and P.Paradisi, *Phys. Rev.* **D73**, 055017 (2006).
- [26] Y.Nir and M.Worah, *Phys. Lett.* **B423**, 319 (1998).
- [27] See, for example, S.J.Huber, *Nucl. Phys.* **B666**, 269 (2003).
- [28] C.E.Carlson, G.D.Dorata, and M.Sher, *Phys. Rev.* **D54**, 4393 (1996).
- [29] Z.Xiao, C.Li, and K.Chao, *Eur. Phys. J.* **C10**, 51 (1999).
- [30] X-G.He and G.Valencia, *Phys. Rev.* **D70**, 053003 (2004).
- [31] N.G.Deshpande, D.K.Ghosh, and X-G.He, *Phys. Rev.* **D70**, 093003 (2004).
- [32] W-S.Hou, M.Nagashima, and A.Soddu, *Phys. Rev.* **D72**, 115007 (2005).
- [33] A.J.Buras, R.Fleischer, S.Recksiegel, and F.Schwab, *Nucl. Phys.* **B697**, 133 (2005); *Phys. Rev. Lett.* **92**, 101804 (2004). Updates by the authors are in *Eur. Phys. J.* **C45**, 701 (2006).
- [34] T.Goto, Y.Okada, and Y.Shimizu, *Phys. Rev.* **D58**, 094006 (1998).
- [35] T.Goto, T.Nihei, and Y.Okada, *Phys. Rev.* **D54**, 5904 (1996); *ibid.* **D53**, 5233 (1996).
- [36] CKMfitter Group, J.Charles *et al.*, *hep-ph/0406184*, *Eur. Phys. J.* **C41**, 1 (2005), updated results and plots available at <http://ckmfitter.in2p3.fr/> .

- [37] **UTfit** Collaboration, M.Ciuchini *et al.*, *hep-ph/0012308*, *JHEP* **0107**, 013 (2001), updated results and plots available at <http://utfit.roma1.infn.it/> .
- [38] SuperKEKB Task Force, “Letter of Intent for KEK Super B Factory”, **KEK Report 2004-4** (2004).
- [39] U.Haisch, *hep-ph/0512007* .
- [40] C-W.Chiang and F.J.Gilman, *Phys. Rev.* **D62**, 094026 (2000).
- [41] D.S.Gorbunov and V.A.Rubakov, *Phys. Rev.* **D64**, 054008 (2001).
- [42] A.Brignole and A.Rossi, *Nucl. Phys.* **B587**, 3 (2000).
- [43] H.Park *et al.*, *Phys. Rev. Lett.* **94**, 021801 (2005).
- [44] X-G.He, J.Tandean, and G.Valencia, *Phys. Lett.* **B631**, 100 (2005).
- [45] N.G.Deshpande, G.Eilam, and J.Jiang, *Phys. Lett.* **B632**, 212 (2006).
- [46] D.S.Gorbunov and V.A.Rubakov, *Phys. Rev.* **D73**, 035002 (2006).
- [47] C.Q.Geng and Y.K. Hsiao, *Phys. Lett.* **B632**, 215 (2006).
- [48] T.Sasaki, Master thesis (in Japanese), Yamagata University (2006).
- [49] A.Alavi-Harati *et al.*, *Phys. Rev. Lett.* **83**, 917 (1999).
- [50] A.Lai *et al.*, *Phys. Lett.* **B536**, 229 (2005).
- [51] G.D.Barr *et al.*, *Phys. Lett.* **B328**, 528 (1994).
- [52] J-H.Jiang, D-N.Gao, and M-L.Yan, *hep-ph/0304111*, *Mod. Phys. Lett.* **A18**, 977 (2003).
- [53] C.Q.Geng, C.C.Lih, and C.C.Liu, *Phys. Rev.* **D62**, 034019 (2000).
- [54] S.Richardson and C.Picciotto, *Phys. Rev.* **D52**, 6342 (1995).
- [55] P.Heiliger, B.McKellar, and L.M.Sehgal, *Phys. Lett.* **B327**, 145 (1994).
- [56] G.D.Barr *et al.*, *Phys. Lett.* **B358**, 399 (1995).
- [57] H.Watanabe *et. al.*, *Nucl. Instrum. Methods***A545**, 542 (2005).
- [58] Valmiki Prasad, Ph.D Thesis, University of Chicago, June 2002

- [59] M.Doroshenko *et al.*, Nucl. Instrum. Method **A545**, 278 (2005).
- [60] M.Itaya *et al.*, Nucl. Instrum. Methods **A522**, 477 (2005).
- [61] Y.Akune, Master Thesis (in Japanes), Saga University (2003).
- [62] Some informations of CopperII system can be found at <http://www-online.kek.jp/~daqplatform> .
- [63] Some details of this module can be found at <http://hep.uchicago.edu/cpv/ce1337.html> .
- [64] S.Takita, Master Thesis (in Japanes), Yamagata University (2006).
- [65] Particle Data Group, Particle Listings 2005 [http://pdg.lbl.gov/2005/listings/contents\\_listings.html](http://pdg.lbl.gov/2005/listings/contents_listings.html)
- [66] T. Alexopoulos *et al.*, "A Proposal for a Precision Measurement of the Decay  $K_L \rightarrow \pi^0 \nu \bar{\nu}$  and Other Rare Processes at Fermilab Using the Main Injector - KAMI" (2001), available from Fermilab Library by request.
- [67] H.Watanabe, Ph.D thesis, Saga University (2002).
- [68] Talk at KEK seminar by P. Shagin, Jan. 1998, and more improved results of photon yield as a private communication from M. Korzhik (Institute of Nuclear Problems of Berarussian State University) at Minsk, Aug. 2005.
- [69] H. Takahashi, JPS talk, Kouchi, Sept. 2004.
- [70] S. Ajimura *et al.*, Nucl. Inst. Meth. **A 552**, 263 (2005).
- [71] K. Sakashita, "Measurement of the Photon Detection Inefficiency due to Photo-nuclear Interaction", Masters Thesis, Osaka University (2002).
- [72] T. Inagaki, H. Hirayama, T. Sato, T. Shinkawa and Y. Yoshimura, Nucl. Instrum. Methods **A359**, 478 (1995).
- [73] KOPIO Conceptual Design Report, 2005.